UC Merced
UC Merced Electronic Theses and Dissertations

Title

An Optical Investigation of Metal Halide Perovskite Prototypes for Space Photovoltaics

Permalink

https://escholarship.org/uc/item/1wb8j1m5

Author

Erickson, Samuel Scott

Publication Date

2024

Peer reviewed|Thesis/dissertation

eScholarship.org Powered by the California Digital Library
University of California

UNIVERSITY OF CALIFORNIA, MERCED

An Optical Investigation of Metal Halide Perovskite Prototypes for Space Photovoltaics

A dissertation submitted in partial satisfaction
of the requirements for the degree of
Doctor of Philosophy

in

Physics

by

Samuel Scott Erickson

Committee in Charge:

Professor Michael Scheibner, Chair
Professor Sayantani Ghosh, Advisor
Professor Jay Sharping
Dr. Timothy Peshek

2024

Copyright

Samuel Scott Erickson, 2024

All rights reserved

The dissertation of Samuel Scott Erickson, titled An Optical Investigation of Metal Halide Perovskite Prototypes for Space Photovoltaics, is approved, and it is acceptable in quality and form for publication on microfilm and electronically:

Chair _____ Date _____
Professor Michael Scheibner

_____ Date _____
Professor Sayantani Ghosh

_____ Date _____
Professor Jay Sharping

_____ Date _____
Dr. Timothy Peshek

University of California, Merced

2024

Contents

List of Figures vi

List of Tables xii

Abstract xiii

Acknowledgments xiv

Curriculum Vitae xv

1 Introduction 1

2 Perovksite Background 3
- 2.1 Introduction to Perovskites . . . 4
- 2.2 The Emergence of Perovskite Solar Cells . . . 5
- 2.3 Advantages of Metal Halide Perovskites for Photovoltaics . . . 6
- 2.4 Low Earth Orbit Environment and Challenges . . . 8
- 2.5 Metal Halide Perovskites for Space PV . . . 10

3 13^{th} Materials International Space Station Experiment 13
- 3.1 Mission Timeline . . . 13
- 3.2 Sample Fabrication Details . . . 14
- 3.3 Results and Discussion . . . 15
  - 3.3.1 Optical Characterization . . . 15
  - 3.3.2 Photoluminescence Spectroscopy . . . 17
  - 3.3.3 Photostability . . . 20
  - 3.3.4 Temperature Dependent PL . . . 23
- 3.4 Conclusion . . . 25

4 16^{th} Materials International Space Station Experiment 27
- 4.1 Mission Timeline . . . 28
- 4.2 Sample Fabrication Details . . . 29
- 4.3 Results and Discussion . . . 29

4.3.1 Optical Characterization 29
4.3.2 Photoluminescence Spectroscopy 30
4.3.3 UV Photostability 34
4.4 Conclusion 36

5 Proton and Neutron Irradiation of Unencapsulated MHPs 38
5.1 Experimental Design 39
5.2 Results and Discussion 40
5.3 Conclusion 47

6 15^{th} Materials International Space Station Experiment 48
6.1 Mission Timeline 49
6.2 Sample Fabrication Details 50
6.3 Results and Discussion 53
6.3.1 Optical and Fluorescence Microscopy 53
6.3.2 Photoluminescence Spectroscopy 59
6.4 Conclusion 68

7 Conclusion and Future Work 69

A Experimental Background and Methods 72
A.1 Photoluminescence Spectroscopy 72
A.2 Perovskite Electronic Structure 73
A.3 Methods 74

References 77

List of Figures

2.1 **Cost of launch per kg to orbit.** Sustainable engineering designs, such as landing and reusing most rocket components, have considerably reduced the cost per kg to orbit. A few key rocket systems are labeled, with SpaceX vehicles in red. 3

2.2 **Metal halide perovskite crystal structure.** ABX_3 crystal structure where the A site is a cation (Cs, methylammonium (MA) or formamidinium (FA)), B site is a metal (Pb or Sn) and X site is a halide (I, Br, Cl). 4

2.3 **Best research cell efficiencies.** Power conversion efficiency (PCE) plotted over time for non-concentrator perovskite, CdTe, CIGS, and single crystal Si devices. Perovskite and Si are currently tied at 26.1%. Data provided online by NREL [1]. 6

2.4 **AM0 and AM1.5 solar spectra.** AM1.5 solar irradiance standard for Earth-based devices (grey line) and AM0 spectra incident on devices in low Earth orbit (red line). Note the greater UV and visible light intensity of the AM0 spectrum. The integrated UV intensity (below 400 nm) of AM0 is 2.25 times larger than that of the AM1.5 spectrum. 9

2.5 **Tuning MHP bandgap.** For lead-based perovskites, varying cation and halide concentrations can tune the bandgap from 1.55 to 3.1 eV (800 to 400 nm). Reproduced with permission from Wiley and Sons. . 11

3.1 **MISSE-13 sample schematics and edge images.** (A) Schematic of assembled layers for flight sample and control A. (B) Photographs of edges of (top) flight and (bottom) control A samples after the former's return. (C) Schematic of assembled layers for control B without SiO_2. Bold arrows indicate direction of illumination on the ISS. Reproduced with permission from Wiley and Sons [2]. 14

3.2 **MISSE flight facility platform.** The MISSE-13 flight sample was deployed in the zenith orientation, pointing outward normal from the Earth's surface. Reproduced with permission from Wiley and Sons [2]. 15

3.3 **MISSE-13 flight sample photographs.** (A) Immediately after fabrication, (B) 290 hr after fabrication, and (C) post flight. Reproduced with permission from Wiley and Sons [2]. 16
3.4 **Assessing the damaged regions.** (A) Magnified optical image of the damaged region shows a bubble trapped in the encapsulant, indicated by an arrow. (B) Scanning photoluminescence spectroscopy of the same region shows the variation in intensity. White regions indicate no emission signal. Reproduced with permission from Wiley and Sons [2]. 16
3.5 **Confocal Fluorescence Imaging.** Spatial fluorescence images of (A) control A, (B) control B, (C) flight sample, and (D) flight sample after 15 hr AM1.5 light soaking. Red regions are light emitted from samples between 1.55 – 1.65 eV. Dark areas are non-emissive in this energy range. Scale bars 250 µm. Reproduced with permission from Wiley and Sons [2]. 17
3.6 **Investigation of dark regions.** Spatially-resolved maps of PL intensities of the flight sample centered at emission energy in the range (A) 2.5 – 2.7 eV and (B) 1.55 – 1.65 eV. Comparison of the two maps confirm that the non-emissive regions of the MAPI films are PbI_2. Scale bars 200 µm. Reproduced with permission from Wiley and Sons [2]. . 18
3.7 **Quantification of dark confocal regions.** ImageJ analysis of confocal maps for flight and both control samples. Individual dark spots are represented as jittered points with corresponding distribution envelope and boxplot. Total percent dark area for each sample listed above each boxplot. 19
3.8 **Spatial PL distributions.** Histograms of (A) radiative charge recombination lifetime and (B) peak emission energy for each sample over a 500 x 500 µm area. Reproduced with permission from Wiley and Sons [2]. 20
3.9 **Thermal cycling and strain aboard the ISS.** (A) Modeled sample temperature during one ISS orbit. (B) Microscopic strain in the x and y-directions for the MAPI film and both layers in contact with it (glass and SiO_2). (C) Microscopic and (D) macroscopic strain in the z-direction for all modeled layers. Microscopic strains refer to change in length along a given crystalline axis due to thermal effects, while macroscopic strains are overall changes in the dimensions of the entire device layer. Macroscopic strains in the x and y-directions are zero because the MAPI film is fully constrained by the glass and SiO_2. Positive strains indicate tensile strains, while negative strains indicate compressive strains. Reproduced with permission from Wiley and Sons [2]. 21

3.10 **Evaluating device stability under AM1.5 light soaking.** (A) Spectrally integrated PL intensity and (B) spectral FWHM of PL signal recorded every 5 minutes for 15 hours of continuous AM1.5 illumination. The simulated solar spectrum was filtered with a 675 nm short-pass filter before reaching the samples to allow measurement of the PL signal. Inset of (A) are photographs of control B before and after light soaking, depicting widespread photodegradation and color change indicative of PbI_2 formation. Scale bars 1 mm. Reproduced with permission from Wiley and Sons [2]. 22
3.11 **Effects of light soaking on control A.** Distribution of charge recombination lifetime across control A before and after 15 hr AM1.5 light soaking. Photographs pre-LS and post-LS provided to the right. Reproduced with permission from Wiley and Sons [2]. 23
3.12 **Structural phase transition at low temperature.** PL emission intensity mapped as a function of temperature for (A) control A and flight sample (B) before and (C) after light soaking (LS). Phase transition temperature $T_C = 56$ K for flight sample pre-LS. (D) Peak emission energy and (E) FWHM plotted as a function of temperature for all samples. Dashed lines mark T_C for each sample and show a similar behavior for control A and the flight sample post-LS. Reproduced with permission from Wiley and Sons [2]. 24
3.13 **The role of particle radiation.** Results of SRIM (Stopping and Range of Ions in Matter) and TRIM (Transport of Ions in Matter) simulations. (A) SRIM penetration depth of protons in borosilicate glass as a function of energy. Inset shows energy of protons within the 1 mm thick cover glass. (B) TRIM ion simulation for perovskite sample using 14 MeV protons. Reproduced with permission from Wiley and Sons [2]. 26

4.1 **MISSE-16 devices.** (A) Table of all flight and control samples included in the MISSE-16 study. (B) Optical transmission of each top glass material. All samples consist of quartz glass/MAPI/DC93-500/top glass. The only difference between samples is the top glass material, as outlined in A. 28
4.2 **MISSE-16 sample schematic and edge images.** (A) Schematic of assembled layers for all seven devices in this study. (B) Photographs of edges of flight samples utilizing as their top glass material (top) 400 nm long pass and (bottom) 240-395 nm band pass filters. (C) Note the similar glass yellowing as the MISSE-13 flight sample (Fig. 3.1B) for the top sample. No color change can be observed in the UV band pass filters, as they block all visible light. Bold arrows indicate direction of illumination on the ISS. 30

4.3 **Confocal fluorescence microscopy.** Photoluminescence collected between 750 and 800 nm represented as red for (A) glass control (sample 2), (B) glass flight (sample 4), (C) 325-385 nm control (sample 1), (D) 325-385 nm flight (sample 3). 100 µm scale bar for all images. High spatial uniformity of samples made meaningful dark area quantization (as in Fig. 3.7) infeasible. 32
4.4 **Spectral and time-resolved PL metrics.** Boxplots for all control and flight samples provided as a function of (A) energy, (B) FWHM, (C) recombination lifetime, and (D) PL intensity. Each box is composed of 25 data points taken in a 1 mm2 grid across each sample. The small range of (A) and (B) denote little chemical or optical change post-flight. Lifetime (C) and intensity (D) correlation is expected, as shorter lifetimes are likely to be caused by non-radiative recombination and, thus, lower PL counts. 33
4.5 **Device stability under UV light soaking.** Spectrally integrated (A) energy, (B) FWHM, and (C) integrated PL intensity of all seven MISSE-16 samples recorded every 10 seconds for 5 hours of continuous 360 nm illumination. 35

5.1 **Determining proton beam energy.** SRIM/TRIM simulations depicting (A) 20 keV and (C) 1 MeV proton trajectories within irradiated samples. Energy loss of low (B) and high (D) energy protons due to movement through crystal lattice and recoils. 41
5.2 **Scanning electron microscope images.** (A) Control, after proton exposure for (B) 10^{13} p/cm^2, (C) 10^{14} protons/cm^2, (D) 10^{15} protons/cm^2, (E) 10^{16} protons/cm^2. Control sample, 5, 8, 11, and 12, respectively. 41
5.3 **Photodarkening with increasing proton fluence.** Confocal fluorescence images of sample 7 (A) before irradiation, (B) after the first irradiation and (C) after the second irradiation. (D – F) Same protocol for sample 4. Scale bars: 200 µm. (G) Change in percent non-emissive area post- irradiation for all proton fluences tested. 42
5.4 **Confocal PL dark area for neutron-irradiated samples.** ImageJ analysis reveals non-emissive area between 22.7 and 28.8% across neutron samples of two fluences, as well as their control. This is range is negligible and expresses only the variation in perovskite grain density between samples. 43
5.5 **Bandgap and lifetimes with increasing proton fluence.** Box plots depicting (A) band gap, (B) charge recombination lifetime, and (C) spectral full width half maximum averaged over all samples for each radiation fluence. 44

5.6 **AM1.5 light soaking.** (A) Energy, and (B) PL intensity measured over 15 hours of AM1.5 illumination, comparing a control sample with two irradiated with 1015 and 1016 p+/cm2. (C) Percent non-emissive area before and after light-soaking for the same samples. 45
5.7 **Spatial PL change from AM1.5 light soaking.** Confocal fluorescence images before and after 15 hr AM1.5 exposure. Samples exposed to light after receiving proton fluences of zero (A, B), 10^{15} (C, D), and 10^{16} (E, F) protons/cm^2. All sample have the same scale. 46

6.1 **MISSE-15 device schematics.** Two devices of each architecture above were flown aboard MISSE-15. (A) p-i-n MAPI cell, (B) n-i-p triple cation cell, (C) p-i-n formamidinium-rich triple cation cell, (D) n-i-p all-inorganic CsPbI2Br cell. 50
6.2 **Ag and Al contact degradation.** Images of the front of samples 2 (MAPI, A, B), and 3 (triple cation, D, E), pre and post flight. The Ag contacts used in MAPI and FA-rich triple cation samples degraded differently than the Al contacts used in the $CsPbI_2Br$ and triple cation samples. Sub-cells A-F are labeled in (D). This pattern is shared by all samples as viewed from the front (through the top glass). Current-voltage response is plotted for samples 2 (C) and 3 (F). No electrical response was measured for any sample post-flight. 53
6.3 **Optical and confocal analysis of degraded Al region.** (A) Front image of triple cation sample 3. (B) Magnified image of bottom-left Al contact. (C) 4x magnification confocal fluorescence image of this region. Ideally, all PL signal should be blocked by the Al square and appear black in this image. (D) 4x magnification transmission optical microscope image. The characteristic dark red of the MHP layer matches one-to-one with the fluorescent regions in (C). 54
6.4 **Comparing optical microscope images.** (A) 4x magnification optical reflection of degraded Al contact region of triple cation sample 3. (B) Image of both transmitted and reflected light on sample 3. (C) Optical transmission only for the same area. (D) 20x magnification transmission of the corner of the Al contact. 55
6.5 **Combined confocal fluorescence images.** (A) Front image of triple cation sample 3. (B) combined reflection and PL confocal images. White denotes reflection, red emission, and black no signal. Note the large number of bubbles within the encapsulant around the Al square. The MHP layer is still emissive within the bubbles, though the focus must be changed to account for the difference in refractive index. . . 56

6.6 **Cracks in aluminum electrodes of sample 3.** (A) Reflection and emission confocal image of corner of pixel D. (B) Reflection and emission confocal image of center right pixel D. (C) 10x magnification transmission microscope image of Al pixel C. 57
6.7 **Optical and confocal analysis of degraded Ag region.** (A) Front image of FA-rich triple cation sample 5. (B) 4x magnification transmission optical microscope of this region. (C) Combined reflection and PL confocal image of magnified area. Note the more uniform and severe degradation of Ag compared to Al contacts. The faint vertical and horizontal line in C are caused by stitching larger areas together with the confocal microscope. 57
6.8 **Comparison of flight and control Ag degradation.** (A) Front image of FA-rich triple cation sample 5. (B) Combined reflection and PL confocal image of pixel E. (C) Front image of MAPI control sample 9. (D) Combined reflection and PL confocal image of pixel C. Ag degradation is more severe in the flight sample, evidenced by the greater PL signal in the contact area and less reflective Ag with more holes in B. Inset pixels of B and D are 3 x 3 mm. 58
6.9 **MHP between and behind metal contacts.** (A) Back image of MAPI sample 1 taken though substrate. (B) Fluorescence confocal image of region behind Ag contact A (right) and between contacts A and B (left). Note the significant darkening and pitting of the MHP behind the degraded Al contact. 59
6.10 **Spectral and time-resolved PL between metal contacts.** Control samples (in red) and flight samples excited in their centers, between pixels C and D. (A) energy, (B) FWHM and (C) charge recombination lifetime for all non-$CsPbI_2Br$ devices, which returned non-emissive. . 60
6.11 **PL metrics for three regions of MAPI sample 1.** (A) Front and (B) back images of sample 1 showing area of PL maps taken in pixel A, E, and between pixels (denoted X). (C) energy, (D) FWHM, (E) PL intensity, and (F) charge recombination lifetime for all three areas measured through each side of the sample. Region X was not measured though the substrate. 62
6.12 **PL and TRPL maps of intact Ag region.** (A) Front image of FA-rich triple cation control sample 14. (B) Back image of sample 14 with area of map taken through substrate in red (sample has been flipped top-to-bottom from front image). Heatmaps of (C) energy, (D) FWHM, (E) PL intensity, and (F) charge recombination lifetime. Top right region (within dashed black line) maps MHP behind intact Ag contact while remaining area is between contacts. 64

6.13 **PL and TRPL maps of degraded Ag region.** (A) Front image of FA-rich triple cation sample 5. (B) Back image of sample 5 with area of map taken through substrate in red. Heatmaps of (C) energy, (D) FWHM, (E) PL intensity, and (F) charge recombination lifetime. Top right region (within dashed black line) maps partially-degraded MHP, bottom right is MHP behind intact Ag contact, and left side is MHP between pixels A and B. 66
6.14 **PL redistribution in MAPI sample 1.** Spectral camera capturing PL through the substrate of sample 1 (A) pre flight and (B) post flight. Degradation of MHP layer behind Ag contacts post flight results in fewer charges extracted overall and greater emission in MHP between pixels. 67

A.1 **Halide perovskite band contributions.** Typcial orbital structure of the (A) Sn and Pb metals, as well as the (B) Cl, Br, and I halides found in MHPs. (C) Formation of perovskite bandgap from the overlapping metal and halide atomic orbitals. (D) Calculated bandgap for perovskite crystals with varying chemistries. (E) Cartoon of energetic postions of trap states in the MHP bandgap compared to other semiconductors [3]. 73
A.2 **PL/TRPL collection schematic.** A home-built laser system was used to collect all PL data presented in this thesis. From the SuperK laser, the beam is reflected from two adjustable mirrors to ensure proper alignment. The first 50/50 beamsplitter allows the laser to reach the sample while also redirecting the PL. After the laser is removed with a 715 long pass filter, the second beam splitter divides the PL equally between the single photon avalanche diode and spectrometer. 75
A.3 **Lightsoaking configuration.** Photograph of Newport LSH-7320 Solar Simulator and sample aligned beneath. The MHP device has been placed between the necessary filters at the proper distance from the simulator to best imitate the AM1.5 spectrum. A fiber optic cable below the sample captures PL and sends it to the Actron 2300 Spectrometer. 76

List of Tables

4.1 ***Photographs of all MISSE-16 samples.*** *Images of all samples described in Fig. 4.1A, taken after flight samples returned from the ISS. UV band pass filters appear black, obscuring the MHP layer in four samples. Of the three visible perovskite films, two (samples 2 and 5) show a small number of bubbles trapped within the DC93-500 encapsulant. All substrates are 1 in^2.* 31

5.1 ***Irradiated samples included in study.*** *Unencapsulated $CH_3NH_3PbI_{3-x}Cl_x$ on ITO glass. A non-irradiated control sample was also fabricated alongside each batch (samples 1-8 and 9-12). . Samples 1-4 exposed to fast (4.5 MeV) and thermal (<0.05 eV) neutrons. "Low n^0" total dose of 2.76x10^4 mrem, while "high n^0" experienced 5.52x10^4 mrem. These doses are equivalent to 1 and 2 years on the lunar surface, respectively. Beam flux for each proton fluence described in methods.* 40

6.1 ***Details for all MISSE-15 flight and control samples.*** *Samples 1-8 flew aboard the ISS, while 9-15 remained on Earth as control samples. Each of the four device types will also be referenced to encompass all devices of a given perovskite composition.* 49

6.2 ***MISSE-15 flight samples.*** *Photographs of all flight samples presented from the front, back, and front with back illumination. Regions which appear grey or silver in the front images are intact Al or Ag. Yellow regions in all images are due to degradation. All substrates are 1 mm^2.* 51

6.3 ***MISSE-15 ground control samples.*** *Photographs of all control samples presented from the front and back. Note the discoloration of many Al and Ag contacts, though not as severe as in the MISSE-15 flight samples. All substrates are 1 mm^2.* 52

Abstract

Metal halide perovskites (MHPs) have garnered significant interest as semiconductors for optoelectronic devices like solar cells in the past 15 years due to their defect-tolerant crystal structure, tunable bandgap, and impressive photovoltaic performance. This dissertation will examine the viability of MHP-based photovoltaics for operation in the harsh low Earth orbit (LEO) environment around the International Space Station (ISS) through a combination of ground-based experiments and analysis of samples exposed to actual LEO conditions. To evaluate the resiliency of MHPs in space, prototype thin films of the perovskite methylammonium lead iodide (MAPI) were flown on multiple Materials International Space Station Experiment (MISSE) missions mounted outside the ISS. Among these was the first perovskite device to orbit the Earth, doing so nearly 4800 times and demonstrating MHPs could survive for 10 months in LEO. Optical analysis like photoluminescence spectroscopy will be discussed heavily throughout this work, as most samples were electrically isolated and fully encased in glass. To further explore the effects of high-energy particle radiation in LEO, unencapsulated MAPI films were subjected to controlled proton and neutron irradiation on Earth. While neutron exposure caused no changes, proton fluences above 10^{13} cm^{-2} led to photodarkening, spectral blueshift, and reduced charge carrier lifetimes. Such proton fluences are orders of magnitude greater than those experienced over a decade in LEO, demonstrating MHP resilience to particle damage. Finally, this thesis will examine the effects of the LEO environment on complete MHP solar cell devices of different architectures. Through advanced spectroscopy and microscopy, the fundamental photophysics of MHPs subjected to these extreme stressors will be revealed. Overall, the cells returned with localized MHP damage due to top contact (Ag or Al) migration, though the perovskite remained intact outside of these regions.

Acknowledgments

I feel impossibly lucky to have had such supportive family, friends, teachers, and mentors throughout my life. You certainly deserve more praise than this. I thank my mother, Lisa, father, Randy, and stepfather, Patrick, for your constant love and help along the way. Among dozens of my amazing teachers, I must thank Richard Campbell for igniting my love of physics in the eighth grade.

On the research side of things, I must of course thank Dr. Sayantani Ghosh for her direction, time, and willingness to put up with me for five years. I thank Dr. Michael Scheibner, Dr. Jay Sharping, and Dr. Timothy Peshek for serving on my doctoral committee, asking difficult questions, and guiding my research.

Thanks to everyone in the Perovskites in Space team for the amazing research opportunity and years of collaboration. Thank you Dr. Lyndsey McMillon-Brown and Dr. Timothy Peshek at NASA Glenn for leading the team, as well as Dr. Joseph Luther and Dr. Kaitlyn VanSant at NREL for your invaluable input. A special thanks to my friend Dr. William Delmas for teaching me how an opto-electronics lab works.

Finally, to my amazing, beautiful, and only slightly shorter than average wife, Madison, thank you for many months of encouragement across many drafts of this thesis. I love you and can't wait for our new life back East.

Curriculum Vitae

Education

University of California, Merced (2019-Present)
Doctor of Philosophy: Physics

University of Arkansas, Fayetteville, Arkansas (2015-2019)
Bachelor of Science: Physics
Minors: Mathematics, History, Anthropology

Work Experience & Research Appointments

University of California, Merced (2019-Present)
Graduate Student Researcher
Researcher in an optoelectronics characterization lab, under the supervision of Prof. Sayantani Ghosh. Primary research interests include perovskite semiconductors, photovoltaics for space applications, and high-resolution spectroscopy. *Highlights include:*

- Spectroscopy and microscopy of metal halide perovskite (MHP) prototypes for experiments on Earth an the International Space Station (ISS)
- Development of novel electrohydrodynamic deposition process for MHP fabrication in space
- Optical characterization of unencapsulated perovskite thin films before and after proton and neutron irradiation

First Solar, Perrysburg, OH (Fall 2023)
Tandem Development Intern
Worked within the Advanced Research Group to develop new characterization protocols for experimental MHP devices. Assisted team members in data collection,

processing, and visualization using JMP. Wrote custom I-V programs in Python to control hardware and study device hysteresis.

University of Arkansas (2017-2019)
Undergraduate Research Fellow
Studied defect formation in epitaxially-grown barium and strontium titanate perovskites. Utilized transmission and scanning electron microscopes to identify crystal defects. Regularly operated atomic force microscope to study friction, polarization, and topography of samples.

Publications

[1] S. Erickson, C. Lum, K. Stephens, M. Parashar, D. K. Saini, B. Rout, C. Park, T. J. Peshek, L. McMillon-Brown, and S Ghosh. Elucidating Early Proton Irradiation Effects in Metal Halide Perovskites via Photoluminescence Spectroscopy. Submitted to *Joule*, (2024).

[2] W. Delmas*, S. Erickson*, J. Arteaga, M. Woodall, M. Scheibner, T.S. Krause, K. Crowley, K.T. VanSant, J.M. Luther, J.N. Williams, J. McNatt, T.J. Peshek, L. McMillon-Brown, and S. Ghosh. Evaluation of hybrid perovskite prototypes after 10-month space flight on the International Space Station. *Advanced Energy Materials*, 13(19):2203920, (2023). (*contributed equally to this work).

[3] H. Zhang, E.T. Vickers, S. Erickson, M. Guarino-Hotz, J. L. Barnett, S. Ghosh, and J. Z. Zhang. Synthesis and Properties of Stable Amino Metal Halide Molecular Clusters in the Solid State. *Journal of Physical Chemistry Letters* 13, 10543–10549, (2022).

[4] T. Al. Morgan, M. Zamani-Alavijeh, S. Erickson, G. Story, W. Schroeder, A. Kuchuk, M. Benamara, and G. J. Salamo. Self-assembled stoichiometric barium titanate thin films grown by molecular beam epitaxy. *Journal of Crystal Growth* 493, 15–19, (2018).

Conference Presentations

[1] S. Erickson, W. Delmas, C. Lum, J. Arteaga, K. T. VanSant, J. M. Luther, T. J. Peshek, L. McMillon-Brown, and S. Ghosh. Perovskites in Space: Promising Results Aboard Two ISS Missions. Materials Research Society Spring Meeting (2024).

[2] S. Erickson, W. Delmas, J. Arteaga, M. Woodall, M. Scheibner, T. S. Krause, K. Crowley, K. T. VanSant, J. M. Luther, J. N. Williams, J. McNatt, T. J. Peshek, L. McMillon-Brown, and S. Ghosh. Evaluation of hybrid perovskite prototype after 10-month space flight on the International Space Station. New Generation Photovoltaics for Space (2023).

[3] S. Erickson, W. Delmas, J. Arteaga, M. Woodall, M. Scheibner, T. S. Krause, K. Crowley, K. T. VanSant, J. M. Luther, J. N. Williams, J. McNatt, T. J. Peshek, L. McMillon-Brown, and S. Ghosh. Effects of 10-Month Low Earth Orbit Exposure on Hybrid Perovskite Thin Film. American Physical Society March Meeting (2023).

[4] S. Erickson, W. Delmas, J. Arteaga, M. Woodall, M. Scheibner, T. S. Krause, K. Crowley, K. T. VanSant, J. M. Luther, J. N. Williams, J. McNatt, T. J. Peshek, L. McMillon-Brown, and S. Ghosh. Evaluation of hybrid perovskite prototype after 10-month space flight on the International Space Station. Materials Research Society Spring Meeting (2023).

[5] S. Erickson, S. Ghosh, L. McMillon-Brown, and T. J. Peshek. Using Electrohydrodynamic Deposition for In-Space Manufacture of Perovskite Solar Cells. American Physical Society March Meeting (2021).

[6] S. Erickson, S. Ghosh, L. McMillon-Brown, and T. J. Peshek. Using Electrohydrodynamic Deposition for In-Space Manufacture of Perovskite Solar Cells. Materials Research Society Spring Meeting (2021).

Chapter 1

Introduction

Metal halide perovskites (MHPs) are a class of materials with the crystal structure of naturally occurring mineral perovskite ($CaTiO_3$). Over the past 15 years, they have emerged as promising semiconductors for various optoelectronic applications, particularly photovoltaics (PV) or solar cells. This dissertation compiles the author's work at the University of California, Merced, focusing on photovoltaic MHP viability in low Earth orbit (LEO). This is accomplished through ground-based experiments including proton irradiation of samples, as well as pre and post flight characterization of devices placed outside the International Space Station (ISS).

Chapter 2 provides background on halide perovskites and the unique challenges of space photovoltaics. It begins with the parameters which define the perovskite crystal before a brief history of key MHP advancements. Discussion of advantageous properties among MHP devices is followed by an overview of how such devices are useful in space. Finally, the environment and stressors of LEO are addressed, defining the operational space for ISS missions and ground tests in future chapters.

Chapter 3 focuses on a prototype MHP sample which was exposed to the LEO environment for ten months aboard the 13^{th} Materials International Space Station Experiment (MISSE) mission. To understand how the MHP film was affected by this environment, the sample was designed without charge transport layers or electrical contacts. Upon returning to the Earth, the prototype was characterized optically along with its two ground control samples. Since the samples were fully encased in glass, the project was limited to optical techniques including high resolution photoluminescence (PL) spectroscopy and confocal fluorescent microscopy. Through careful investigation, the flight sample was believed to have been thermally strained by its nearly 4800 orbits around the Earth. This strain was relaxed after 15 hours illumination from a solar simulator post flight, resulting in recovery of PL metrics. Ultimately, the flight sample endured ten months in LEO with no non-reversible degradation. As the first perovskite material to orbit the Earth, the MISSE-13 flight sample demonstrated the resiliency of MHPs and paved the way for future perovskite devices in

space.

Chapter 4 investigates the changes among samples aboard another ISS mission, MISSE-16. Since the sun-facing substrate of the MISSE-13 flight sample blocked the ultraviolet (UV) light of the extraterrestrial solar spectrum (AM0), a new batch of MHP prototypes was designed specifically to test the effects of UV light. These five flight and two control samples consisted of methylammonium lead iodide ($CH_3NH_3PbI_3$, or MAPI) thin films spin coated on glass, then encapsulated with different top glass materials. Like the MISSE-13 samples, these devices were designed to isolate the MHP layer to determine how it would be affected by LEO stressors. Top glass materials included three UV band pass filters, one 400 nm long pass filter, and one high transmission Eagle XG glass. Post flight, no samples exhibited signs of UV damage. Instead, all samples returned with fewer signs of degradation than the MISSE-13 flight sample.

Chapter 5 details a terrestrial MHP proton and neutron irradiation study. The 1-2 mm thick top glasses of MISSE-13 and 16 samples blocked most high energy particles found in LEO. Fully realized MHP devices in space will require far thinner cover glasses to remain light and cost effective. To better explore the effects of particle radiation on MHPs, unencapsulated perovskite films were exposed to two neutron fluences and six proton fluences. While neutrons had no measurable impact, clear signs of damage were observed among MHP samples above proton fluences of $1x10^{13}$ cm^{-2}. Films exposed to 10^{14} – 10^{16} p^+/cm^2 exhibited PL photodarkening, energetic blue shift, and considerable reduction in radiative charge recombination lifetime.

Chapter 6 summarizes results from the MISSE-15 mission. While prior chapters examine the resiliency of isolated MHPs to LEO stressors, this chapter turns to full perovskite solar cells. Two samples each of four different architectures were exposed to LEO for eight months. Post flight, microscopic and spectroscopic methods were used to compare flight and control devices. Although the Al and Ag contacts of all flight samples returned partially degraded, the perovskite between these pixel regions remained emissive and similar to their control devices.

As the cost to bring a payload to orbit continues to fall, governments, scientific bodies, and private companies will continue to commercialize space. MHPs are excellent candidates to provide cheap, defect tolerant, and lightweight power to future satellites and space stations. The primary motivation for this work is to understand how perovskites endure the many stressors of LEO. Since most samples are fully encapsulated in glass, non-destructive optical characterization techniques such as confocal microscopy and photoluminescence spectroscopy will be used to determine the quality of each MHP film. These methods will reveal the novel physics of MHP devices and help determine their viability for space applications.

Chapter 2

Perovksite Background

The exploration of space has been a profound human endeavor, fueled by scientific curiosity and technological advancements. With continued exploration and commercialization of our solar system, the demand for reliable and efficient power sources becomes increasingly vital. Metal halide perovskites (MHPs), a remarkable class of materials that have emerged as a promising solution for space photovoltaics, offer a unique combination of exceptional optoelectronic properties, low-cost manufacturing, and resilience to the harsh conditions of the space environment [4–7]. The commercialization of low Earth orbit (LEO) has experienced a massive cost reduction in the past decade, thanks to the pioneering efforts of companies like SpaceX (Fig. 2.1). This has paved the way for a surge in the deployment of spacecraft, satel-

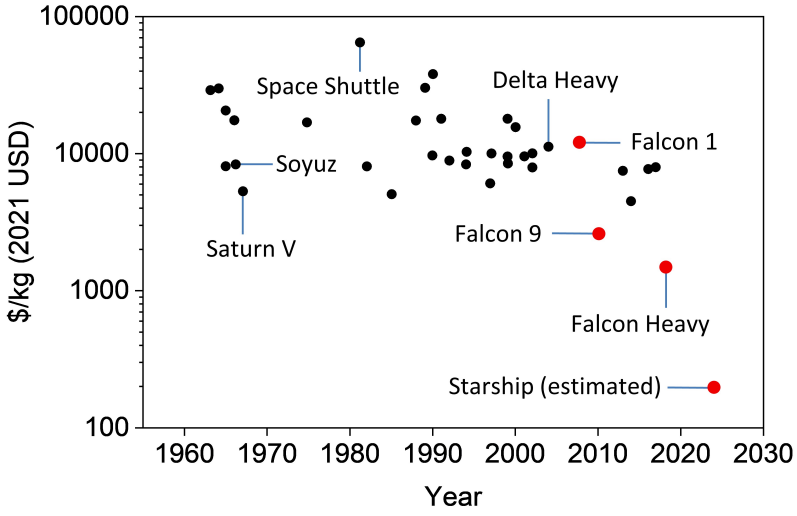


Figure 2.1: Cost of launch per kg to orbit. *Sustainable engineering designs, such as landing and reusing most rocket components, have considerably reduced the cost per kg to orbit. A few key rocket systems are labeled, with SpaceX vehicles in red.*

lites, and other space-based systems. Consequently, the need for cheap, reliable, and abundant power sources has grown dramatically. MHPs stand out as an attractive candidate, possessing the potential to withstand the stressors of LEO while being lightweight, cost-effective, and highly efficient [8, 9]. This introduction will delve into the fascinating world of perovskites, exploring their unique material properties, rise in photovoltaic applications, and suitability for space-based solar energy generation. It will provide a comprehensive overview of the challenges associated with space environments and how perovskites are exceptionally well-suited to overcome these obstacles.

2.1 Introduction to Perovskites

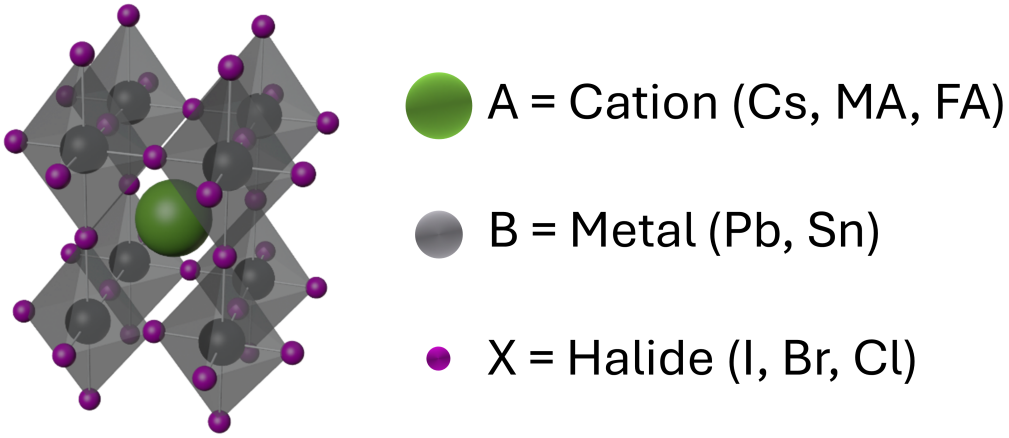


Figure 2.2: Metal halide perovskite crystal structure. *ABX_3 crystal structure where the A site is a cation (Cs, methylammonium (MA) or formamidinium (FA)), B site is a metal (Pb or Sn) and X site is a halide (I, Br, Cl).*

Perovskites are a class of crystalline materials defined by their distinctive crystal structure, represented by the chemical formula ABX_3. In this structure, A is a monovalent cation (such as methylammonium $CH_3NH_3^+$, formamidinium $HC(NH_2)_2^+$, or cesium Cs^+), B is a divalent metal cation (commonly lead Pb^{2+}, more exotically tin Sn^{2+} or germanium Ge^{2+}), and X is a monovalent anion, typically a halide (iodide I^-, bromide Br^-, or chloride Cl^-). The arrangement of these ions results in a cubic or pseudocubic structure with a diverse range of possible chemical compositions (Fig. 2.2). The stability and distortion of the perovskite structure are governed by the Goldschmidt tolerance factor, which considers the ionic radii of the constituent elements. The tolerance factor is given by the equation: $t = (r_A + r_X) / \sqrt{2(r_B + r_X)}$, where r_A, r_B, and r_X are the ionic radii of the A, B, and X ions, respectively. For an

ideal cubic perovskite structure, the tolerance factor should be close to 1, with values between 0.8 and 1.0 typically considered stable. Additionally, charge balance and the oxidation states of the elements play a crucial role in determining the overall stability and properties of the perovskite material. The charge neutrality condition requires that the sum of the positive charges from the A and B cations must equal the sum of the negative charges from the X anions. By carefully selecting the elements and their ratios at the A, B, and X sites, researchers can fine-tune the material's properties, such as bandgap, carrier mobility, and stability, to meet specific requirements for various applications, including photovoltaics, light-emitting diodes, and photodetectors [10, 11].

2.2 The Emergence of Perovskite Solar Cells

The discovery of perovskites dates to 1839 when the mineral perovskite ($CaTiO_3$) was first identified by the German mineralogist Gustav Rose and named after the Russian mineralogist Lev Perovski [12]. However, it wasn't until the late 20th century that perovskite structures were explored for their intriguing electrical and optical properties, paving the way for their eventual application in solar cells and other optoelectronic devices. The breakthrough in perovskite solar cell (PSC) research occurred in 2009 when Tsutomu Miyasaka and colleagues at Toin University of Yokohama, Japan, demonstrated the use of organo-metal halide perovskites as light absorbers in dye-sensitized solar cells, achieving an efficiency of 3.8% [13]. This pioneering work sparked intense research efforts worldwide, as the exceptional properties of perovskites for photovoltaic applications became increasingly apparent. In 2012, a major milestone was achieved when researchers from the University of Oxford led by Henry Snaith demonstrated the first solid-state perovskite solar cell with an efficiency exceeding 10% [14]. Since then, the field of perovskite photovoltaics has experienced remarkable progress, with power conversion efficiencies (PCEs) continuously increasing, surpassing 26% in laboratory settings (Fig. 2.3) [1, 15–18]. The ability to fine-tune the perovskite composition and incorporate various additives and interface modifiers has enabled continuous enhancements in charge carrier dynamics, light harvesting, and overall device performance. Furthermore, the development of new perovskite compositions, such as the incorporation of mixed cations and halides, has led to significant improvements in stability and resistance to environmental factors like moisture and heat. For instance, the use of Cs as the A-site cation, in combination with formamidinium (FA) and methylammonium (MA), has resulted in highly stable perovskite compositions with improved thermal and moisture resistance compared to their single-cation counterparts [19]. The remarkable progress in PSC technology has highlighted the potential of these materials for various applications, including space photovoltaics, where their unique properties and potential to withstand the harsh conditions of the space environment make them an attractive candidate for powering future space

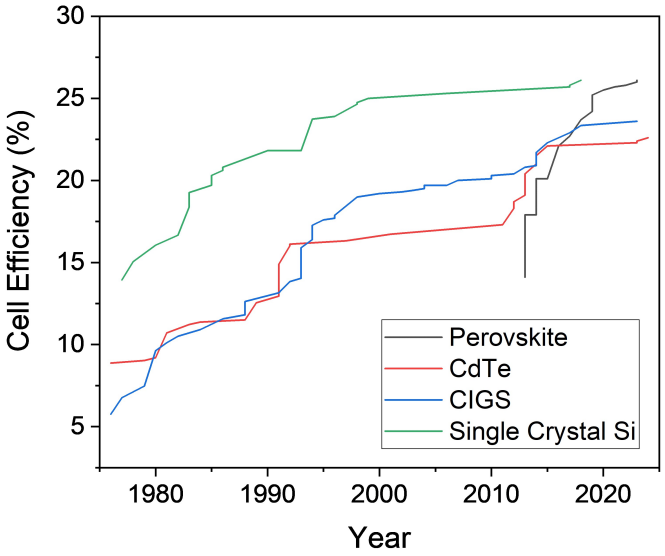


Figure 2.3: Best research cell efficiencies. *Power conversion efficiency (PCE) plotted over time for non-concentrator perovskite, CdTe, CIGS, and single crystal Si devices. Perovskite and Si are currently tied at 26.1%. Data provided online by NREL [1].*

missions.

2.3 Advantages of Metal Halide Perovskites for Photovoltaics

Metal halide perovskites possess a unique combination of properties that make them highly attractive for photovoltaic applications on Earth and in space:

1. High Absorption Coefficients: MHPs exhibit strong light absorption across the visible and near-infrared spectrum with absorption coefficients on the order of 10^4 to 10^5 cm^{-1}, enabling efficient light harvesting in films as thin as a few hundred nanometers [20]. This exceptional light absorption capability is a result of the unique electronic structure and direct bandgap nature of perovskite materials. The high absorption coefficients allow for the realization of thin-film solar cells with remarkably short optical paths, minimizing bulk recombination losses and enabling efficient charge collection. This attribute is particularly advantageous for space applications, where weight and volume constraints are critical, as thinner absorber layers translate to lighter and more compact solar cell modules.

2. Long Charge Carrier Diffusion Lengths: Perovskites exhibit exceptional charge carrier diffusion lengths, ranging from hundreds of nanometers to several micrometers, which far exceed the typical film thicknesses used in PSCs [21]. These long diffusion lengths facilitate efficient charge extraction and high photocurrent generation, even in relatively thick absorber layers. This unique property allows for greater flexibility in device design, as thicker perovskite films can be employed to enhance light absorption without compromising charge collection efficiency. Additionally, the long diffusion lengths contribute to the defect tolerance of perovskites, as charge carriers can traverse longer distances before encountering recombination centers, resulting in improved device performance and stability.

3. Low Non-radiative Recombination Rates: Non-radiative recombination processes, where charge carriers recombine without emitting photons, are detrimental to solar cell efficiency as they reduce the number of charge carriers available for generating electricity. The low non-radiative recombination rates in perovskites can be attributed to their unique defect physics and the presence of shallow defect energy levels [9]. These shallow defects act as benign traps, allowing for the temporary trapping and subsequent release of charge carriers without significant energy loss. As a result, perovskite solar cells can maintain high open-circuit voltages and fill factors, leading to superior power conversion efficiencies.

4. Low-cost Solution Processing: One of the major advantages of PSCs is their compatibility with cost-effective solution-based fabrication techniques, such as spin-coating, blade-coating, or inkjet printing [22]. Unlike many conventional photovoltaic technologies that rely on expensive vacuum deposition methods or high-temperature processing, perovskite solar cells can be manufactured using solution-based techniques that are scalable and economical. The ability to process perovskites from solution allows for the use of roll-to-roll or other high-throughput manufacturing methods, enabling the mass production of perovskite solar modules at low cost.

5. Lightweight and Flexible: The thin-film nature of perovskite solar cells allows for the realization of lightweight and flexible device architectures, making them well-suited for space applications where weight and volume constraints are critical [23]. The ability to deposit perovskite absorber layers on lightweight, flexible substrates, such as metal foils or plastic films, enables the development of solar arrays that can be easily integrated into spacecraft structures or deployed in various configurations. This unique attribute addresses one of the primary challenges in space photovoltaics, where minimizing payload weight is essential for reducing launch costs. Furthermore, the flexibility of PSCs opens opportunities for innovative design and deployment strategies, such as stowing compact solar arrays during launch and unfurling them in space to maximize surface area for energy generation.

These remarkable properties have propelled perovskite solar cells to achieve power conversion efficiencies exceeding 26% in laboratory settings, rapidly bridging the gap with established thin-film photovoltaic technologies like cadmium telluride (CdTe) and copper indium gallium selenide (CIGS). The combination of high efficiency, low cost, and unique form factors make perovskite solar cells an attractive solution for meeting the growing energy demands of space missions while enabling new frontiers of exploration.

2.4 Low Earth Orbit Environment and Challenges

The LEO environment presents a unique and formidable set of challenges for spacecraft and their onboard systems, including photovoltaic devices. Understanding and mitigating these challenges is crucial for designing robust, reliable, and long-lasting space-based technologies. The harsh conditions of LEO can have a significant impact on the performance and lifetime of solar cells, making it imperative to address these factors in the development of advanced photovoltaic solutions [24–29].

One of the primary concerns in LEO is the constant exposure to various forms of particle radiation, including galactic cosmic rays (GCRs), solar particle events (SPEs), trapped radiation belts, and other sources such as neutrons and alpha particles. These energetic particles can penetrate deep into materials, causing ionization damage, displacement of atoms, and the formation of defects and trapping centers within the semiconductor lattice of solar cells [30–33]. The effects of particle radiation on solar cells can manifest in various ways, including decreased efficiency, reduced open-circuit voltage, increased dark current, and in severe cases, complete device failure [34, 35]. Energetic particles can disrupt the delicate charge carrier dynamics within the solar cell, leading to increased recombination and reduced charge collection efficiency. While terrestrial solar cells are designed to operate under the Air Mass 1.5 (AM1.5) solar spectrum, which accounts for the attenuation and scattering of sunlight by the Earth's atmosphere, space-based photovoltaics encounter the unfiltered AM0 solar spectrum. This spectrum, directly from the Sun, is characterized by a higher intensity of ultraviolet (UV) radiation compared to the terrestrial case. The increased UV radiation in the AM0 spectrum can have detrimental effects on solar cell materials, leading to increased photodegradation and material damage [36, 37]. UV photons possess higher energy than visible and infrared photons, making them more capable of breaking chemical bonds and inducing structural changes within the solar cell materials [38]. This can result in the formation of defects, changes in optical properties, and increased rates of photo-oxidation and photo-induced degradation mechanisms. To mitigate the effects of UV radiation, solar cell designs for space applications often incorporate specialized encapsulation materials and coatings that provide effective UV filtering and shielding.

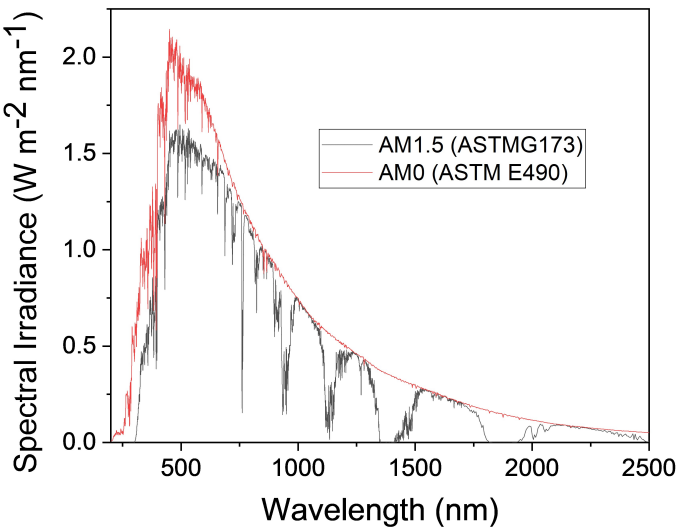


Figure 2.4: AM0 and AM1.5 solar spectra. *AM1.5 solar irradiance standard for Earth-based devices (grey line) and AM0 spectra incident on devices in low Earth orbit (red line). Note the greater UV and visible light intensity of the AM0 spectrum. The integrated UV intensity (below 400 nm) of AM0 is 2.25 times larger than that of the AM1.5 spectrum.*

As spacecraft orbit the Earth, they experience extreme temperature fluctuations due to the periodic transition between direct sunlight exposure and eclipse periods in the Earth's shadow. This thermal cycling can induce significant mechanical stress and strain within the solar cell materials and device structures, potentially compromising their structural integrity and performance. During periods of direct sunlight, solar cells can reach temperatures well above 100 °C, while during eclipse periods, temperatures can plummet to below 0 °C [39]. These rapid and repeated temperature changes can cause differential thermal expansion and contraction of the various materials within the solar cell, leading to the formation of cracks, delamination, and other mechanical failures. Furthermore, the temperature extremes themselves can have a direct impact on the electronic properties and charge carrier dynamics within the solar cell materials [40, 41]. Low temperatures can lead to reduced carrier mobility and increased recombination rates, while high temperatures can accelerate degradation mechanisms and destabilize the material structures [42]. Effective thermal management and the selection of materials with well-matched thermal expansion coefficients are crucial considerations in the design of solar cells for space applications. Specialized encapsulation techniques, such as the use of lightweight and thermally stable composites, can help mitigate the effects of thermal cycling and ensure long-term durability and performance.

The space environment is replete with charged particles, which can accumulate

on the spacecraft's surface and generate electrostatic discharges (ESDs). These high-energy discharges can potentially damage sensitive electronic components, including solar cells, if appropriate mitigation measures are not implemented [43]. ESDs occur when the accumulated charge on a spacecraft's surface exceeds the breakdown voltage of the surrounding medium, resulting in a rapid and localized transfer of charge. This discharge can generate intense electromagnetic arcs and transient currents, which can cause permanent damage to solar cells and other onboard electronics. Protecting solar cells from ESD events is crucial for maintaining their functionality and reliability in space. All flight samples discussed herein utilized a conductive back carrier sheet to electrically "ground" the device to the space station.

In LEO, atomic oxygen (AO) is present due to the dissociation of molecular oxygen by solar radiation. This highly reactive species can degrade and erode materials, posing a threat to the long-term performance and durability of solar cells and other exposed components [44]. Atomic oxygen can react with organic materials, causing oxidation and erosion, which can lead to the degradation of protective coatings, encapsulants, and even the semiconductor materials themselves. This phenomenon is particularly relevant for organic-inorganic hybrid perovskite solar cells, where the organic components may be susceptible to AO attack. Mitigating the effects of atomic oxygen requires robust protective coatings. As discussed in future chapters, each flight sample was encapsulated in at least 1 mm of glass, providing excellent AO protection.

In summary, the LEO environment presents a multitude of challenges for solar cells and spacecraft systems, ranging from particle radiation and thermal cycling to ESDs and AO erosion. Addressing these challenges requires a comprehensive understanding of the space environment, advanced materials engineering, and innovative design strategies to ensure the reliability and longevity of space-based photovoltaic technologies.

2.5 Metal Halide Perovskites for Space PV

The unique combination of radiation tolerance, tunable optoelectronic properties, and lightweight yet high-performance characteristics make perovskites an attractive solution for meeting the power demands of space missions [45–48]. One of the most significant advantages of perovskites for space applications is their demonstrated radiation tolerance [30, 49–56]. Conventional semiconductor materials, such as silicon and III-V compounds, are susceptible to performance degradation and structural damage when exposed to high-energy particle radiation in space. Perovskites, on the other hand, have exhibited promising resistance to radiation-induced defects, owing to their unique defect physics and self-healing capabilities. The soft ionic nature of the perovskite lattice allows for dynamic structural rearrangements and the migration of ions and vacancies, enabling the material to self-heal and recover from radiation-

induced damage. The defect tolerance and self-healing properties of perovskites are attributed to their unique bonding characteristics and the presence of shallow defect energy levels. These shallow defects act as benign traps, allowing for the temporary trapping and subsequent release of charge carriers without significant energy loss or permanent damage to the material.

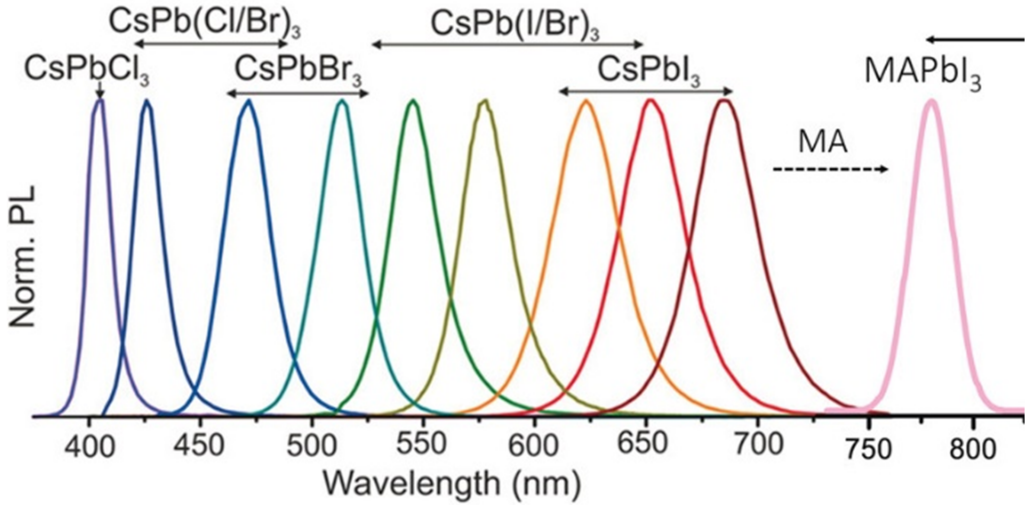


Figure 2.5: Tuning MHP bandgap. *For lead-based perovskites, varying cation and halide concentrations can tune the bandgap from 1.55 to 3.1 eV (800 to 400 nm). Reproduced with permission from Wiley and Sons.*

One of the remarkable features of perovskites is the ability to precisely tune their bandgap by adjusting chemical composition. By incorporating different halide ions (e.g., I^-, Br^-, Cl^-) or mixing cations at the A-site (e.g., MA^+, FA^+, Cs^+), researchers can tailor the bandgap of perovskites to match the AM0 spectrum and increase efficiency (Fig. 2.5) [57, 58]. This is particularly advantageous for space applications, where every incremental increase in efficiency translates directly to reduced payload weight and increased mission capabilities. As an additional benefit, more complex MHPs with multiple cations and halides tend to have higher PCEs [59].

Many conventional solar cell technologies, such as silicon and thin-film technologies like cadmium telluride (CdTe) and copper indium gallium selenide (CIGS), suffer from reduced performance at low temperatures. This is a significant challenge for space applications, where solar cells may experience extreme cold conditions during eclipse periods or in deep space missions. In contrast, perovskites have demonstrated exceptional low-temperature operation, maintaining high efficiencies even at temperatures as low as -150 °C [60–62]. This unique characteristic is attributed to the specific charge carrier dynamics and transport mechanisms within the perovskite material, which are less susceptible to performance degradation at low

temperatures compared to other thin film semiconductors [63, 64]. This outstanding low-temperature performance makes perovskites well-suited for space missions where extreme thermal cycling and extended periods of cold are expected.

The thin-film nature of perovskite solar cells enables the realization of lightweight and high specific power (power-to-weight ratio) devices. Perovskite absorber layers can be deposited as thin as a few hundred nanometers while still maintaining high absorption and efficient charge collection. High specific power devices help minimize payload weight, directly impacting launch costs and mission feasibility [65]. Additionally, the lightweight and flexible nature of perovskite solar cells opens opportunities for innovative design and deployment strategies, such as stowing compact solar arrays during launch and unfurling them in space to maximize the available surface area for energy generation.

In addition to their high performance and unique form factors, perovskite solar cells offer the potential for cost-effective manufacturing at scale. The solution-processable fabrication of perovskites enables low-cost deposition techniques such as spin-coating, blade-coating, or inkjet printing, in contrast to the expensive vacuum deposition methods or high-temperature processing required for many conventional PV technologies [66–68]. This allows for roll-to-roll or other high-throughput manufacturing methods, enabling the mass production of perovskite solar modules [69, 70]. Furthermore, the low-temperature processing and abundance of constituent elements in perovskites contribute to their potential for sustainable and environmentally friendly manufacturing processes.

In summary, metal halide perovskites possess a unique combination of properties that make them well-suited for space PV applications, including radiation tolerance, tunable bandgaps, low-temperature performance, high specific power, and cost-effective manufacturing. As research continues to advance, perovskites hold great promise for revolutionizing the way future space missions are powered and enabling new frontiers of exploration.

Chapter 3

13^{th} Materials International Space Station Experiment

Most material presented in this chapter was published in *Advanced Energy Materials* in 2023 [2].

While combined stressor tests of Metal Halide Perovskites (MHPs) are vital for understanding their viability in space, researchers currently have no way of fully reproducing the conditions of low Earth orbit (LEO). Prior to this work, several MHP devices were briefly carried to the edge of space aboard high-altitude balloons and a sounding rocket [27, 40, 61, 71]. The duration of these missions, some as short as 6 minutes, revealed few insights of MHP degradation or performance. In this chapter, we report optical analysis of the first MHP flown in LEO aboard the 13^{th} Materials International Space Station Experiment (MISSE-13). This prototype, referred to moving forward as the MISSE-13 flight sample, provided data allowing us to determine MHP response to the harsh LEO stressors. Ultimately, the sample experienced no non-reversible degradation after 10 months outside the International Space Station (ISS). This encouraging result motivated the experiments in the remaining chapters of this thesis.

3.1 Mission Timeline

A batch of methylammonium lead iodide ($CH_3NH_3PbI_3$ or MAPI) samples was fabricated by William Delmas at Case Western Reserve University's Materials for Opto-Electronics Research and Education (MORE) Center in July 2019 for an experiment to test MHP encapsulation methods for space operation. Three champion devices were chosen from this batch to serve as the flight and (two) control samples for a last-minute opening aboard the MISSE-13 mission in October 2019. Architecture of the flight and ground control 'A' samples are presented in Fig. 3.1A, while a second

ground control 'B' sample without the SiO_2 layer is shown in Fig. 3.1C. The two SiO_2 samples traveled to Alpha Space Test and Research Alliance, LLC in Houston, TX for environmental testing including a high vacuum bakeout at 60 °C for 25 hr and 3-axis vibration at 4.5 G_{rms} (where 1 G_{rms} = 9.8 m/s^2). They were exposed

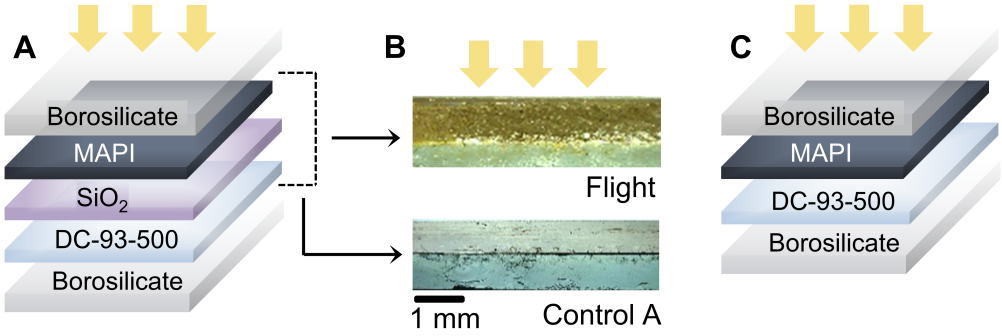


Figure 3.1: MISSE-13 sample schematics and edge images. *(A) Schematic of assembled layers for flight sample and control A. (B) Photographs of edges of (top) flight and (bottom) control A samples after the former's return. (C) Schematic of assembled layers for control B without SiO_2. Bold arrows indicate direction of illumination on the ISS. Reproduced with permission from Wiley and Sons [2].*

to ambient conditions in Florida for ≈ 5 months during payload integration. The flight sample was loaded onto a SpaceX Falcon 9 rocket and launched on the 20^{th} Commercial Resupply Service mission (CRS-20) on March 7, 2020. At this time, control A was returned to NASA Glenn for storage. Aboard the ISS, the flight sample was deployed on the MISSE-Flight Facility platform in zenith (sun-facing) orientation between March 2020 and January 2021 as depicted in Fig. 3.2. The sample was electrically connected to the platform with a conductive carrier sheet to prevent electrostatic discharge to the ISS. The MISSE-13 mission concluded with the landing of SpaceX CRS-21 on January 14, 2021. The flight sample was returned to NASA Glenn two months later. The author's role in this project began in July 2021 with post-flight characterization of all samples two years after fabrication.

3.2 Sample Fabrication Details

The perovskite precursor solution (ink) was purchased from Sigma Aldrich and consisted of a 1:1 ratio of CH_3NH_3I and PbI_2 suspended in dimethylformamide (DMF). The space-qualified Dow Corning (DC) 93-500 encapsulant used to seal the devices is a silicone elastomer formed by mixing its base and hardening agent in a 10:1 ratio, then degassing at 40 °C in a vacuum oven [72]. The fabrication steps were as follows. First, 30 µL of perovskite ink was drop cast onto a 1 x 1 in borosilicate glass slide. It

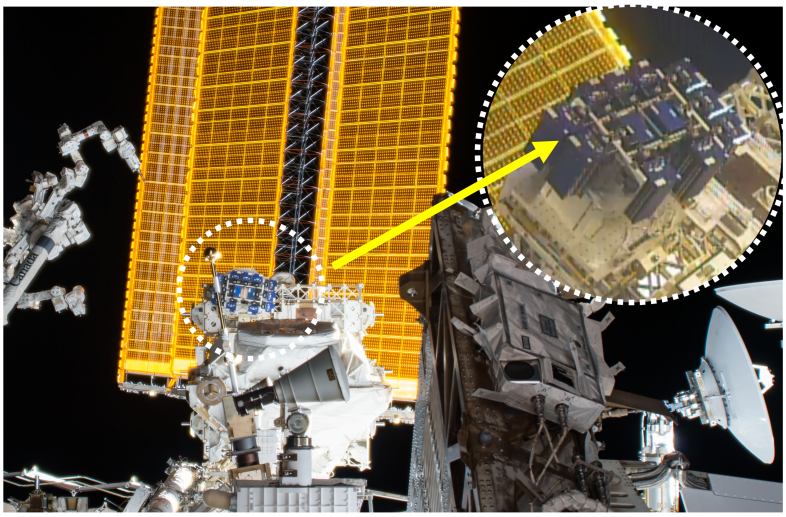


Figure 3.2: MISSE flight facility platform. *The MISSE-13 flight sample was deployed in the zenith orientation, pointing outward normal from the Earth's surface. Reproduced with permission from Wiley and Sons [2].*

was spun at 2000 rpm for 90 s, then annealed at 100 °C for 60 min. In the first few seconds on the hot plate, the yellow precursor solution turned to the characteristic black of a perovskite thin film. A cotton swab dipped in DMF was used to remove the edges of the film from the glass substrate. Between 50 nm and 150 nm of SiO_2 was deposited on the flight sample and control A with an Anstrom Instruments Chemical Vapor Deposition system. All samples were then moved from the glovebox to the fume hood for encapsulation. Finally, 1 mL of DC 93-500 was dropped onto the surface of each sample and a 1 x 1 in piece of glass was pressed on top to fully spread the silicone and seal the sample. SiO_2 was chosen as an additional barrier layer to supplement the DC 93-500 and help protect the samples from moisture and oxygen in the original encapsulation experiment. As such, samples with SiO_2 were chosen for the flight and control A samples for the MISSE-13 mission. A sample without SiO_2 was included as an additional control, which ultimately provided essential data for comparison.

3.3 Results and Discussion

3.3.1 Optical Characterization

The MISSE-13 flight sample returned to Earth with little visual change in its MHP layer, few signs of degradation, and a strong photoluminescent signal. Fig. 3.1B

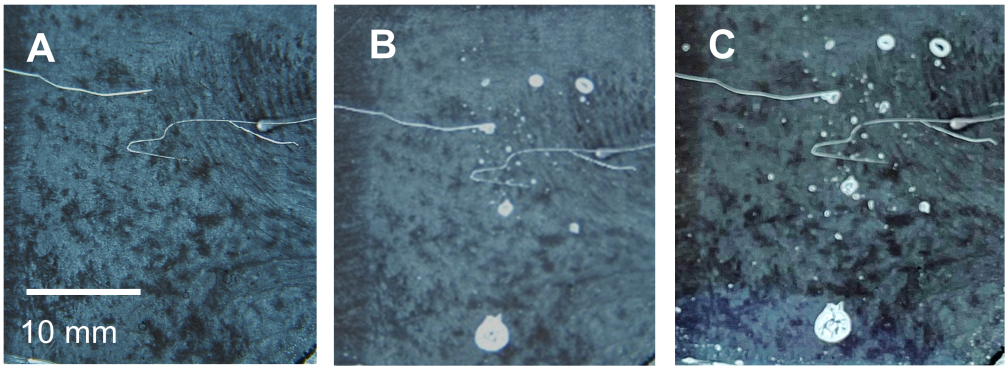


Figure 3.3: MISSE-13 flight sample photographs. *(A) Immediately after fabrication, (B) 290 hr after fabrication, and (C) post flight. Reproduced with permission from Wiley and Sons [2].*

shows side-view images of the flight and control A samples after the former's return. The sun-facing glass of the flight sample significantly yellowed during flight, typical of electron irradiation in borosilicate glass [51, 73]. Ceria-doped borosilicate glass is often used for space applications because of its radiation resistance [73–75]. Such glass is generally 0.005 in thick and was not practical or available for the original encapsulation study the MISSE-13 samples were fabricated for. Photographs of the flight sample immediately after fabrication, 290 hr after fabrication, and postflight

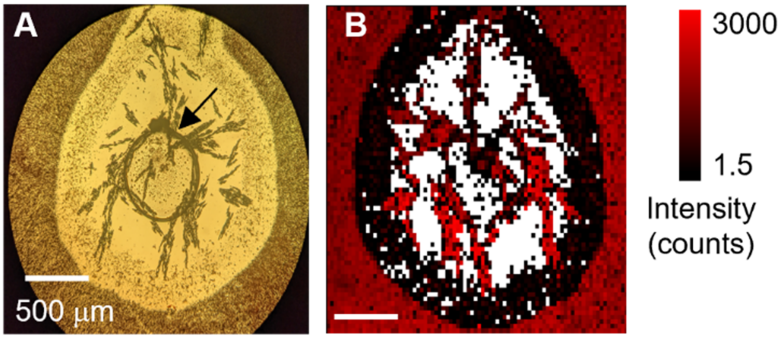


Figure 3.4: Assessing the damaged regions. *(A) Magnified optical image of the damaged region shows a bubble trapped in the encapsulant, indicated by an arrow. (B) Scanning photoluminescence spectroscopy of the same region shows the variation in intensity. White regions indicate no emission signal. Reproduced with permission from Wiley and Sons [2].*

are provided in Fig. 3.3A-C, respectively. Here, we observe the formation of spots on

the film. The sample was stored in an ambient environment between Fig. 3.3A and Fig. 3.3B to assess its chemical and optical degradation. High-resolution photoluminescence (PL) mapping of the largest spot (bottom center, Fig. 3.3B-C) revealed these areas to be localized degradation from bubbles formed within the DC 93-500 encapsulant. Fig. 3.4A provides an optical microscope image of this spot, and Fig. 3.4B depicts the same area as a 10,000-point PL map.

In this scan, emissive perovskite around the spot became darker as it approached the bubble. Since these devices were encapsulated in the ambient air of a fume hood, this is indicative of degradation from moisture trapped within the bubble [76–78]. These optically non-responsive areas remained localized after their formation pre-flight, and these regions were not further damaged from the space environment.

3.3.2 Photoluminescence Spectroscopy

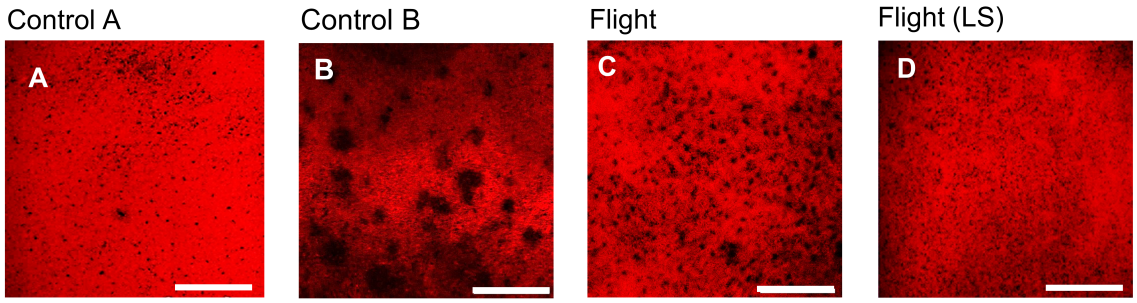


Figure 3.5: Confocal Fluorescence Imaging. *Spatial fluorescence images of (A) control A, (B) control B, (C) flight sample, and (D) flight sample after 15 hr AM1.5 light soaking. Red regions are light emitted from samples between 1.55 – 1.65 eV. Dark areas are non-emissive in this energy range. Scale bars 250 µm. Reproduced with permission from Wiley and Sons [2].*

Since all samples in this study were electrically insulated and fully encased in glass, we were required to probe them with exclusively optical techniques. Fluorescence confocal microscopy as depicted in Fig. 3.5 provides spatial emission information, allowing the user to better understand the quality of the films, substrate coverage, and degree of degradation. With an LSM 880 confocal microscope system, a 405 nm (3.06 eV) laser was used to excite the samples and emitted light was collected between 1.55 – 1.65 eV. This wavelength range is represented as red in Fig. 3.5, while the black areas are non-emissive in this range. These dark areas were, however, found to be emissive between 2.5 – 2.7 eV, indicative of PbI_2 emission shown as green in Fig. 3.6 [35, 79]. PbI_2 isolation from the MAPI lattice is a clear sign of degradation

in the presence of moisture and oxygen. Thus, the regions which appear black in the 1.55 – 1.65 eV (red) confocal images are an excellent gauge of spatial degradation within the MISSE-13 samples. Quantifying the size of each dark region and the total

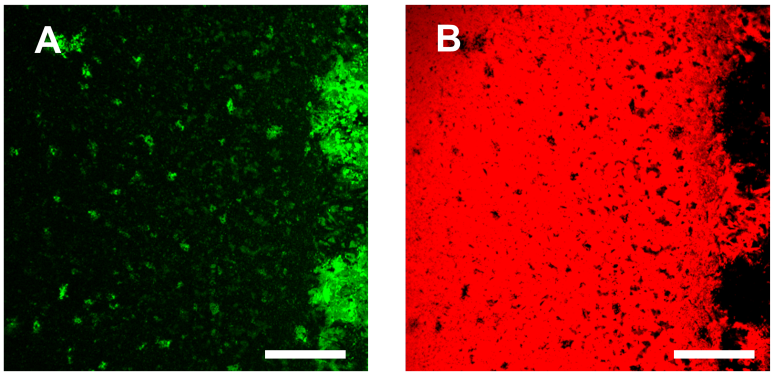


Figure 3.6: Investigation of dark regions. *Spatially-resolved maps of PL intensities of the flight sample centered at emission energy in the range (A) 2.5 – 2.7 eV and (B) 1.55 – 1.65 eV. Comparison of the two maps confirm that the non-emissive regions of the MAPI films are PbI_2. Scale bars 200 µm. Reproduced with permission from Wiley and Sons [2].*

percent dark area in ImageJ allows for a more detailed analysis of PbI_2 formation. This information is provided in Fig. 3.7 for all three samples. In agreement with Fig. 3.5, control B has a small number of large dark regions, control A has a large number of very small dark regions, and the flight sample is somewhere between. Overall, 13% of the flight sample returned non-emissive, while only 4% of control A was dark. The increased damage in the flight sample was reversable and will be discussed further in the next section. Fig. 3.5 and 3.7 demonstrate the effectiveness of the vapor deposited SiO_2 layers on the flight and control A samples. Without this protective layer, control B's surface was 23% non-emissive, nearly six times that of the otherwise identical control A. To better understand the effect of these dark regions on film quality, high-resolution PL maps were taken of each sample in a 500 x 500 μm^2 grid. The emitted light from each sample passed through a beamsplitter to be analyzed both spectrally and temporally. From these two methods we fully described the PL intensity, energy, and full width at half maximum (FWHM) of the Gaussian signal, as well as the charge recombination lifetime of the perovskite. The lifetimes and energies of all samples are provided in Fig. 3.8A and B, respectively. First, note the significant energetic blue-shift of control B compared to control A. PbI_2 inclusion within the MAPI lattice has been shown to increase emission energy [78]. However, the flight sample returned with the largest blue-shift and approximately half the total dark area as control B. Similarly, the characteristic recombination lifetime τ was lowest for

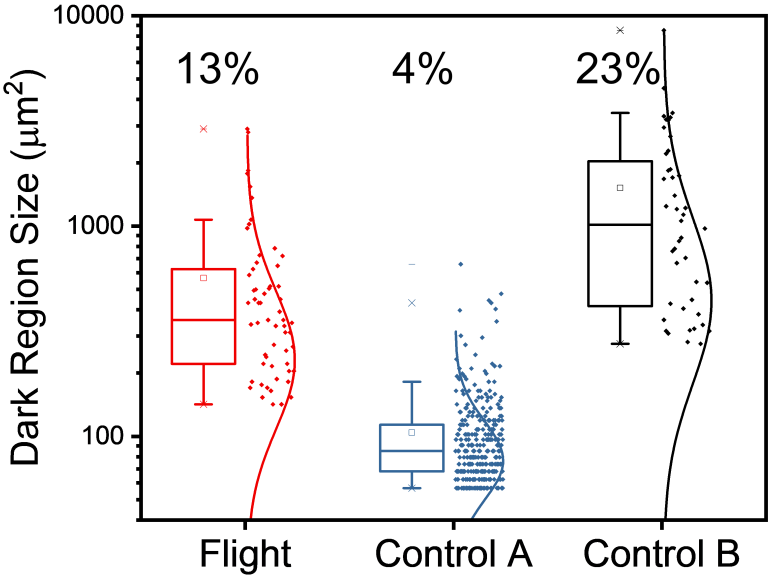


Figure 3.7: Quantification of dark confocal regions. *ImageJ analysis of confocal maps for flight and both control samples. Individual dark spots are represented as jittered points with corresponding distribution envelope and boxplot. Total percent dark area for each sample listed above each boxplot.*

the flight sample postflight and highest for control A. Combined with the confocal data, these data indicate that PbI_2 was unlikely to be the cause of PL variation in the flight sample. More plausible is the residual strain to the film that developed during the $\approx$ 4800 orbits around the Earth during its 10-month journey. Thermal strain is calculated as the temperature difference (compared to the sample's 100 °C annealing temperature) multiplied by the difference in thermal expansion coefficient between device layers ($\varepsilon_t = \Delta\alpha\Delta T$). Thermal cycling on the ISS was modeled for a uniform temperature plate with its top surface exposed to sunlight and its bottom surface thermally isolated. From this simulation, the transient heat equation was solved numerically to provide sample temperature at all points in the $\approx$ 90 min orbit. The results of the simulation are presented in Fig. 3.9. During the cold, dark half of the orbit (Fig. 3.9A), substantial microscopic tensile strain develops within the perovskite film in the x and y-directions (Fig. 3.9B). This is caused by the film attempting to contract at low temperature, but being fully constrained in x and y-directions due to thermal expansion mismatch with the glass and SiO_2. Thus, there is no macroscopic strain in the x and y-directions. However, the microscopic tension in the x and y-directions produces a compressive microscopic strain within the MAPI in the z-direction due to the Poisson effect (Fig. 3.9C). The Poisson effect describes the expansion or contraction of a material along a perpendicular axis to the direction

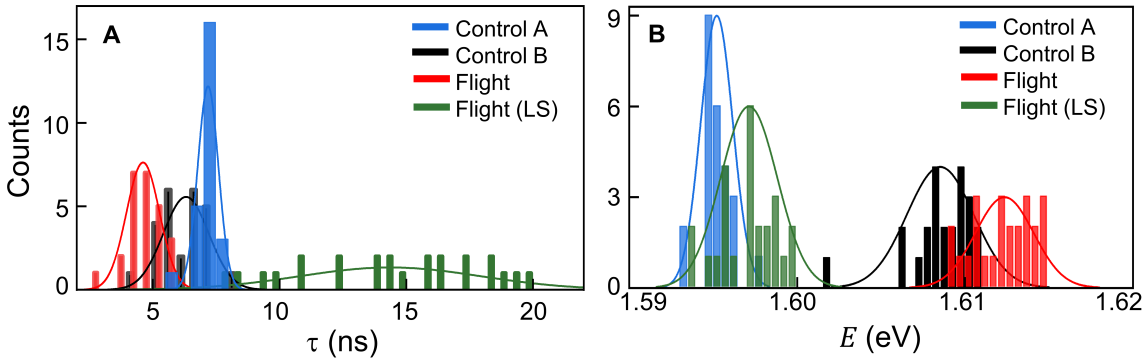


Figure 3.8: Spatial PL distributions. *Histograms of (A) radiative charge recombination lifetime and (B) peak emission energy for each sample over a 500 x 500 μm area. Reproduced with permission from Wiley and Sons [2].*

of applied force. In this case, the z-direction strain is computed as product of twice the Poisson ratio and the thermal strain ($\varepsilon_{z,\ micro} = 2\nu\varepsilon_t$). Since the layers are not constrained in the z-direction, this produces a macroscopic strain in the z-direction (Fig. 3.9D). The dashed line in Fig. 3.9D represents the z-direction strain for a fully unconstrained MAPI film. The shaded region between the dashed and solid line is thus the effect of the microscopic x and y-direction strain from the Poisson effect. Overall, the combined strain magnitudes of the x and y-directions are larger than the strain in the z-direction, so the strain in the film is expected to be largely tensile. At low temperatures, the maximized tensile strain can lower the valence band edge and increase bandgap, producing the observed PL blue-shift in the flight sample [80].

3.3.3 Photostability

After initial optical characterization, all three samples were exposed to simulated AM1.5 sunlight for 15 hr while their PL spectra was measured every 5 minutes. MHP light soaking (LS) experiments can be complicated; the exact architecture and quality of a device, as well as temperature and length of exposure can produce significantly different results [35, 79]. The spectrally integrated PL intensities of Fig. 3.10A show initial photodarkening of all samples for the first hour, then photobrightening for the flight and control A samples for the remaining 14 h. Control B slowly darkens during the remainder of the exposure, ultimately degrading into PbI_2 and turning yellow (Fig. 3.10A, inset). MHPs are believed to immediately begin their darkening and brightening processes upon exposure to light, with one effect ultimately dominating [81]. Photodarkening is a result of MAPI degradation, while photobrightening can be driven by light-induced strain relief, photogenerated carriers passivating trap states,

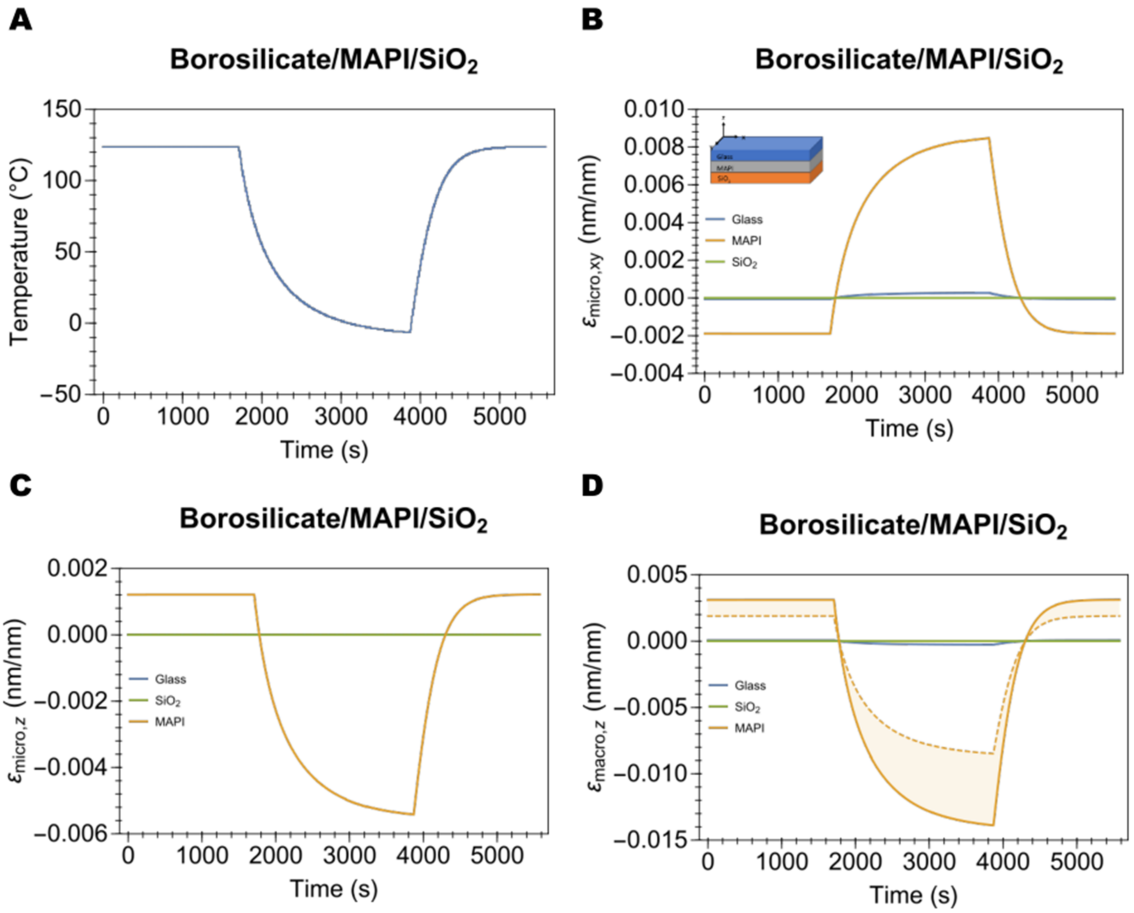


Figure 3.9: Thermal cycling and strain aboard the ISS. *(A) Modeled sample temperature during one ISS orbit. (B) Microscopic strain in the x and y-directions for the MAPI film and both layers in contact with it (glass and SiO_2). (C) Microscopic and (D) macroscopic strain in the z-direction for all modeled layers. Microscopic strains refer to change in length along a given crystalline axis due to thermal effects, while macroscopic strains are overall changes in the dimensions of the entire device layer. Macroscopic strains in the x and y-directions are zero because the MAPI film is fully constrained by the glass and SiO_2. Positive strains indicate tensile strains, while negative strains indicate compressive strains. Reproduced with permission from Wiley and Sons [2].*

or a combination of both [82, 83]. As these non-radiative recombination sites are reduced, charges are able to recombine and produce a photon, increasing integrated PL intensity. Both control samples experience spectral broadening in Fig. 3.10B, while the flight sample remains very stable throughout the 15 h. The control B spectrum

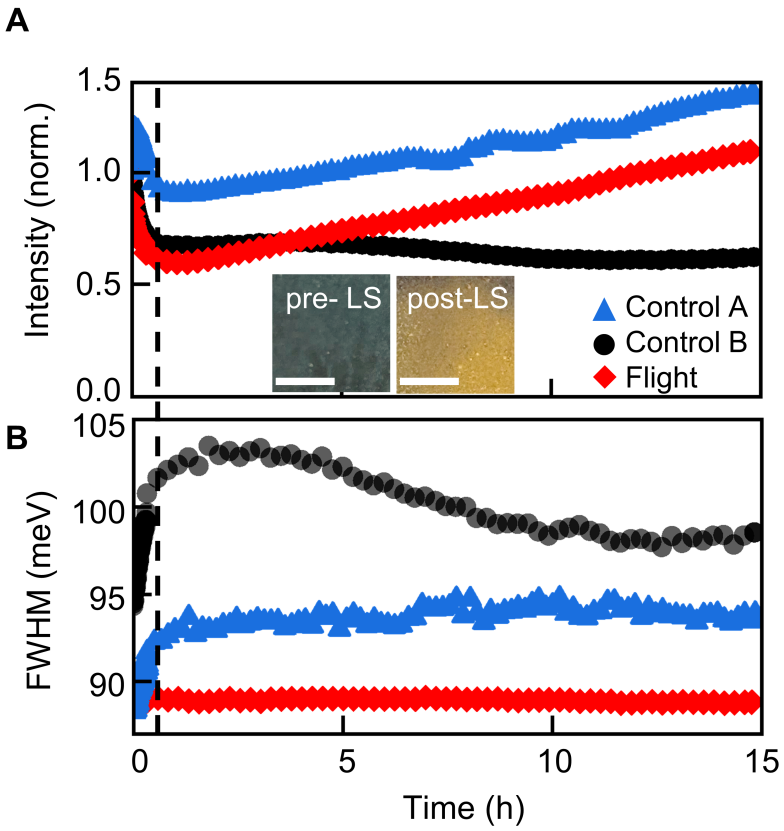


Figure 3.10: Evaluating device stability under AM1.5 light soaking. *(A) Spectrally integrated PL intensity and (B) spectral FWHM of PL signal recorded every 5 minutes for 15 hours of continuous AM1.5 illumination. The simulated solar spectrum was filtered with a 675 nm short-pass filter before reaching the samples to allow measurement of the PL signal. Inset of (A) are photographs of control B before and after light soaking, depicting widespread photodegradation and color change indicative of PbI_2 formation. Scale bars 1 mm. Reproduced with permission from Wiley and Sons [2].*

broadens much more than control A due to the PbI_2 formation in agreement with the photodarkening in Fig. 3.10A. While control A undergoes little visual change after LS, the increase in spectral FWHM suggests formation of defect states from MAPI degradation, also seen in lifetime shortening post-LS (Fig. 3.11). The photobrightening and FWHM stability of the flight sample suggest light-induced lattice expansion relieved strain in the film, which has been shown to increase PCE in MHP solar cells [82]. The benefits of light 'wakeup' in MHPs are generally temporary and eventually followed by chemical degradation. No signs of degradation were found in the flight sample post-LS. Instead, clear signs of recovery in both confocal fluorescence (Fig.

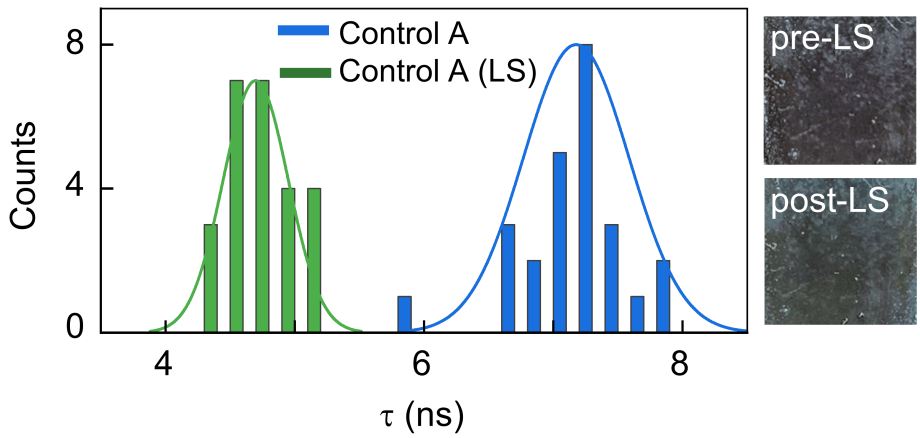


Figure 3.11: Effects of light soaking on control A. *Distribution of charge recombination lifetime across control A before and after 15 hr AM1.5 light soaking. Photographs pre-LS and post-LS provided to the right. Reproduced with permission from Wiley and Sons [2].*

3.5D) and PL metrics (Fig. 3.8) were found in the flight sample. After LS, the dark confocal regions on the flight sample were reduced from 13% to 6% (Fig. 3.5C and D, respectively), indicating reduced defect density on the film surface. Likewise, post-LS PL maps revealed the flight sample had tripled its average postflight lifetime (Fig. 3.8A) and red-shifted its energy close to control A (Fig. 3.8B). These optical changes indicate that the LS test provided enough photogenerated carriers to the flight sample to allow the film to relax its strained lattice and behave more like control A.

3.3.4 Temperature Dependent PL

The varying behavior between MISSE-13 samples extends to low temperatures. To remain useful in LEO, MHPs have to withstand rapid and extreme thermal cycling. Between 140 and 160 K, MHPs undergo a structural phase transition from tetragonal to orthorhombic accompanied by an energetic blue-shift [62]. Fig. 3.12A maps the PL intensity of control A as a function of temperature and energy. The emission energy shifts from 1.59 eV to 1.64 eV at $T = 120$ K, also shown in Fig. 3.12D. This transition temperature is additionally marked by a steep narrowing of the FWHM at temperatures below T_C. Thus, the dashed lines in Fig. 3.12D and E mark the phase transition for all samples. $T_C = 120$ K is a slightly lower transition temperature than is usually reported for MAPI films. Control B exhibits $T_C = 148$ K, a more standard value for MHPs (Fig. 3.12D,E). The lower T_C of control A is attributed to the vapor deposited SiO_2 layer, as interfacial strain has been demonstrated to arrest the transition temperature of MAPI by up to 25 K [84, 85]. While the be-

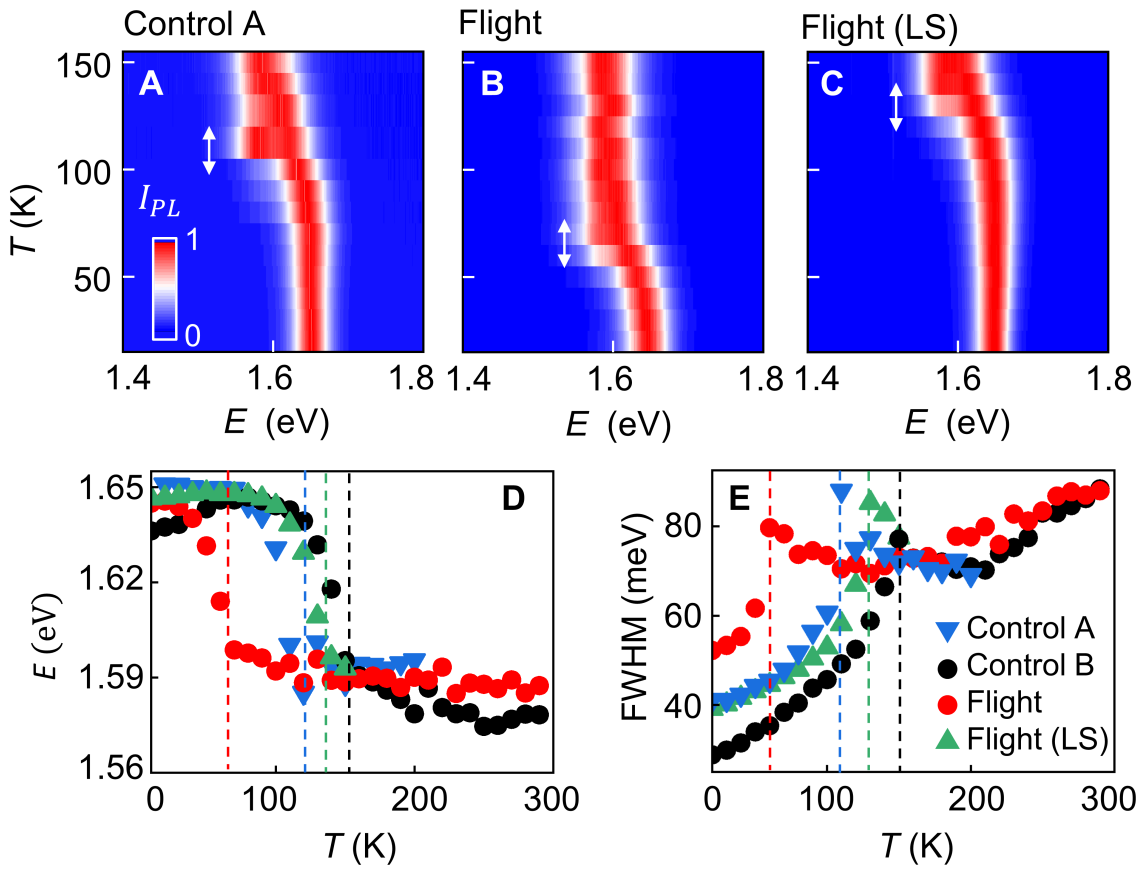


Figure 3.12: Structural phase transition at low temperature. *PL emission intensity mapped as a function of temperature for (A) control A and flight sample (B) before and (C) after light soaking (LS). Phase transition temperature T_C = 56 K for flight sample pre-LS. (D) Peak emission energy and (E) FWHM plotted as a function of temperature for all samples. Dashed lines mark T_C for each sample and show a similar behavior for control A and the flight sample post-LS. Reproduced with permission from Wiley and Sons [2].*

havior of the flight sample matches that of the control samples (Fig. 3.12D,E), its transition temperature was arrested to 56 K post-flight (Fig. 3.12B). This value is extremely low and unexpected. The MHP tetragonal form is disordered such that, as lattice vibrations are removed, the crystal shifts to the orthorhombic phase where the methylammonium ions are better ordered. The low flight T_C is thought to have been caused by the residual tensile strain in the film as discussed in the previous section. MHP nanocrystal studies have demonstrated a lowered, stable T_C due to the high surface-to-volume ratio of the perovskite [86]. This results in surface contributions

to the Gibbs free energy large enough to arrest the transition to the orthorhombic phase of the MHP [87]. After $\approx$ 4800 thermal cycles, it is possible that the strain in the film induced a polymorph which persisted post-flight. Whatever the exact cause of the low T_C, it was finally restored to 130 K after LS, a value comparable to that of control A.

3.4 Conclusion

From the results detailed herein, MHP thin films can clearly survive the LEO environment for 10-months with no non-reversible degradation. The MISSE-13 flight sample returned to Earth thermochemically stable and optically emissive, excellent signs that MHPs are ready for more tests in the hard conditions of space. While the flight sample had the shortest recombination lifetime, highest energy, and lowest phase transition temperature postflight compared to its controls, all three of these characteristics were reversed under 15 hr continuous AM1.5 illumination. Furthermore, both control samples showed signs of degradation during LS tests, with control B degrading into a yellow PbI_2 film. The flight sample showed no signs of degradation from LS, only improving from AM1.5 exposure. The initial lifetime shortening post-flight is certainly worth monitoring for future MHP devices in space, as long lifetimes in a photovoltaic absorber are essential for efficient solar cells. Very short MHP lifetimes will cause charges to recombine before being extracted, ultimately lowering open circuit voltage and efficiency. This chapter proposes that the three abnormalities in the flight sample mentioned above were a result of residual strain in the film from excessive thermal cycling. The LS test thus provided enough photogenerated carriers and phonons to the flight sample to allow the film to relax and eliminate this strain, restoring the sample's lifetime, transition temperature, and peak energy.

Several questions remain from this study, primary of which is the exact cause of the microscopic strain within the sample. The modeled thermal strain along all three axes may induce energetic local minima which activate at lower temperatures than standard MHPs. These states could arise from a combination of defect creation and thermal strain, evidence of each having been observed in the flight sample. Recent studies have reported PL intensity and lifetime decreases in MAPI films caused by repeated structural transitions from 200+ thermal cycles [42, 66]. Similar effects are likely to have occurred during the $\approx$ 4800 orbits of the MISSE-13 mission. Other possible sources of damage within the MHP lattice include ultraviolet (UV) light from the AM0 solar spectrum and particle radiation. The latter is unlikely to have damaged the flight sample due to the protection of its 1 mm thick top glass. This is demonstrated in the SRIM (Stopping and Range of Ions in Matter) and TRIM (Transport of Ions in Matter) simulations of Fig 3.13 [88]. Here, protons with energies of up to 14 MeV are stopped by the 1 mm borosilicate cover glass of the flight sample. The ISS proton fluence for the 10-month journey is estimated at 10^9 cm^{-2}, consisting

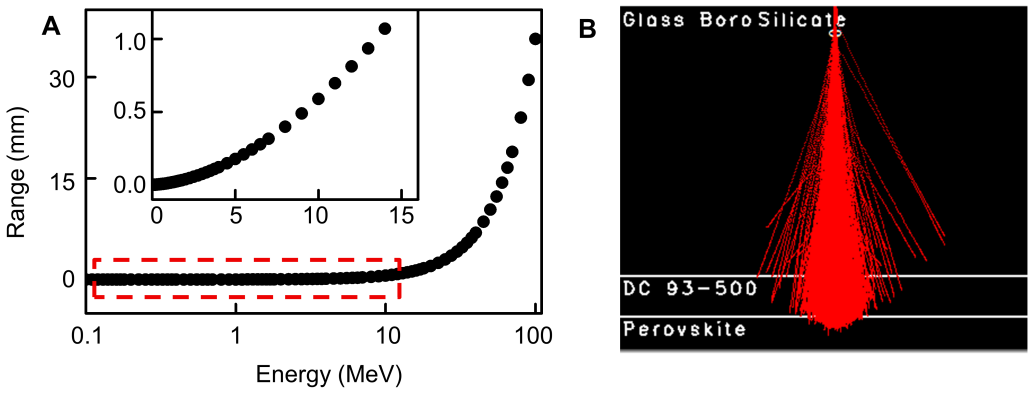


Figure 3.13: The role of particle radiation. *Results of SRIM (Stopping and Range of Ions in Matter) and TRIM (Transport of Ions in Matter) simulations. (A) SRIM penetration depth of protons in borosilicate glass as a function of energy. Inset shows energy of protons within the 1 mm thick cover glass. (B) TRIM ion simulation for perovskite sample using 14 MeV protons. Reproduced with permission from Wiley and Sons [2].*

mostly of lower energy (0.05 – 10 MeV) particles [89]. Thus, particle radiation is not considered a significant source of damage for the MISSE-13 flight sample. The role of space-relevant proton and neutron irradiation of MHPs is investigated further in Chapter 5. The role of UV light in sample strain and degradation remained unclear during MISSE-13 analysis. To isolate various UV and visible bands of the AM0 spectrum during flight, 4 different UV filters were used as the top glass of MHP samples during the MISSE-16 mission. The optical investigation of these samples, as well as their ground controls and a flight control topped with Corning Eagle XG (EXG) glass is detailed in the next chapter. As long as researchers are unable to fully recreate the complex and harsh conditions of LEO in the laboratory, programs such as MISSE will remain essential for testing prototype devices in space. The MISSE-13 MHP flight sample ultimately outperformed its controls and holds the distinction as the first perovskite film to orbit Earth. The success of this sample led the way for additional MHP thin films on MISSE-16 and full solar cells on MISSE-15, discussed in chapters 5 and 4 respectively.

Chapter 4

16^{th} Materials International Space Station Experiment

The material presented in this chapter is currently in preparation for publication.

Although the 13^{th} Materials International Space Station Experiment (MISSE-13) flight sample successfully endured 10 months in low Earth orbit (LEO), the study was not able to fully address the resiliency of metal halide perovskites (MHPs) to the LEO environment. As discussed in Chapter 3, the 1 mm thick borosilicate top glass blocked the majority of particle radiation (mostly high energy protons and electrons) and ultraviolet (UV) radiation. Future MHPs for space use will have significantly thinner top glass materials to reduce the size and mass of the cells. Thus, it is vital to supplement our knowledge of the MISSE-13 mission with experiments that test MHP response to UV and particle radiation separately. The former will be addressed in this chapter, while the latter will be the subject of Chapter 5. Herein, we report optical analysis of five MHP prototype samples flown in LEO aboard the MISSE-16 mission for 6 months. These samples, along with their two ground controls, do not include electrical contacts or charge transport layers, allowing us to focus on changes within the isolated methylammonium lead iodide (MAPI) thin film. These devices were similar to those of MISSE-13 but included different top glass layers to allow specific wavelengths of the extraterrestrial or air mass zero (AM0) solar spectrum to reach the absorber layer. These filters were 2 mm thick compared to the 1 mm cover glass of MISSE-13 devices reducing the amount of particle radiation reaching the MHP layer. The MISSE-16 samples thus received similar stressors as the MISSE-13 flight sample with reduced particle radiation and visible light incident on the perovskite absorber. Ultimately, all MISSE-16 devices returned to Earth with less optical and chemical variation than the MISSE-13 flight sample. This result reflects the shorter flight time of the MISSE-16 samples, greater top glass protection, and high-quality films produced at the National Renewable Energy Laboratory (NREL) for this mis-

sion. The results herein demonstrate MHP resiliency to the AM0 spectrum in orbit and further strengthen the viability of perovskite for use in space applications.

4.1 Mission Timeline

(A)

Sample #	NREL #	Top glass
1	KV366	325-385 nm (control)
2	KV337	EXG glass (control)
3	KV375	325-385 nm
4	KV364	EXG glass
5	KV334	400 nm long pass
6	KV365	240-395 nm
7	KV325	275-375 nm

(B)

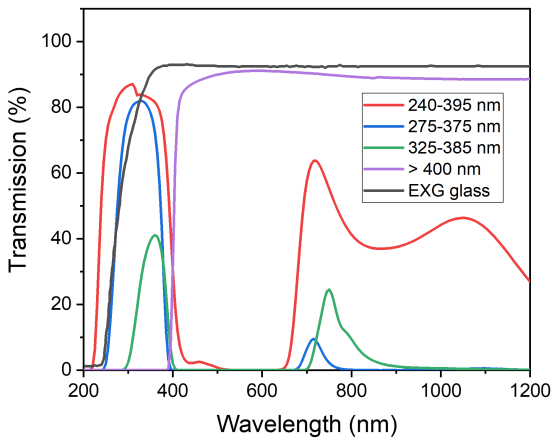


Figure 4.1: MISSE-16 devices. *(A) Table of all flight and control samples included in the MISSE-16 study. (B) Optical transmission of each top glass material. All samples consist of quartz glass/MAPI/DC93-500/top glass. The only difference between samples is the top glass material, as outlined in A.*

Seven methylammonium lead iodide ($CH_3NH_3PbI_3$ or MAPI) samples were fabricated at NREL by Kaitlyn VanSant in September 2021 for the MISSE-16 mission. Five of these samples, each with a different top glass material as described in Fig. 4.1, traveled to Alpha Space Test and Research Alliance, LLC in Houston, TX for environmental testing including a high vacuum bakeout at 60 °C for 25 hr and 3-axis vibration at 4.5 G_{rms} (where 1 G_{rms} = 9.8 m/s^2). The flight samples were loaded onto a SpaceX Falcon 9 rocket and launched on the 25^{th} Commercial Resupply Service mission (CRS-25) on July 15, 2022. Aboard the ISS, the samples were deployed on the MISSE-Flight Facility platform in zenith (sun-facing) orientation between August 2022 and February 2023. The sample was electrically connected to the platform with a conductive carrier sheet to prevent electrostatic discharge to the ISS. The MISSE-16 mission concluded with the landing of SpaceX CRS-27 on April 15, 2023. The flight samples were returned to NASA Glenn one month later. Post-flight characterization of all samples began in July 2023, one and a half years after fabrication.

4.2 Sample Fabrication Details

The perovskite precursor solution (ink) was synthesized by mixing the following materials: 290.2 mg PbI_2, 100 mg CH_3NH_3I, 470 µL dimethylformamide (DMF) 470 µL, 36.7 µL dimethyl sulfoxide (DMSO), and 10.5 µL n-methyl-2-pyrrolidone (NMP). 1 x 1 in quartz substrates were sonicated in acetone and isopropyl alcohol for 10 min each prior to 15 min UV ozone exposure. The perovskite ink was filtered with a 0.2 µm pore filter immediately before blade coating onto the substrates. 18 mL of the ink solution was deposited at the blade edge near the front of the substrate. The blade then moved across the substrate at a speed of 7.5 mm/s while maintaining a height of 150 µm above the substrate surface. Immediately following the ink deposition, a nitrogen quenching step was performed using an air knife positioned 4.4 mm above the stage. Nitrogen gas flowed at 40 psi, as indicated on the fume hood's pressure gauge. 3 or 4 passes with the air knife across the sample were used to convert the freshly deposited perovskite into an intermediate phase. After this quenching step, each sample was transferred to a hot plate and annealed at 140 °C for 2 min to transform the perovskite from the intermediate phase into the final black phase. The final perovskite film was removed from the periphery of each sample with a razor blade in preparation for encapsulation. As with the MISSE-13 samples, the space-qualified Dow Corning (DC) 93-500 silicone elastomer encapsulant was used to encapsulate the devices. First, 3.53 g of the base solution was mixed with 0.36 g of the curing agent in a large vial. The vial was sealed with a rubber septum and attached to a Schlenk line via a needle through the septum. The solution was de-gassed for 20 min at a vacuum level of 100 mTorr to remove trapped bubbles. The DC93-500 was then spread evenly over the surface of each sample and top glass materials specified in Fig. 4.1 were used to seal each device. Finally, the samples were cured at room temperature overnight. A schematic of finished samples is provided in Fig. 4.2A.

4.3 Results and Discussion

4.3.1 Optical Characterization

The MISSE-16 flight samples returned to Earth with fewer signs of degradation than the MISSE-13 flight sample, exhibiting little visual or optical change and a strong photoluminescent signal. Fig. 4.2B shows side-view images of flight samples 5 and 6 post flight. The sun-facing 400 nm long pass filter of sample 5 significantly yellowed during flight, much like the borosilicate glass of the MISSE-13 flight sample (Fig. 3.1B). Since this yellowing is attributed to high-energy electron exposure, it is likely to have occurred in all flight samples. The UV band pass filters such as the 240-395 nm shown in Fig. 4.2B block all visible light and color change cannot be observed. Photographs of all samples post flight are included in Table 4.1. A small number of

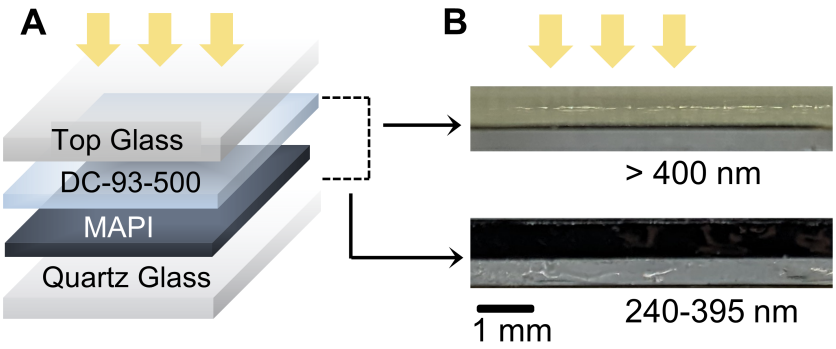


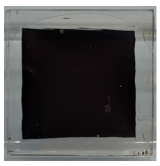
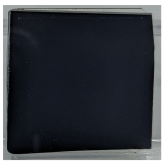
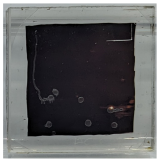
Figure 4.2: MISSE-16 sample schematic and edge images. *(A) Schematic of assembled layers for all seven devices in this study. (B) Photographs of edges of flight samples utilizing as their top glass material (top) 400 nm long pass and (bottom) 240-395 nm band pass filters. (C) Note the similar glass yellowing as the MISSE-13 flight sample (Fig. 3.1B) for the top sample. No color change can be observed in the UV band pass filters, as they block all visible light. Bold arrows indicate direction of illumination on the ISS.*

bubbles within the encapsulant were evident in samples 2 and 5 after the encapsulant fully hardened. There may be similar bubbles in other samples, but the black UV filters prevent proper imaging of the MHP/encapsulant interface. These spots were not accompanied by localized damage as in the MISSE-13 flight sample (Fig. 3.4), likely a result of drier air within the bubbles.

4.3.2 Photoluminescence Spectroscopy

Since all samples in this study were electrically insulated and fully encased in glass, characterization was limited to exclusively optical techniques. Fluorescence confocal microscopy as depicted in Fig. 4.3 provides spatial emission information, allowing the user to better understand the quality of the films, substrate coverage, and degree of degradation. With an LSM 880 confocal microscope system, a 405 nm laser was used to excite the samples and emitted light was collected between 1.55 – 1.65 eV. This wavelength range is represented as red in Fig. 4.3, while the black areas are non-emissive in this range. Unlike the MISSE-13 MAPI films (Fig. 3.6), the MISSE-16 samples appeared extremely uniform under confocal microscopy. Very few regions were non-emissive from pinholes or PbI_2 formation in the film. The spatial photoluminescence (PL) uniformity and high grain density reflect the excellent quality of samples fabricated at NREL. Quantization of non-emissive regions of these samples as seen in Fig. 3.7 was not feasible due to the very small dark regions of the films. While confocal fluorescence microscopy provided useful spatial PL data, it lacked spectral

Table 4.1: ***Photographs of all MISSE-16 samples.*** *Images of all samples described in Fig. 4.1A, taken after flight samples returned from the ISS. UV band pass filters appear black, obscuring the MHP layer in four samples. Of the three visible perovskite films, two (samples 2 and 5) show a small number of bubbles trapped within the DC93-500 encapsulant. All substrates are 1 in^2.*

Sample #	NREL #	Top glass	Sample photograph
1	KV366	325-385 nm (control)	
2	KV337	EXG glass (control)	
3	KV375	325-385 nm	
4	KV364	EXG glass	
5	KV334	400 nm long pass	
6	KV365	240-395 nm	
7	KV325	275-375 nm	

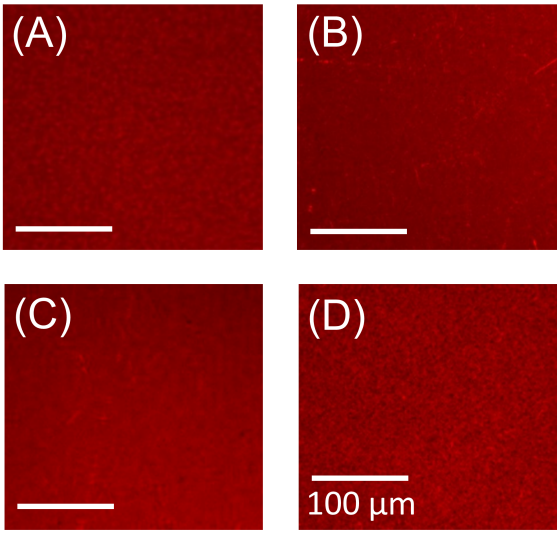


Figure 4.3: Confocal fluorescence microscopy. *Photoluminescence collected between 750 and 800 nm represented as red for (A) glass control (sample 2), (B) glass flight (sample 4), (C) 325-385 nm control (sample 1), (D) 325-385 nm flight (sample 3). 100 µm scale bar for all images. High spatial uniformity of samples made meaningful dark area quantization (as in Fig. 3.7) infeasible.*

resolution. In order to properly record the optical behavior of the MISSE-16 samples, high-resolution PL maps were taken of each sample in a 1 mm^2 grid. The emitted light from each sample passed through a beamsplitter to be analyzed both spectrally and temporally. From these two methods we fully described the PL intensity, energy, and full width at half maximum (FWHM) of the Gaussian signal, as well as the charge recombination lifetime of the perovskite. These four parameters are presented as box plots for each sample in Fig. 4.4. Unlike the clear energy and lifetime shifts of the MISSE-13 flight sample in Fig. 3.8, all seven MISSE-16 devices are optically similar. Energetically, all samples emit between 1.613 and 1.619 eV. A range of 6 meV is not significant for these devices and does not indicate degradation from flight or PbI_2 formation within the crystal lattice. Post flight, the average energy of the EXG glass flight sample was only 1 meV higher than its control, while the 325-385 nm flight sample energy was 1.8 meV higher than its control. Thus, the MISSE-16 flight samples were not found to experience any degradation leading to bandgap shift such as significant PbI_2 formation or lattice strain seen in the MISSE-13 flight sample.

The lack of strain, vital in understanding the response of the MISSE-13 flight sample to the LEO environment, has several possible explanations. First is the shorter flight duration. The MISSE-16 samples orbited the Earth for 6 months, while the MISSE-13 sample orbited for 10 months. The effect of this difference in total thermal

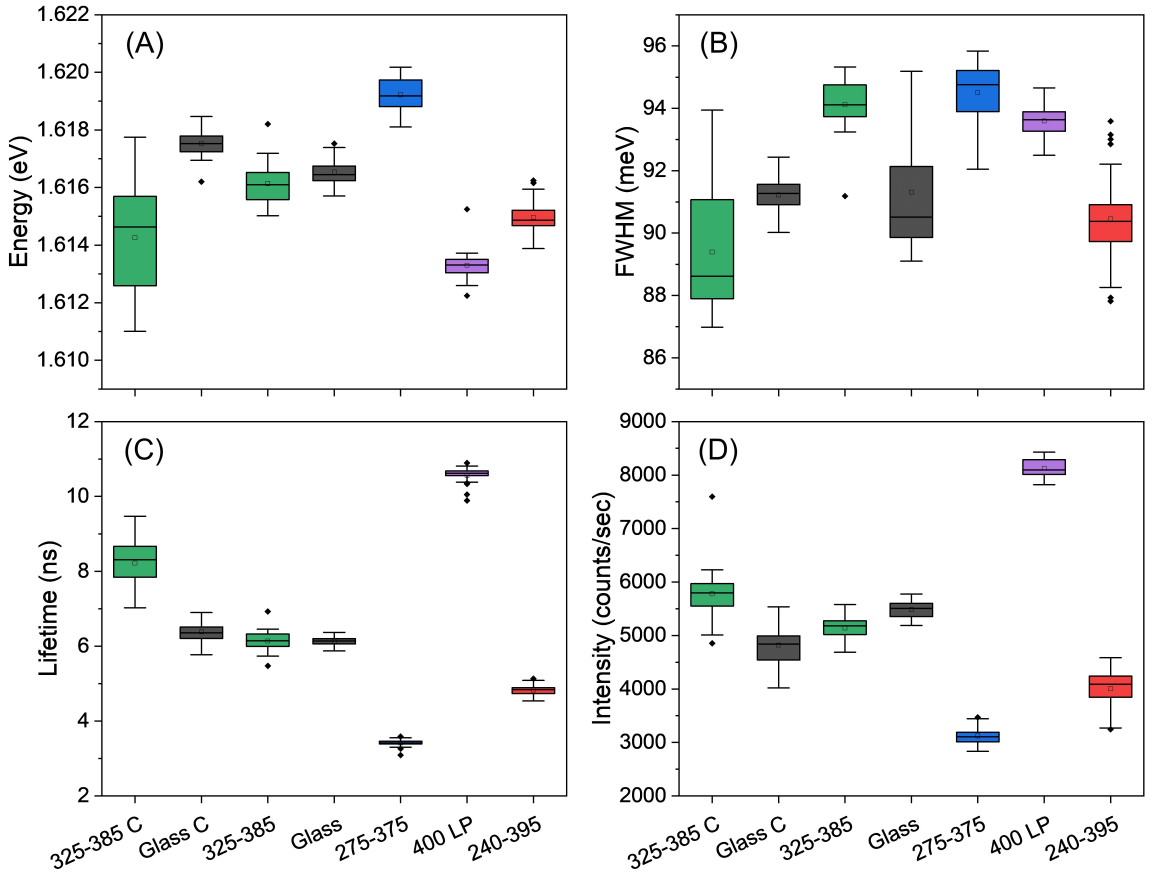


Figure 4.4: Spectral and time-resolved PL metrics. *Boxplots for all control and flight samples provided as a function of (A) energy, (B) FWHM, (C) recombination lifetime, and (D) PL intensity. Each box is composed of 25 data points taken in a 1 mm2 grid across each sample. The small range of (A) and (B) denote little chemical or optical change post-flight. Lifetime (C) and intensity (D) correlation is expected, as shorter lifetimes are likely to be caused by non-radiative recombination and, thus, lower PL counts.*

cycles, AM0 exposure, and high-energy radiation impacts is not well understood in MHP devices. Many stressors which are damaging to perovskites take effect after reaching a threshold within the device. This topic is explored further in Chapter 5 with the optical and chemical breakdown of bare MHP films from increasing proton fluence. With 4 additional months of space exposure, it is possible the MISSE-13 flight sample reached a damaging strain cycle threshold which was not experienced by the MISSE-16 samples. A second possibility for the greater PL uniformity between MISSE-16 samples is the lack of the SiO_2 layer present in the MISSE-13 flight

and control A samples. As described in Chapter 3, the MISSE-13 perovskite film is believed to have been constrained between the SiO_2 layer and borosilicate glass substrate. The rigidity and lack of thermal expansion in these materials produced both tensile and compressive strains within the MHP film, causing its PL characteristics to shift. Without the vapor-deposited SiO_2, the MHP layers of all MISSE-16 samples were instead deposited between their glass substrates and DC93-500 encapsulating epoxy. The epoxy is unlikely to have constrained the MHP in the same way the SiO_2 had previously, as it is a much softer material than the SiO_2. Thus, the MISSE-16 flight samples should not have been as thermally constrained as the MISSE-13 flight sample, yielding the smaller energetic shifts seen in Fig. 4.4A. Third and finally, the MISSE-16 devices are of higher quality than those of MISSE-13, possibly resulting in fewer MHP defects overall. The fabrication facilities at NREL yielded greater uniformity in the MISSE-16 samples than those of MISSE-13, seen in the visual, confocal, and PL data of each. High substrate coverage and low PL variation are indicative of high-quality, defect tolerant MHP layers. As such, the MISSE-16 samples are expected to outperform the more prototypical MISSE-13 devices.

Along with emission energy, the MISSE-16 samples exhibited high uniformity in their FWHM. The range of average linewidth for MISSE-16 devices was only 5.1 meV at room temperature, as seen in Fig. 4.4B. The similar Gaussian width between samples notes the consistency of fabrication and resiliency of devices to the LEO environment. No flight samples returned to Earth with significant increase in FWHM, reflecting the lack of phonon-producing defects in the MHP films. Fig. 4.4C and D provide the charge recombination lifetime and PL intensity respectively of all MISSE-16 samples. These data overall support the case made in the previous two plots of little lasting degradation from the mission. More interesting is the correlation between the two variables. In both Fig. 4.4C and D, the 275-375 nm device has the lowest values, while the 400 nm long pass device has the highest. This correlation is expected physically, as the probability of trap-assisted non-radiative recombination is proportional to the amount of time a charge is excited. Thus, the MHPs with short lifetimes are expected to have lower overall PL emission and those with longer lifetimes should be brighter. This is observed across samples, reducing the possibility of unforeseen variables contributing to the behavior of the MISSE-16 devices.

4.3.3 UV Photostability

Once post-flight PL and confocal characterization was completed, all MISSE-16 samples were subjected to 5 hours UV light exposure to determine photostability. To achieve this, samples were illuminated through the substrate with a 409 nm laser and through the top glass with a 360 nm UV lamp. Spectrally resolved PL was captured every 10 seconds for 5 hours to track changes in the energy, linewidth, and emission amplitude. These tests were performed at the University of California, Merced by

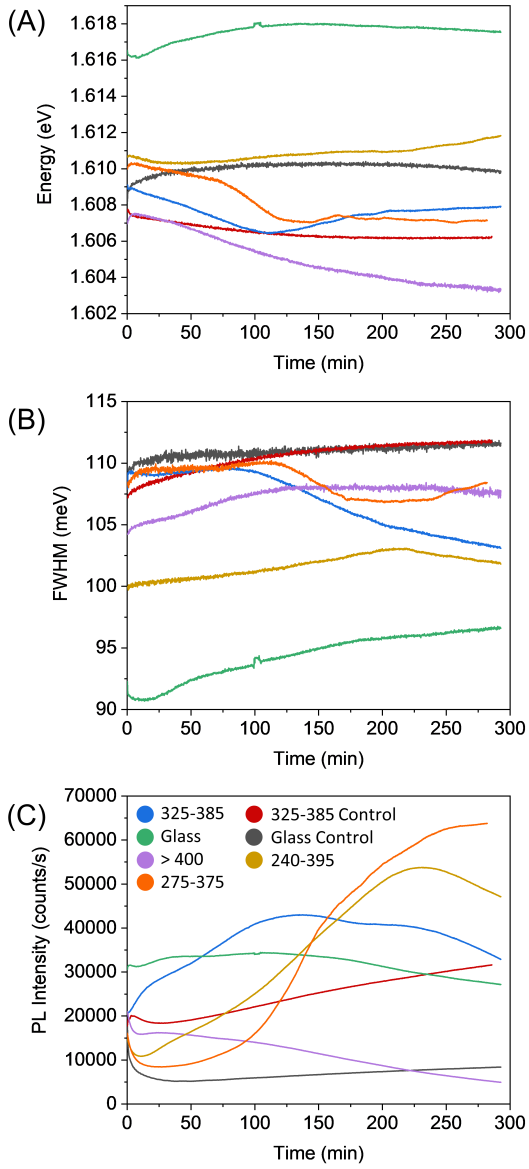


Figure 4.5: Device stability under UV light soaking. *Spectrally integrated (A) energy, (B) FWHM, and (C) integrated PL intensity of all seven MISSE-16 samples recorded every 10 seconds for 5 hours of continuous 360 nm illumination.*

Jorge Arteaga in December 2023. There are few obvious trends between samples in Fig. 4.5. Unlike the clear signs of degradation during MISSE-13 light soaking (Fig. 3.10), the MISSE-16 control and flight samples show no signs of detrimental energy or linewidth shift. Sample 5, utilizing a 400 nm long pass filter, experienced the greatest energy change from 1.608 to 1.603 eV. This redshift of only 5 meV falls within the

range of energies measured across a given sample as seen in Fig. 4.4A. The EXG glass and 325-385 flight samples behave much like their respective controls under UV illumination. While all samples begin the test with slightly different energies, the former initially blueshift then slowly redshift, while the latter primarily decrease in energy over the 5 hours. Most samples experienced a slow increase or decrease in their energies over the 5 hours UV exposure, ultimately red or blue shifting approximately 2 meV. As with previously discussed confocal and PL data, these results demonstrate the stability of both the MISSE-16 flight and control samples. As with bandgap energy, the greatest FWHM variation across any sample is only 5 meV. This change is seen in Fig. 4.5B among both the EXG glass and 325-385 nm flight samples, though the former linewidth broadens and the latter narrows. This change is less than that measured across each sample in Fig. 4.4B, again suggesting insignificant changes during UV light soaking. The integrated PL intensity from each sample is depicted in Fig. 4.5C. Here, both control samples initially undergo a small decrease in PL, then slowly brighten for the remainder of the 5 hours. This response is very similar to that of the MISSE-13 flight sample and control A in Fig. 3.10A, suggesting a slight improvement in the MISSE-16 controls during UV exposure. Slow photobrightening is not recorded in any of the MISSE-16 flight samples, though the 240-395 and 275-375 nm samples significantly brighten during the test. The remaining three samples mostly darken over the 5 hours, though some PL intensity increase is observed as well. Overall, the magnitude of PL signal is not very useful in determining stability in this case. Energy and FWHM are more appropriate and show better agreement with their corresponding PL maps in Fig. 4.4. Though lacking the clear trends of the MISSE-13 AM1.5 light soaking tests, this 5 hour UV exposure induced very little change on the MISSE-16 samples, demonstrating their optical and chemical stability.

4.4 Conclusion

Surpassing the success of the MISSE-13 flight sample, the 5 MHP thin films flown aboard the MISSE-16 mission further demonstrate the resiliency of perovskites in LEO. Samples exposed to specific bands of UV light in the AM0 solar spectrum did not show varying signs of degradation as expected but returned to Earth chemically and optically stable. The few meV difference in bandgap and FHWM between samples is well within batch variation during fabrication. The small number of bubbles within the DC93-500 encapsulant observed in samples 2 and 5 do not appear to have damaged their respective MHP layers. Even localized PL intensity decrease as in the MISSE-13 flight sample (Fig. 3.4) is not observed in these areas, indicative of the dry gas within the bubbles and high-quality perovskite material. As discussed in section 4.3.2, the lack of residual strain in the MHP of flight samples is surprising, though there are several possible explanations. Absence of SiO_2 layer, key to constraining MISSE-13 flight sample, is most likely. The higher grain density and PL uniformity

of MISSE-16 samples may also have made them more defect-resistant and able to relax across many thermal cycles. Finally, the MISSE-16 devices were exposed to the LEO environment for 6 months compared to the 10 months of the MISSE-13 flight sample. The additional 2,000 orbits in 4 months may well have exceeded a damage threshold needed to disrupt the MISSE-13 flight sample until it was relaxed after 15 hours AM1.5 light soaking. Future studies of perovskite devices in LEO are needed to fully understand the role of this intense thermal cycling.

To better understand the effects of AM0 UV light on MHP films and complement the results of MISSE-13, the five flight samples detailed herein were each fitted with a different top glass material. Across four optical filters and one high-transmission glass, all regions of the AM0 UV and visible spectrum were passed to the absorber layer. No significant change was measured between samples with spectral or time-resolved PL, nor with optical or confocal microscopy. These data are encouraging for future MHP devices used in space and provide the first test of *in situ* UV exposure on perovskite material in LEO. While the effects of thermal cycling and UV light on MHP films have been thoroughly explored, the top glass materials used for MISSE-13 and 16 were too thick to allow the majority of LEO protons to reach the MHP layer. In order to understand perovskite degradation from space-relevant particle radiation, 12 MHP samples were exposed to 6 proton fluences and 2 neutron fluences in the laboratory. The following chapter explores the effect of these irradiations on bare perovskite films and further investigates the robustness of MHPs to the stressors of LEO.

Chapter 5

Proton and Neutron Irradiation of Unencapsulated MHPs

Most material presented in this chapter has been submitted for publication in *Joule*.

While the metal halide perovskite (MHP) samples of MISSE-13 and 16 proved robust in LEO, their thick top glass blocked all particle radiation below 14 MeV (Fig. 3.13). The 1 mm thick cover glass was appropriate for these prototype devices, but will become significantly thinner as lightweight, commercial MHPs are developed for space use. To better understand MHP degradation by space-relevant particle radiation, this chapter investigates the effect of 4.5 MeV neutrons and 20 keV protons (p^+) with fluences between 5x10^{10} and 1x10^{16} p^+/cm^2 on unencapsulated MHP thin films. Full cell measurements make it difficult to pinpoint whether changes originate in the MHP layer itself or in other cell components. Consequently, this study isolated the intrinsic radiation tolerance of unencapsulated methylammonium lead iodide/chloride ($CH_3NH_3PbI_{3-x}Cl_x$, or MAPI-Cl) films by focusing characterization solely on the MHP light-absorbing layer itself. Using spatially resolved photoluminescence spectroscopy and confocal microscopy with no other interfaces present, the fundamental radiation damage and defect behavior were revealed through optical changes to the film. Key findings include PL intensity decreased with increasing proton fluence, indicating defect formation led to 30% more film darkening above 1x10^{13} cm^{-2} fluences. Additionally, all proton-irradiated films exhibited continuous blue-shifting of energy bandgap, and charge recombination lifetimes decreased with higher proton fluences. These optical changes in the absorber layer precede performance declines measured by standard current-voltage tests on complete devices. Therefore, they have potential as early indicators of radiation tolerance in MHP solar cells.

5.1 Experimental Design

Prior radiation studies have shown promising resilience of MHP solar cell devices under proton irradiation, with proton energies generally ranging from 150 keV – 10 MeV to simulate the LEO environment [90–92]. In some cases, protons with energies up to 68 MeV have been used to penetrate the device stack and damage the MHP [51, 93, 94]. These tests typically showed no irreversible radiation-induced damage, as higher energy protons transfer little energy to the thin MHP layers and even demonstrate defect healing through ionization [95]. A more appropriate range is 0.05 – 0.15 MeV, where protons stop inside the thin absorber layer and vacancy and interstitial defect formation has been observed [49, 96]. Nearly all prior research utilized complete device stacks with charge transport layers, electrodes, and often extra encapsulation layers for additional environmental protection [52, 91]. Standard photovoltaic metrics like short circuit current, open circuit voltage, fill factor and power conversion efficiency were used to evaluate radiation resistance. To directly probe the light-absorbing layer's intrinsic radiation tolerance, this study used 600 nm thick MAPI-Cl perovskite films deposited on ITO glass, omitting other device layers. These samples, detailed in Table 5.1, were fabricated at the University of California, Merced between November 2022 and March 2023. All work on this project was completed by the author at the University of California, Merced other than radiation exposure, as detailed below. The MHP precursor solution was purchased pre-formulated from Ossila ("Perovskite Precursor Ink for Air Processing"), containing a 3:1 ratio of CH_3NH_3I and $PbCl_2$ in DMF solvent. Thin films were deposited onto ITO coated glass substrates by spin-coating 50 μL of the ink at 3000 rpm for 30 seconds, followed by annealing on a hotplate at 90 °C for 35 minutes. X-ray photoelectron spectroscopy analysis determined the final iodide to chloride ratio 'x' in the $CH_3NH_3PbI_{3-x}Cl_x$ crystal structure to be 0.15. After fabrication, the perovskite film samples were stored in vacuum-sealed bags with desiccant to protect them from moisture and light exposure. Samples were sent to the NASA Langley Research Center for neutron irradiation and the University of North Texas for proton irradiation. As depicted in Table 5.1, samples 1-4 received neutron exposure, 3-8 received two rounds of proton exposure at increasing fluence, and 9-12 received one round of irradiation of the highest proton fluences in the experiment. Samples 9-12 were fabricated as the second batch of MHP samples, needed because the original range of proton fluences did not significantly damage the first batch of samples. SRIM and TRIM simulations indicated 20 keV protons produced the most uniform damage profile within the bare 600 nm films. These ion trajectories and corresponding collision simulations are presented in Fig. 5.1 for 20 keV and 1 MeV protons. Here, confirmed 20 keV protons stop almost entirely within the MHP layer (Fig. 5.1A), maximizing lattice displacements and vacancies, while 1 MeV protons interact minimally (Fig. 5.1C). Fig. 5.1B and D confirm that low energy protons maximize vacancies and lattice displacements

Table 5.1: ***Irradiated samples included in study.*** *Unencapsulated $CH_3NH_3PbI_{3-x}Cl_x$ on ITO glass. A non-irradiated control sample was also fabricated alongside each batch (samples 1-8 and 9-12). . Samples 1-4 exposed to fast (4.5 MeV) and thermal (<0.05 eV) neutrons. "Low n^0" total dose of 2.76x10⁴ mrem, while "high n^0" experienced 5.52x10⁴ mrem. These doses are equivalent to 1 and 2 years on the lunar surface, respectively. Beam flux for each proton fluence described in methods.*

Sample #	Irradiation (cm^{-2})		
	First	***Second***	***Third***
1	low n^0		
2	high n^0		
3	low n^0	5×10^{10} p^+	1×10^{13} p^+
4	low n^0	1×10^{12} p^+	1×10^{14} p^+
5	5×10^{10} p^+	1×10^{13} p^+	
6	1×10^{12} p^+	1×10^{14} p^+	
7	5×10^{10} p^+	1×10^{13} p^+	
8	1×10^{12} p^+	1×10^{14} p^+	
9	1×10^{15} p^+		
10	1×10^{16} p^+		
11	1×10^{15} p^+		
12	1×10^{16} p^+		

in MHPs, while high energy protons produce far fewer collisions within the film. To maximize damage to the MHP layer, 20 keV proton beams were generated from a TiH cathode with the Source of Negative Ion by Cesium Sputtering method [50, 97]. Using Space Environment Information System (SPENVIS) simulations, the annual LEO 20 keV proton fluence was estimated between 10^{11} and 10^{12} p^+/cm^{-2} [98]. Based on this range and fluences used in MHP irradiation tests in literature, we exposed samples to six proton fluences between $5x10^{10}$ and $1x10^{16}$ p^+/cm^2. Samples 1-4 were exposed to 4.5 MeV neutrons at doses equivalent to 1 and 2 years on the lunar surface. After initial irradiation, select samples underwent further rounds of proton irradiation to capture non-linear damage mechanisms, with full characterization between exposures. Control samples were fabricated prior to each set of radiation rounds to provide comparison.

5.2 Results and Discussion

Scanning electron microscopy (SEM) images in Fig. 5.2 show no obvious differences in film morphology between the non-irradiated control (Fig. 5.2A) and samples ex-

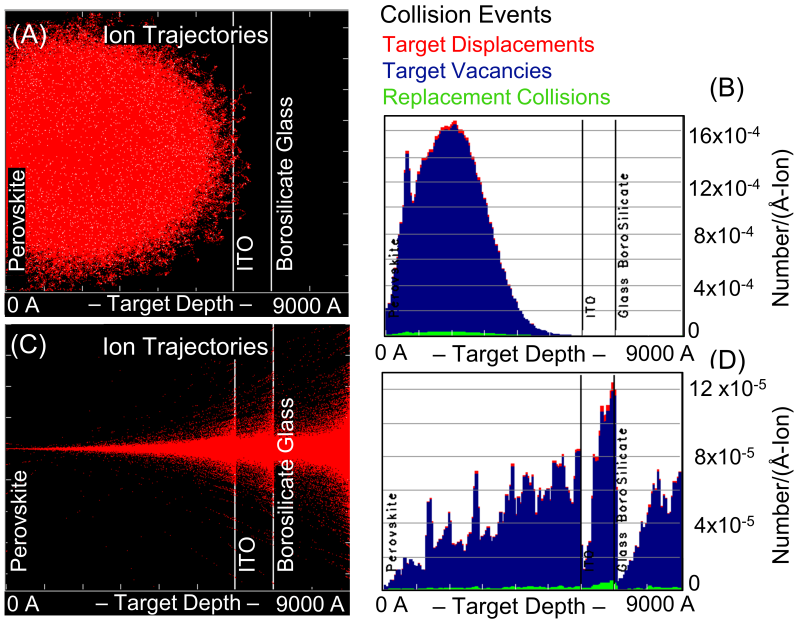


Figure 5.1: Determining proton beam energy. *SRIM/TRIM simulations depicting (A) 20 keV and (C) 1 MeV proton trajectories within irradiated samples. Energy loss of low (B) and high (D) energy protons due to movement through crystal lattice and recoils.*

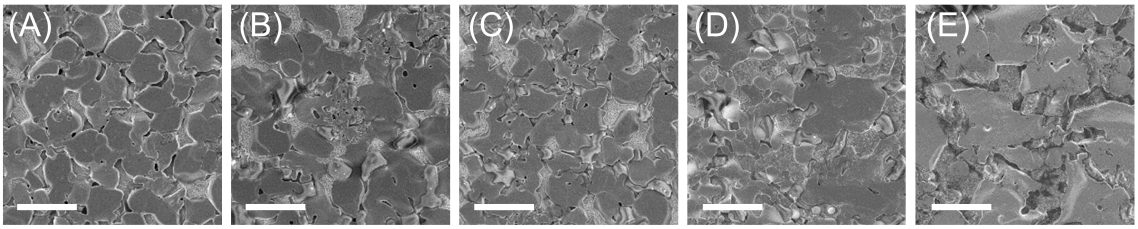


Figure 5.2: Scanning electron microscope images. *(A) Control, after proton exposure for (B) 10^{13} p/cm^2, (C) 10^{14} protons/cm^2, (D) 10^{15} protons/cm^2, (E) 10^{16} protons/cm^2. Control sample, 5, 8, 11, and 12, respectively.*

posed to proton fluences from 10^{13} – 10^{16} p$^+$/cm^2 (Fig. 5.2B-E), confirming previous observations. The somewhat larger domains in Fig. 5.2D, E are seen in all films of the second batch (samples 9-12) and are not due to irradiation effects. However, SEM is not ideal for characterization in this case as it does not allow for direct pre- and post-irradiation comparisons on the same samples. The electron beam can reach high power during observation, leading to charging on the MHP surface. Confocal

microscopy photoluminescence (PL) mapping in Fig. 5.3 allows comparing films before and after proton irradiation. Fig. 5.3A-C show sample 7 before exposure, after 10^{10} p^+/cm^2, and after 10^{13} p^+/cm^2 fluences, with little visible change. However, Figs. 5.3D-F for sample 4 reveal distinct darkening after 10^{14} p^+/cm^2, indicating defect-induced non-radiative recombination. Quantitative analysis across multiple images (Fig. 5.3G) revealed samples over 10^{13} p^+/cm^2 fluences exhibited comparable areas of PL signal loss, suggesting a threshold for radiation-induced trap state density increases enabling non-radiative recombination pathways. Samples irradiated below this 10^{14} p^+/cm^2 limit, including the non-irradiated control and those tested across several orders of magnitude, all produced $< 5\%$ change in darkened PL area. The analysis of samples 1 and 2 after neutron radiation exposure showed no discernible changes in their PL response (Fig. 5.4), indicating a high tolerance to neutron damage.

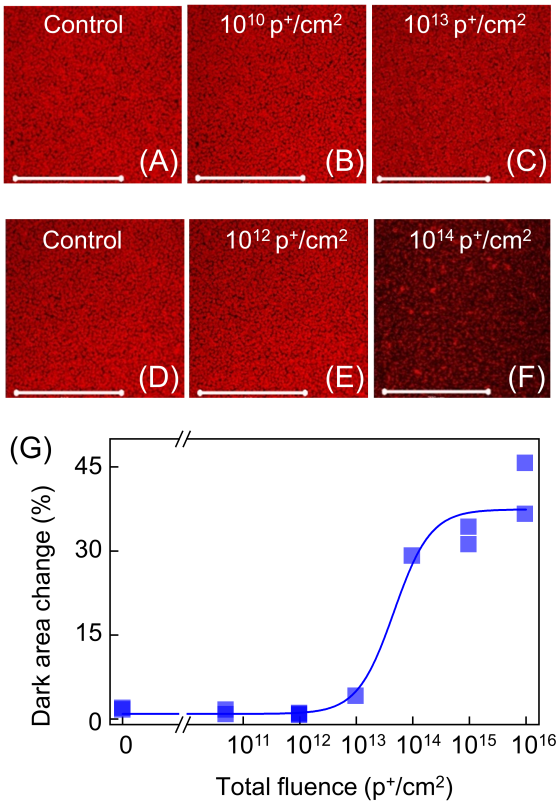


Figure 5.3: Photodarkening with increasing proton fluence. *Confocal fluorescence images of sample 7 (A) before irradiation, (B) after the first irradiation and (C) after the second irradiation. (D – F) Same protocol for sample 4. Scale bars: 200 μm. (G) Change in percent non-emissive area post- irradiation for all proton fluences tested.*

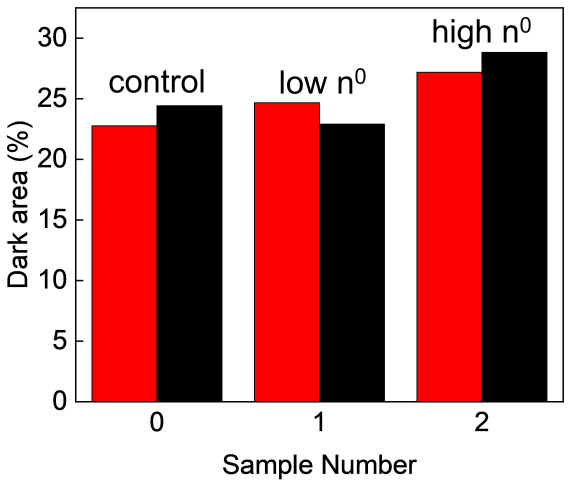


Figure 5.4: Confocal PL dark area for neutron-irradiated samples. *ImageJ analysis reveals non-emissive area between 22.7 and 28.8% across neutron samples of two fluences, as well as their control. This is range is negligible and expresses only the variation in perovskite grain density between samples.*

Following confocal investigation, high-resolution (2 µm spot size) scanning PL spectroscopy (Fig. 5.5) was performed on all samples to understand their spectral characteristics. Spatial maps of each sample across 1 mm^2 areas revealed fluences $> 10^{13}$ p^+/cm^2 caused linear blue-shifts in bandgap energy (Fig. 5.5A) and rapidly decreasing charge carrier lifetimes (Fig. 5.5B) with each successive order of magnitude proton exposure. Samples receiving 10^{12} p^+/cm^2 experienced a negligible energy and FWHM shift (Fig. 5.5C) in comparison to the control sample, though the lifetime reduction is similar to those of higher fluences. This reduction in lifetime for all samples is expected, as protons of 20 keV energy generate substantial crystalline lattice defects before coming to rest inside the MHP layer [49, 54]. These proton collisions displace atoms, creating vacancies and interstitial defects within the lattice. As the exposure increases, the density of these defects escalates, enabling more non-radiative recombination pathways through the resulting mid-bandgap trap states. Optically, this defect-assisted non-radiative recombination also manifests as decreasing PL intensity, seen in the confocal images of Fig. 5.3A-F. For MAPI-Cl and other organic-inorganic perovskites, increases in bandgap energy typically indicate chemical degradation occurring through the formation of lead halide domains that emit at higher energies. Therefore, the blue-shifting trend with increasing fluence in Fig. 5.5A suggests escalating compositional dissociation is taking place within the films due to the radiation exposure. MHPs are susceptible to continuous light exposure, which spontaneously generates defects like halide vacancies and interstitials [99, 100]. This enhances ion migration and increases defect density under prolonged illumination. However, mod-

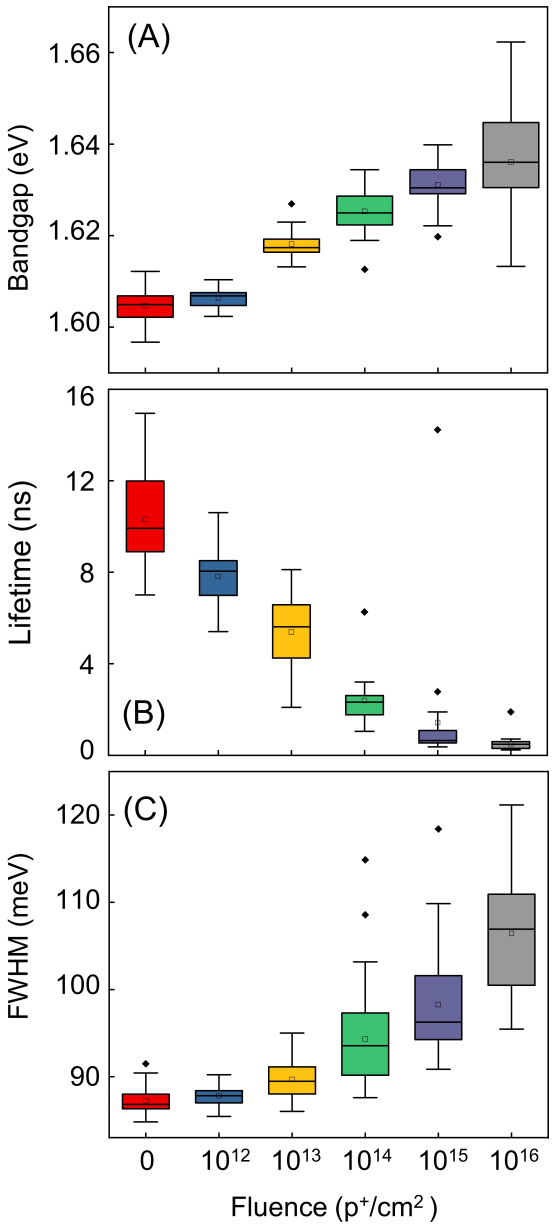


Figure 5.5: Bandgap and lifetimes with increasing proton fluence. *Box plots depicting (A) band gap, (B) charge recombination lifetime, and (C) spectral full width half maximum averaged over all samples for each radiation fluence.*

erate visible light intensity can sometimes reverse this damage and anneal away defects by activating the innate ion migration transport properties inherent to MHPs [101, 102]. Specifically, previous studies have observed CH_3NH_3 cations and halide anions filling vacancies, repairing anti-site defects, and reconstructing the crystalline

structure [92]. The response to 15 hours of 'light soaking' (LS) under AM1.5 illumination for the proton-irradiated samples is compared to a non-irradiated control film in Fig. 5.6. Fig. 5.6A and B show the evolution of the energy bandgap and PL emission intensity over time, respectively. The proton-irradiated perovskite films initially display larger bandgaps than the control, indicating a higher baseline disorder from radiation-induced defects. As expected, the control film exhibits gradual blue-shifting and dimming of the PL emission during visible light exposure. In contrast, the ir-

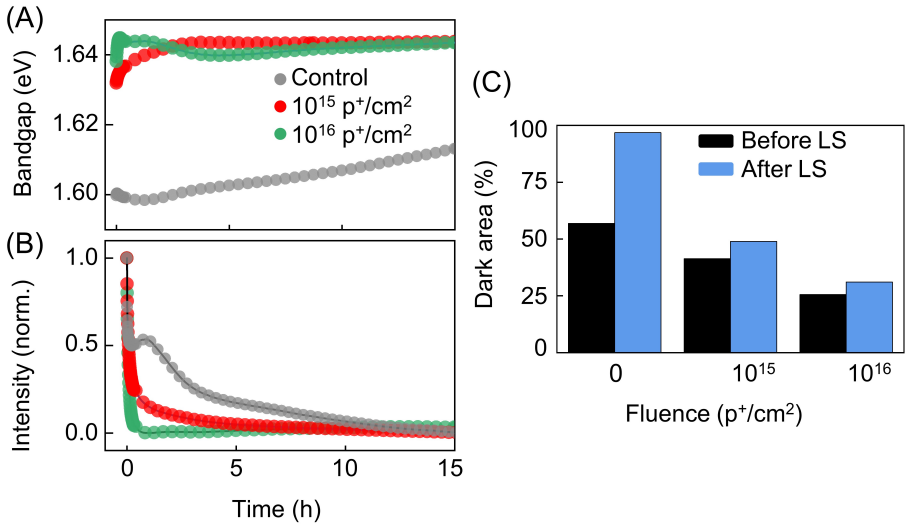


Figure 5.6: AM1.5 light soaking. *(A) Energy, and (B) PL intensity measured over 15 hours of AM1.5 illumination, comparing a control sample with two irradiated with 1015 and 1016 p+/cm2. (C) Percent non-emissive area before and after light-soaking for the same samples.*

radiated samples, with PL peaks already substantially blue-shifted from the control, undergo little further spectral variation. Regarding emission intensity, the irradiated films darken more rapidly than the control initially. However, despite their differing starting points and extents of photodarkening, the spectral metrics of all three films ultimately converge to similar values for both PL peak energy and intensity by the end of the experiment. This unexpected equivalent convergence is surprising given that confocal imaging analysis (Fig. 5.7) and the bar plot in Fig. 5.6C reveal the control exhibits substantially higher photodarkening over the irradiation-disordered samples.

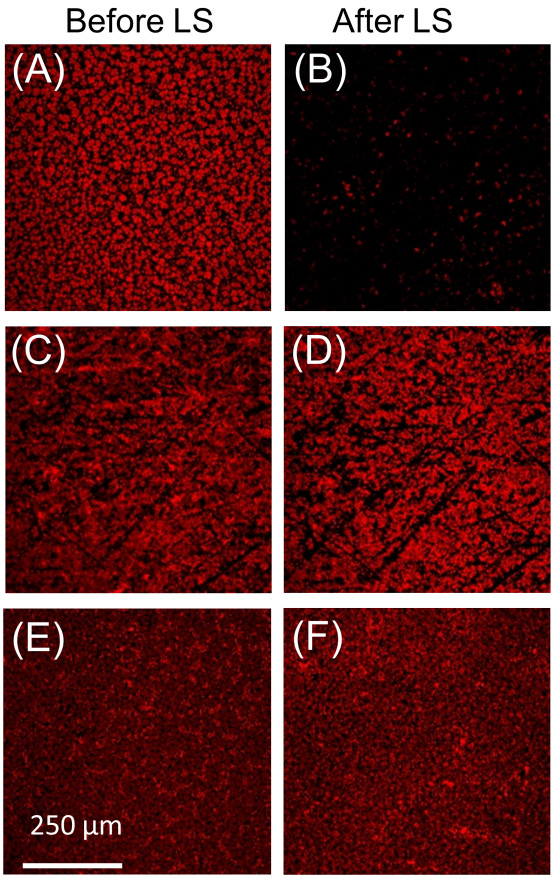


Figure 5.7: Spatial PL change from AM1.5 light soaking. *Confocal fluorescence images before and after 15 hr AM1.5 exposure. Samples exposed to light after receiving proton fluences of zero (A, B), 10^{15} (C, D), and 10^{16} (E, F) protons/cm^2. All sample have the same scale.*

There are no signs of light-induced defect healing in this case, which is often associated with strain relaxation in perovskite films [103]. Without thermal cycling or constraining top layers present, it is unlikely the samples experienced significant internal stress that could facilitate such a healing process as seen in the MISSE-13 flight sample in Chapter 3 [2].

5.3 Conclusion

In summary, this optical characterization of proton-irradiated perovskite thin films provides strong evidence supporting their radiation tolerance and potential for recovery under AM1.5 light soaking conditions. The results demonstrate that proton irradiation of methylammonium lead halide perovskite films generates escalating radiation damage at fluences exceeding 10^{13} p^+/cm^2, quantified through decreasing PL emission intensity. All fluences above this threshold produce comparable levels of non-radiative recombination and darkened fractional film areas. This level of radiation resilience exceeds that of one year in LEO by several orders of magnitude, attesting to the powerful defect tolerance of MHPs. This fluence threshold aligns with the observed linear blue-shifting of bandgaps and reductions in charge carrier lifetimes in the 10^{14} – 10^{16} p^+/cm^2 regime, confirming increasing defect densities that enable non-radiative recombination pathways. The bandgap widening stems from chemical degradation and compositional dissociation within the films. Subsequent extended visible light exposure and light soaking reveals some divergence between the photostability trends of pristine and pre-irradiated films. Notably, these studies confirm that direct spectral characterization techniques are superior to traditional photovoltaic power conversion efficiency (PCE) measurements for accurately revealing the true proton radiation tolerance limits of perovskites. The optical metrics exposed damage onset beginning at 10^{13} p^+/cm^2 fluences, whereas prior work relying on PCE has not detected degradation from space-relevant proton energies until higher fluences [52, 104]. Furthermore, PCE strongly depends on initial device quality, potentially masking incremental damage in poorly performing films [49]. Full device encapsulation and interfacial layers also convolute localization of degradation mechanisms. Thus, traditional electrical tests fail to sensitively convey the fundamental material's intrinsic radiation tolerance. In contrast, direct optical probing of the bare absorber layer alone provides straightforward insights on defect generation and detection of lower fluence damage onsets undetectable electrically. Eliminating confounding factors from other layers or low baseline PCE enables clear interpretation of proton bombardment impacts through the sensitive PL, bandgap, and lifetime metrics. Optical spectroscopy on isolated perovskite films thereby constitutes the most revealing approach for accurately assessing proton radiation degradation in metal halide perovskites.

Chapter 6

15^{th} Materials International Space Station Experiment

The material presented in this chapter is currently in preparation for publication.

In the previous chapters, we have examined the effects of low Earth orbit (LEO) on six metal halide perovskite (MHP) thin films, as well as determined the proton fluence needed to damage these MHPs. The 13^{th} Materials International Space Station Experiment (MISSE) mission revealed the resiliency of MHPs to LEO stressors and the impact of thermal cycling on a constrained perovskite film. The five flight samples of MISSE-16 did not experience additional defects from increased ultraviolet (UV) exposure, instead returning to Earth in better condition than the MISSE-13 flight sample. By systematically subjecting unencapsulated MHP films to increasing proton fluences, we found a breakdown threshold between 10^{13} and 10^{14} protons/cm^2, several orders of magnitude greater than would be experienced in a ten-year space mission [105, 106]. Having explored thermal cycling, ultraviolet (UV) light exposure, and several other LEO stressors on isolated films, we finally turn in this chapter to full perovskite solar cells (PSCs). Aboard the MISSE-15 mission, our team flew eight PSCs in zenith (sun-facing) orientation for eight months. Two devices each of the four architectures were included. Half the cells were of n-i-p structure, with the electron transport layer deposited before the perovskite absorber, while the other half were p-i-n. The n-i-p devices included two all-inorganic $CsPbI_2Br$ cells and two formamidinium (FA)-rich triple cation ($Cs_{0.04}MA_{0.05}FA_{0.91}Pb(I_{0.95}Br_{0.05})_3$) cells. The p-i-n devices included two methylammonium lead iodide (MAPI, $CH_3NH_3PbI_3$) cells and two triple cation ($Cs_x(MA_{0.17}FA_{0.83})_{(100-x)}Pb(I_{0.83}Br_{0.17})_3$) cells. Perhaps the most significant difference between these samples was the use of Ag in p-i-n devices and Al in n-i-p cells as electrical contacts. Ultimately, the MHP layer of all devices other than the inorganic $CsPbI_2Br$ would remain emissive and stable post flight in the regions between the top electrical contacts. Unfortunately, the Al and Ag layers degraded

into the PSC stacks via ion migration, causing yellowing of the perovskite and loss of electrical response. This chapter will discuss microscopic and spectroscopic data which was vital to understanding the behavior of all eight samples in LEO. Emphasis will be placed on microscopy and the complementary nature of fluorescent and optical images in deciphering the degraded regions of these samples.

6.1 Mission Timeline

Eight MHP flight samples and seven MHP control samples were fabricated at the National Renewable Energy Laboratory (NREL) by Kaitlyn VanSant in April 2021 for the MISSE-15 mission. Samples 1-8 as described in Table 6.1 traveled to Alpha Space Test and Research Alliance, LLC in Houston, TX for environmental testing including a high vacuum bakeout at 60 °C for 25 hr and 3-axis vibration at 4.5 G_{rms} (where 1 G_{rms} = 9.8 m/s^2). They were exposed to ambient conditions in Florida

Table 6.1: ***Details for all MISSE-15 flight and control samples.*** *Samples 1-8 flew aboard the ISS, while 9-15 remained on Earth as control samples. Each of the four device types will also be referenced to encompass all devices of a given perovskite composition.*

Sample #	NASA #	Structure	Type	Perovskite Composition	Cell Architecture
1	PP1 KV2	p-i-n	MAPI	$CH_3NH_3PbI_3$	Glass/ITO/PTAA/Perovskite/C60/BCP/Ag
2	PP2 KV51	p-i-n	MAPI	$CH_3NH_3PbI_3$	Glass/ITO/PTAA/Perovskite/C60/BCP/Ag
3	PP3 AK1205	n-i-p	3cat	$Cs_x(MA_{0.17}FA_{0.83})_{(100-x)}Pb(I_{0.83}Br_{0.17})_3$	Glass/ITO/SnO_x NP/Perovskite/PTAA/MoO_x/Al
4	PP4 AK1206	n-i-p	3cat	$Cs_x(MA_{0.17}FA_{0.83})_{(100-x)}Pb(I_{0.83}Br_{0.17})_3$	Glass/ITO/SnO_x NP/Perovskite/PTAA/MoO_x/Al
5	PP5 SH1124	p-i-n	FA-rich 3cat	$Cs_{0.04}MA_{0.05}FA_{0.91}Pb(I_{0.95}Br_{0.05})_3$	Glass/ITO/NiO_x/Perovskite/C60/BCP/Ag
6	PP6 SH1127	p-i-n	FA-rich 3cat	$Cs_{0.04}MA_{0.05}FA_{0.91}Pb(I_{0.95}Br_{0.05})_3$	Glass/ITO/NiO_x/Perovskite/C60/BCP/Ag
7	PP7 AK1207	n-i-p	$CsPbI_2Br$	$CsPbI_2Br$	Glass/ITO/SnO_x NP/Perovskite/PTAA/MoO_x/Al
8	PP8 AK1209	n-i-p	$CsPbI_2Br$	$CsPbI_2Br$	Glass/ITO/SnO_x NP/Perovskite/PTAA/MoO_x/Al
9	C1 KV20	MAPI controls for samples 1 and 2			
10	C2 KV66				
11	C3KV78				
12	C4 AK1292	$CsPbI_2Br$ control for samples 7 and 8			
13	C5 AK1232	Triple cation control for samples 3 and 4			
14	C6 SH1120	Formamidinium-rich triple cation controls for samples 5 and 6			
15	C7 SH1128				

for ≈ 4 months during payload integration. The flight samples were loaded onto a SpaceX Falcon 9 rocket and launched on the 23^{rd} Commercial Resupply Service mission (CRS-23) on August 29, 2021. Aboard the ISS, the samples were deployed on the MISSE-Flight Facility platform in zenith (sun-facing) orientation between November 20, 2021 and July 31, 2022. The samples were electrically connected to the

platform with a conductive carrier sheet to prevent electrostatic discharge to the ISS. The MISSE-15 mission concluded with the landing of SpaceX CRS-25 on August 20, 2022. The flight samples were returned to NREL on September 29, 2022. Post-flight characterization of all samples began at the University of California on March 15, 2023, two years after fabrication.

6.2 Sample Fabrication Details

Two samples each of the four PSC architectures diagrammed in Fig. 6.1 were flown aboard MISSE-15. This collection of devices was chosen to vary the perovskite absorber, charge transfer layers, and top contacts of the devices. Half of the cells were of traditional n-i-p orientation and utilized Ag top contacts, while the other half were inverted p-i-n devices with Al pixels. Post flight images of the front and back

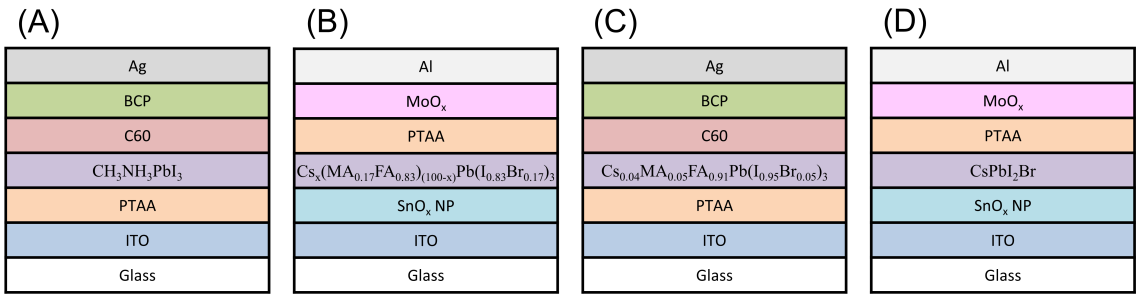


Figure 6.1: MISSE-15 device schematics. *Two devices of each architecture above were flown aboard MISSE-15. (A) p-i-n MAPI cell, (B) n-i-p triple cation cell, (C) p-i-n formamidinium-rich triple cation cell, (D) n-i-p all-inorganic CsPbI2Br cell.*

of all flight samples, as well as back-illuminated images, are provided in Table 6.2. Perhaps the most striking aspects of these images are the yellow metal regions and photobleaching of the $CsPbI_2Br$ devices. These observations along with many others will be investigated in the following sections. Similarly to Table 6.2, front and back images of all control samples taken when the flight samples returned to Earth are collected in Table 6.3. Again the $CsPbI_2Br$ cell has turned translucent, though the metal contacts appear far less damaged than among the flight samples.

Table 6.2: ***MISSE-15 flight samples.*** *Photographs of all flight samples presented from the front, back, and front with back illumination. Regions which appear grey or silver in the front images are intact Al or Ag. Yellow regions in all images are due to degradation. All substrates are 1 mm^2.*

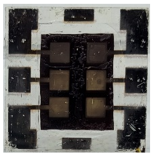
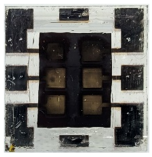
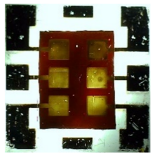
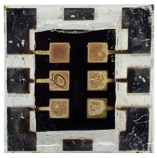
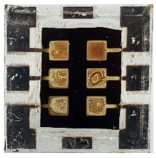
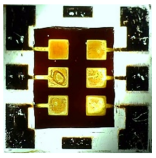
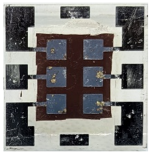
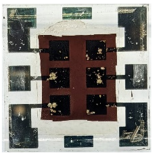
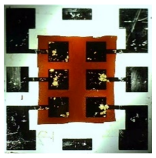
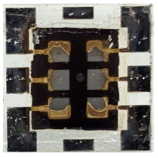
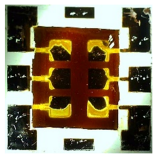
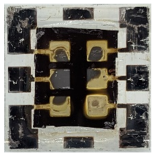
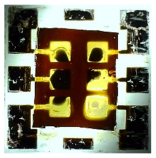
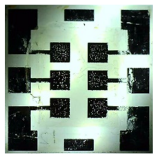
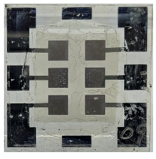
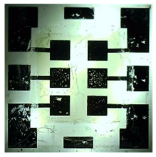
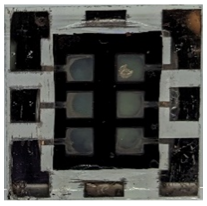
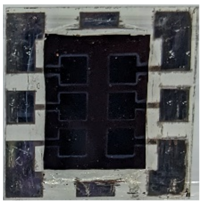
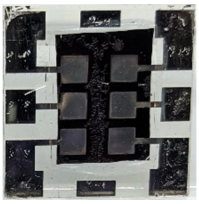
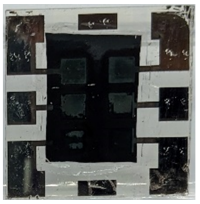
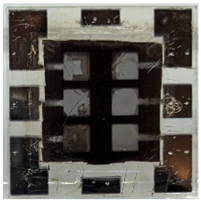
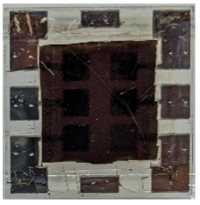
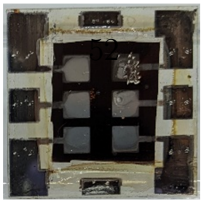
Sample # and Type	Front	Back	Front, back illuminated
1, MAPI			
2, MAPI			
3, 3cat			
4, 3cat			
5, FA-rich 3cat			
6, FA-rich 3cat			
7, $CsPbI_2Br$			
8, $CsPbI_2Br$			

Table 6.3: ***MISSE-15 ground control samples.*** *Photographs of all control samples presented from the front and back. Note the discoloration of many Al and Ag contacts, though not as severe as in the MISSE-15 flight samples. All substrates are 1 mm^2.*

Sample # and Type	Front	Back
9, MAPI		
10, MAPI		
11, MAPI		
12, $CsPbI_2Br$		
13, 3cat		
14, FA-rich 3cat		
15, FA-rich 3cat		

6.3 Results and Discussion

6.3.1 Optical and Fluorescence Microscopy

Apart from the $CsPbI_2Br$ devices, the MHP absorber layer remained dark and emissive for all MISSE-15 flight and control samples in the region between metal top contacts. Unfortunately, both Al and Ag contacts show signs of significant degradation across all flight samples. The ion migration between metal and MHP layers caused varying degrees of damage across samples and within samples. Fig. 6.2 provides pre and post flight images of MAPI (sample 2) and triple cation (sample 3) devices, as well as their current-voltage (I-V) characteristics. While the Ag contacts

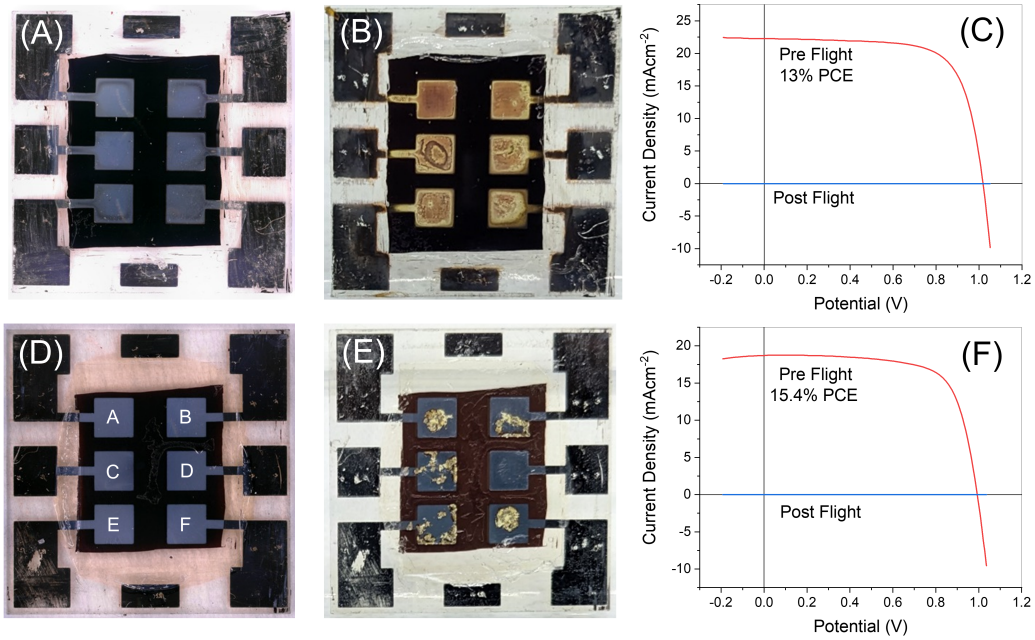


Figure 6.2: Ag and Al contact degradation. *Images of the front of samples 2 (MAPI, A, B), and 3 (triple cation, D, E), pre and post flight. The Ag contacts used in MAPI and FA-rich triple cation samples degraded differently than the Al contacts used in the $CsPbI_2Br$ and triple cation samples. Sub-cells A-F are labeled in (D). This pattern is shared by all samples as viewed from the front (through the top glass). Current-voltage response is plotted for samples 2 (C) and 3 (F). No electrical response was measured for any sample post-flight.*

of Fig. 6.2A show some signs of discoloration around pixel edges pre flight, the Al contacts of Fig. 6.2D appear extremely uniform and reflective. The six pixels of each MISSE-15 sample are labeled A-F as in Fig. 6.2D, viewed from the front side of the device through the cover glass. After 8 months in LEO, samples 2 and 3 returned to

Earth as seen in Fig. 6.2 B and E, respectively. Interestingly, the Ag and Al contacts degraded quite differently during flight. While the Ag of the MAPI and FA-rich triple cation samples turned from grey and reflective to yellow and dull from the edges of the devices, the Al of the triple cation cells exhibited smaller, scattered patches of yellow defects across nearly all pixels in samples 3 and 4. The Al of the flight $CsPbI_2Br$ cells

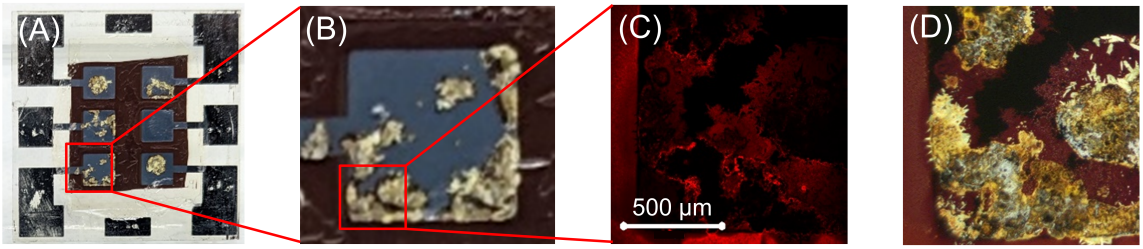


Figure 6.3: Optical and confocal analysis of degraded Al region. *(A) Front image of triple cation sample 3. (B) Magnified image of bottom-left Al contact. (C) 4x magnification confocal fluorescence image of this region. Ideally, all PL signal should be blocked by the Al square and appear black in this image. (D) 4x magnification transmission optical microscope image. The characteristic dark red of the MHP layer matches one-to-one with the fluorescent regions in (C).*

returned with dozens of small pinholes spread evenly across most pixels. It is more difficult to determine the behavior of $CsPbI_2Br$ device layers due to the total photo-bleaching of the absorber layer in both flight samples, and almost total bleaching of the control samples (Table 6.3). Fig. 6.2C and F provide I-V curves of samples 2 and 3, respectively. As expected, the triple cation device efficiency of 15.4% is greater than the MAPI device at 13% pre flight. Post flight, neither sample yields current at any tested voltage. This is true of all ground and flight MISSE-15 samples, indicative of electrical failure and possible delamination of contacts from the device. Without electrical connection, this study is limited to optical characterization techniques as in the previous three chapters. Microscopic investigation will focus first on Al defects, then examine Ag devices. Fig. 6.3 presents a series of optical and confocal fluorescent images of triple cation sample 3. Focusing on pixel E in Fig. 6.3B, one can see the Al pad mostly intact, but with several yellow, damaged sections. With an LSM 880 confocal microscope system, a 405 nm laser was used to excite the sample and emitted light was collected between 1.55 – 1.65 eV. Fig. 6.3C magnifies the bottom left corner of pixel E and examines the spatial emission profile of the MHP layer. The red region along the left edge of the image is uniform emission from the MHP which is outside the contact area. This area of perovskite is representative of the MHP layer between pixels of nearly all samples, which will be addressed later in this chapter. The black regions of Fig. 6.3C are those of intact Al. Since the Al is above the absorber layer

as imaged through the top glass, it will block incoming excitation and outgoing PL from the MHP. The yellow regions of Fig. 6.3B map one-to-one with the red regions of Fig. 6.3C, verifying that the Al has moved deeper into the cell, revealing the MHP layer beneath. Fig. 6.3D complements this emission with transmission optical microscopy. Here, rather than the false-colored red band of fluorescence microscopy, visible regions of the sample are directly observed with white light passing through the sample. Most of the red emissive regions in Fig. 6.3C are similarly dark red in Fig. 6.3D. This deep-red color is due to absorption in the MHP layer and lies between the black and yellow/grey regions of Fig. 6.3D. In this image, black regions are areas of intact Al which block the light from below. Black regions of Fig. 6.3C, however, include both the black and yellow/grey regions of Fig. 6.3D. Thus, emissive areas within the Al pixels are found in regions between the intact and degraded metal. A

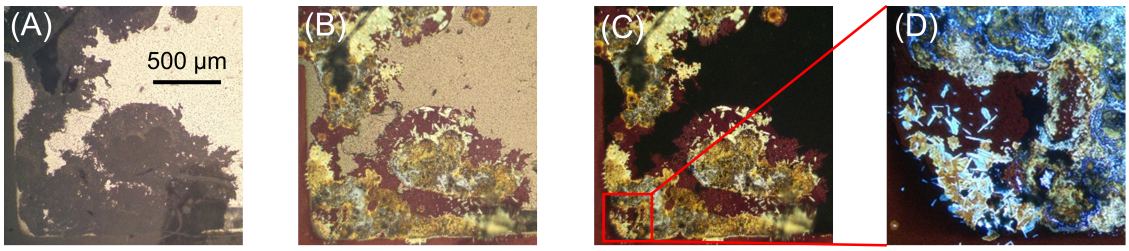


Figure 6.4: Comparing optical microscope images. *(A) 4x magnification optical reflection of degraded Al contact region of triple cation sample 3. (B) Image of both transmitted and reflected light on sample 3. (C) Optical transmission only for the same area. (D) 20x magnification transmission of the corner of the Al contact.*

slightly larger portion of the corner of pixel E is further explored in Fig. 6.4 with three optical lighting conditions. Fig. 6.4A examines this area via reflected light only. This method clearly defines the remaining Al on pixel E, providing better contrast than Fig. 6.3D. Transmitted and reflected light are used together in Fig. 6.4B to easily see both the Al and red MHP regions. Fig. 6.4C is similar to Fig. 6.3D, again using only transmitted light but now covering a larger area. Fig. 6.4D utilizes a 20x objective to further magnify the bottom left corner of this pixel. The most severe damage in this image occurs along top and right edges, while the red MHP is in the center. The left and bottom of the image include white and yellow lines up to 50 µm in length surrounded by red and black. These small spots and lines are likely the beginning of damage in the area, as they are far less dense than the top and right regions of the image. Exactly how the Al is moving into the device stack is not yet fully understood, and the project remains ongoing.

Fig. 6.5 presents another view of sample 3. Fig. 6.5B, magnifying the entirety of

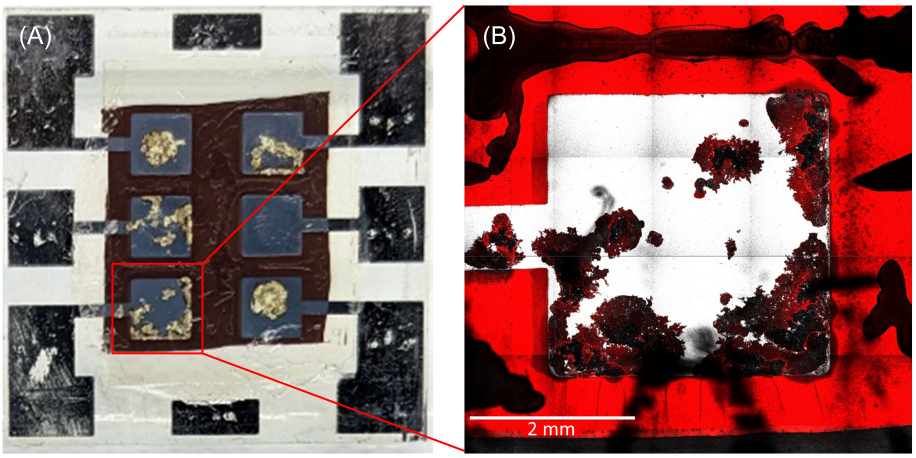


Figure 6.5: Combined confocal fluorescence images. *(A) Front image of triple cation sample 3. (B) combined reflection and PL confocal images. White denotes reflection, red emission, and black no signal. Note the large number of bubbles within the encapsulant around the Al square. The MHP layer is still emissive within the bubbles, though the focus must be changed to account for the difference in refractive index.*

pixel E in Fig. 6.5A, combines reflection and emission confocal images. Here, white areas denote reflection, red emission, and black no signal. Vertical and horizontal lines in the image are caused by stitching together smaller scans and can be ignored. As in Fig. 6.3C, emissive regions within the Al pixel appear primarily between the metal and black areas. This is especially clear near the top right corner of pixel E, where an isolated region is red along its periphery and black in the center. The black region along the bottom of the image is simply the edge of the MHP material, having been removed with a razorblade before subsequent layers were deposited. Other black regions outside the Al are caused by bubbles within the encapsulant. The perovskite within these regions is emissive, as can partially be seen in the top bubble, but the microscope focus must be adjusted to account for the difference in reflective index. A final characteristic of Al decomposition can be seen in Fig. 6.6. Fine cracks in the Al layer were discovered among two pixels of sample 3. Fig. 6.6A and B show these cracks in two areas of pixel D with combined reflection and fluorescence microscopy. MHP emission is visible through the cracks in red. Similarly, Al cracks are seen as red lines in the transmission optical image of Fig. 6.6C. While these cracks are not as abundant as other types of defects highlighted so far, they provide another instance of Al failure among MISSE-15 flight samples. Overall, the Al pixels of triple cation flight samples 3 and 4 have partially degraded into the cell stack and fail to provide electrical connection.

Unlike the small patches of yellow/grey damage among Al pixels, Ag contacts

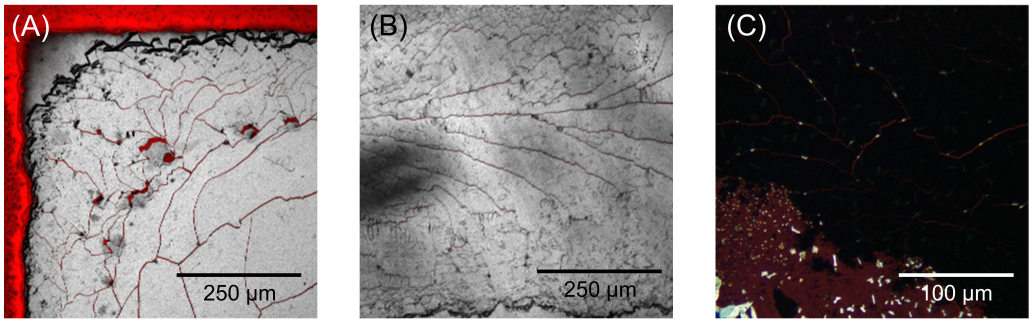


Figure 6.6: Cracks in aluminum electrodes of sample 3. *(A) Reflection and emission confocal image of corner of pixel D. (B) Reflection and emission confocal image of center right pixel D. (C) 10x magnification transmission microscope image of Al pixel C.*

experienced more uniform and severe discoloration from the outside inward. All pixels of MAPI flight samples 1 and 2 have fully turned yellow, and the pixels of FA-rich triple cation samples 5 and 6 have mostly yellowed (Tables 6.2 and 6.3). Additionally, MAPI controls 9-11 and FA-rich triple cation controls 14 and 15 show clear signs of damage, while the Al of triple cation control 13 is almost perfectly intact. The remainder of this section will examine the more destructive Ag contacts among flight and control samples. Fig. 6.7 investigates a region of such degradation in FA-rich triple cation sample 5. Pixel E from Fig. 6.7A is magnified with a transmission optical

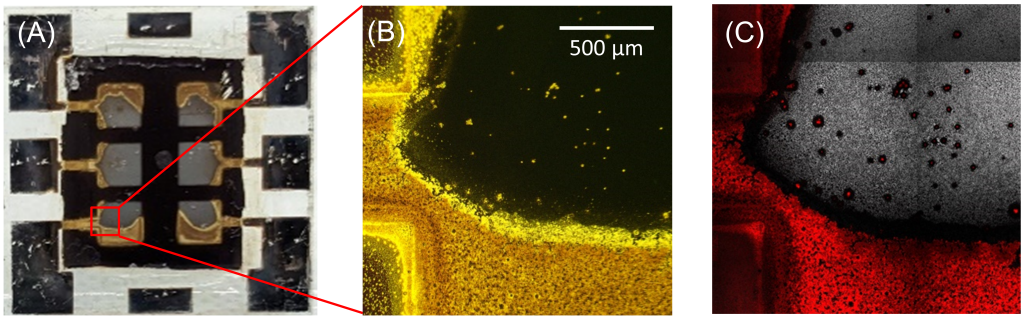


Figure 6.7: Optical and confocal analysis of degraded Ag region. *(A) Front image of FA-rich triple cation sample 5. (B) 4x magnification transmission optical microscope of this region. (C) Combined reflection and PL confocal image of magnified area. Note the more uniform and severe degradation of Ag compared to Al contacts. The faint vertical and horizontal line in C are caused by stitching larger areas together with the confocal microscope.*

microscope in Fig. 6.7B. Here, the intact metal blocks light from below as expected,

but the degraded region appears overwhelmingly yellow. Unlike the dull red in the top and bottom left corners previously seen from MHP films, the intense yellow obfuscates any sign of emission through the degraded Ag. These yellow regions, however, are also emissive as seen in Fig. 6.7C. The large red regions here match well with the yellow of Fig. 6.7B, as do the small specks of yellow and red across the Ag pad. Fig. 6.8 compares two damaged pixels between flight sample 5 and control sample 9. Front images of each sample provided in Fig. 6.8A and C, respectively, contrast

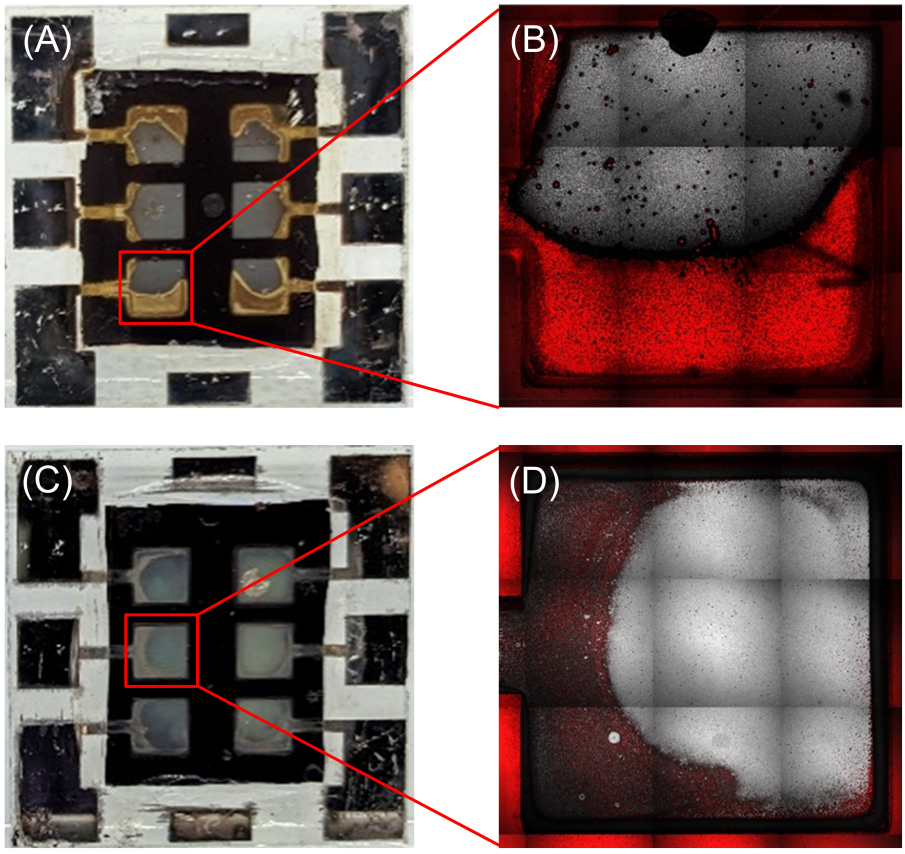


Figure 6.8: Comparison of flight and control Ag degradation. *(A) Front image of FA-rich triple cation sample 5. (B) Combined reflection and PL confocal image of pixel E. (C) Front image of MAPI control sample 9. (D) Combined reflection and PL confocal image of pixel C. Ag degradation is more severe in the flight sample, evidenced by the greater PL signal in the contact area and less reflective Ag with more holes in B. Inset pixels of B and D are 3 x 3 mm.*

the larger, brighter yellow regions of the flight sample pixels with the smaller and duller yellow of the control pixels. From reflective and emissive confocal microscope images in Fig. 6.7B and D, more emission is clearly visible though the partial contact

of the flight sample than the control sample. This bright red region in Fig. 6.8B is a sign of greater Ag damage, revealing more of the MHP beneath. Contrastingly, the PL gathered through the degraded area of Fig. 6.8D is of much lower intensity than the flight sample and appears dim red. The opposite situation is observed for the intensity of light reflected off the remaining Ag portions of each sample. The white area of Fig. 6.8B is much dimmer than that of Fig. 6.8D due to the increased number of holes and overall degradation within. Thus, the reflected and emitted light recorded from samples 5 and 9 demonstrate the greater damage experienced during 8 months in LEO. Fig. 6.9 is presented to better understand how the MHP layer is affected by degraded contacts. The back of MAPI sample 1 (viewed through

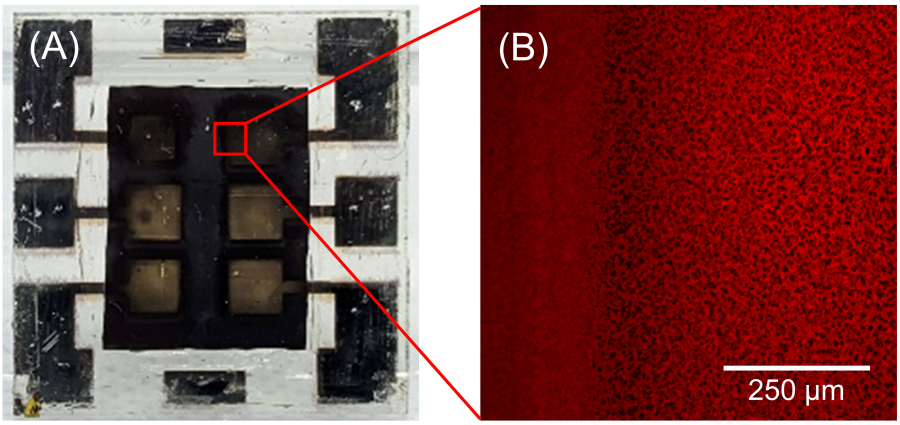


Figure 6.9: MHP between and behind metal contacts. *(A) Back image of MAPI sample 1 taken though substrate. (B) Fluorescence confocal image of region behind Ag contact A (right) and between contacts A and B (left). Note the significant darkening and pitting of the MHP behind the degraded Al contact.*

the substrate) is available in Fig. 6.9A. The edge of pixel A is magnified under confocal fluorescence microscopy in Fig. 6.9B. The right side of the image depicts MHP emission behind the Ag pixel, while the left side of the image contains MHP outside the Ag region. The region behind the damaged pixel is clearly less emissive, appearing rougher and pitted. However, the area outside the pixel is more uniform and appears to have very few non-emissive regions. Apart from the $CsPbI_2Br$ cells, no devices were found without emissive MHP behind their metal contacts. The partial, rather than full, degradation in the perovskite layer permits comparative PL within and between samples, as discussed in the next section.

6.3.2 Photoluminescence Spectroscopy

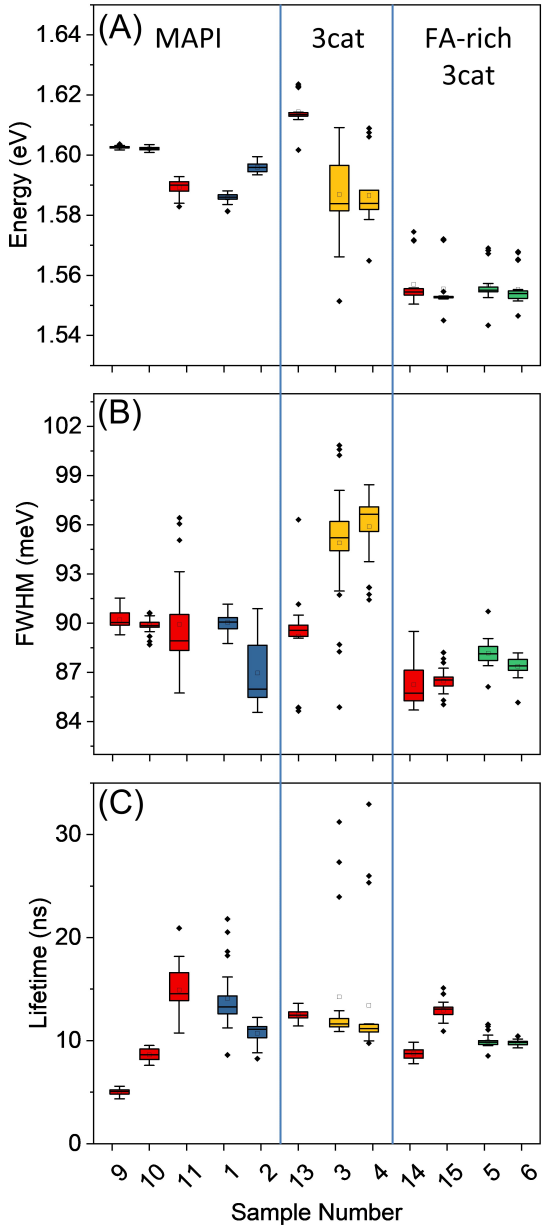


Figure 6.10: Spectral and time-resolved PL between metal contacts. *Control samples (in red) and flight samples excited in their centers, between pixels C and D. (A) energy, (B) FWHM and (C) charge recombination lifetime for all non-$CsPbI_2Br$ devices, which returned non-emissive.*

To properly record the optical behavior of the MISSE-15 samples, multiple high-resolution PL maps were taken across each sample in a 1.8 x 2 mm grid. The emitted light from each sample passed through a beamsplitter to be analyzed both spectrally and temporally. From these two methods one can fully describe the energy and full width at half maximum (FWHM) of the Gaussian signal, as well as the charge recombination lifetime of the perovskite. These three parameters are presented as box plots for each sample (excluding $CsPbI_2Br$) between metal contacts in Fig. 6.10. For all three plots, red boxes denote control samples, blue MAPI flight samples, yellow triple cation flight samples, and green FA-rich triple cation flight samples. Overall, the three types of flight samples behave similarly to their respective controls and show few signs of defects. FA-rich triple cation flight samples returned to Earth with almost no energetic change compared to their controls, as seen in Fig. 6.10A. The maximum average energy difference between flight and control samples is seen among triple cation cells in Fig. 6.10A. On average, these devices are 27.4 meV lower in energy than control sample 13. While this gap is similar to the difference between MISSE-13 flight and control samples post flight, several overlapping data points exist between flight and control samples due to broad energetic variation across samples. Likewise, while the greatest FWHM difference in Fig. 6.10B is found between triple cation flight and control samples, this value is only 5.8 meV. As with energy, the variation across each sample results in overlapping linewidths despite this difference in average values. The FWHM of all other flight samples differs from their controls in average linewidth of 1-3 meV. Additionally, the charge recombination lifetimes plotted in Fig. 6.10C show close agreement between flight and control devices. Variation between devices is greater than within devices, as seen in MAPI control samples 9-11. The source of long lifetime outliers in triple cation flight samples 3 and 4 is not fully understood and the project is ongoing. To better understand how the MHP layer was affected by contact degradation, PL maps were taken both between and behind pixels of MAPI flight sample 1. This data is provided in Fig. 6.11 for maps taken through the front and back side of the sample for pixels A and E, and through the top glass only for a region of MHP between pixels denoted X. Images of the front and back of sample 1 with labels marking map locations are displayed in Fig. 6.11A and B, respectively. Pixel A was chosen to compare with pixel E because it appeared the least degraded of the six and the least yellow as viewed through the substrate. The differences in MHP emission between these two regions are somewhat subtle, though follow an expected trend. In Fig. 6.11C, both the front and back maps of pixel E yield average energies roughly 4 meV higher than pixel A. Meanwhile, region X is energetically red shifted more than 20 meV. These results suggest that the MHP in both pixel regions is degraded compared to the MHP between pixels, though the more yellow Ag of pixel E is indicative of greatest damage. The range of average linewidths in Fig. 6.11D is less than 3 meV across all maps. This is far less than the FWHM variation across the front side of pixel A and is physically insignificant.

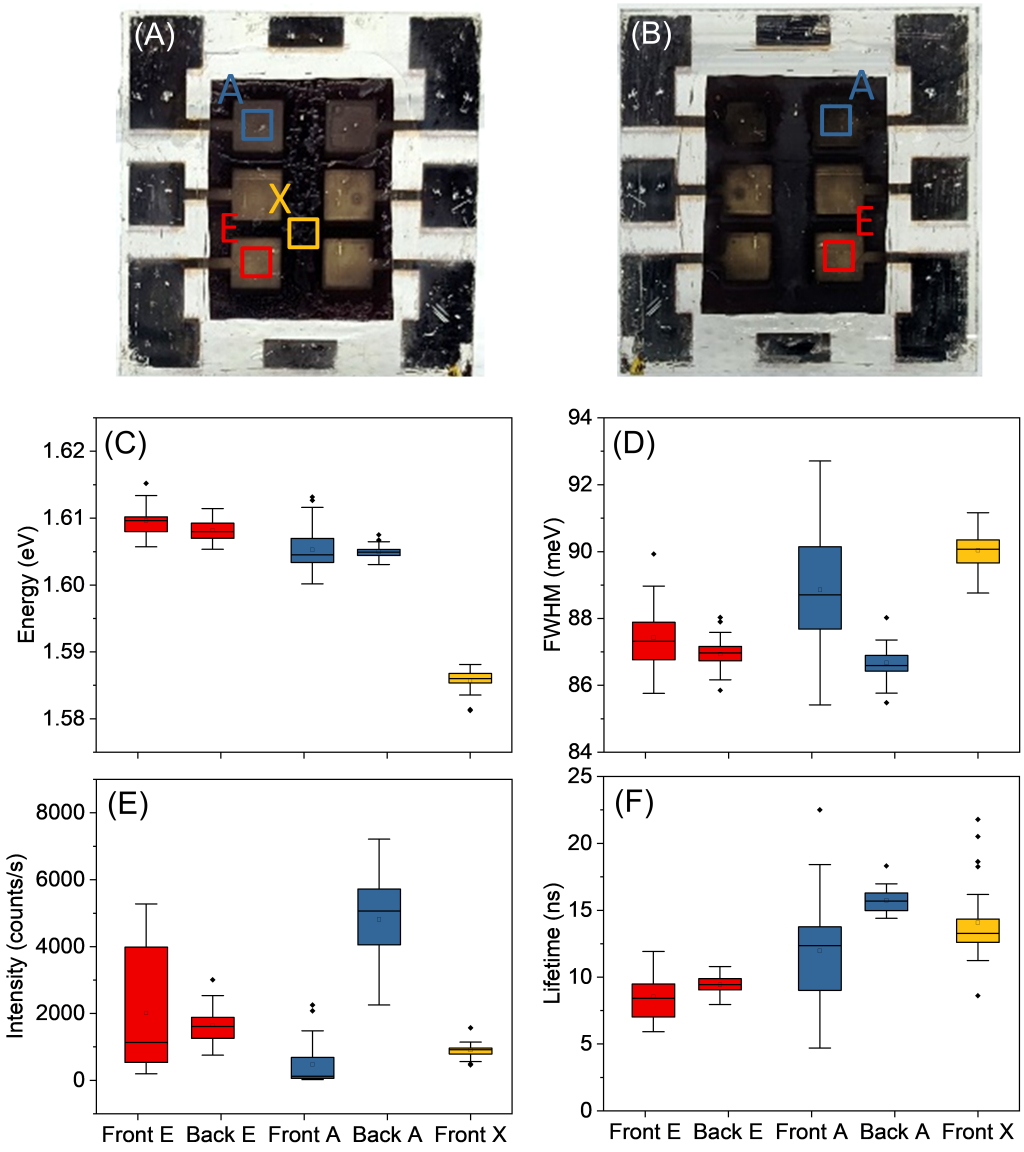


Figure 6.11: PL metrics for three regions of MAPI sample 1. *(A) Front and (B) back images of sample 1 showing area of PL maps taken in pixel A, E, and between pixels (denoted X). (C) energy, (D) FWHM, (E) PL intensity, and (F) charge recombination lifetime for all three areas measured through each side of the sample. Region X was not measured though the substrate.*

PL intensity, provided in Fig. 6.11E, tells a similar story to emission energy. The lowest PL intensity of all regions was found from the front side of pixel A. This is expected due to the remaining Ag contact blocking the MHP layer. Conversely, the back of pixel A yields the highest PL signal since the MHP has fewer defects than in

region E and the Ag will reflect any emitted light toward the receiver. The greatest PL intensity variation is observed in the front map of pixel E. This is likely due to the device layer being excited at each location in the map. One area may consist primarily of Ag, while another is mostly MHP, having been revealed by the degraded Ag. The back of pixel E should increase in PL intensity for the same reasons as pixel A; the remaining Ag reflects emitted light toward the receiver and the back of the MHP layer is less likely to be damaged by the metal contact than the front of the film. Regarding recombination lifetimes in Fig. 6.11F, the MHP of pixel A performs better than pixel E, and the less damaged back side of the absorber yields longer average lifetime than the front side for each pixel. Similar average lifetimes are seen in regions X and A, indicating that the energetic blue shift in region A has little impact on absorption or radiative charge recombination. Altogether, these results reinforce conclusions from section 6.3.1, notably that the MHP layer behind metal contacts is degraded and this degradation is not uniform across all pixels of a device. Fig. 6.12 further addresses the PL differences of Fig. 6.11 by mapping MHP emission behind a corner of intact Ag on FA-rich triple cation control sample 14.

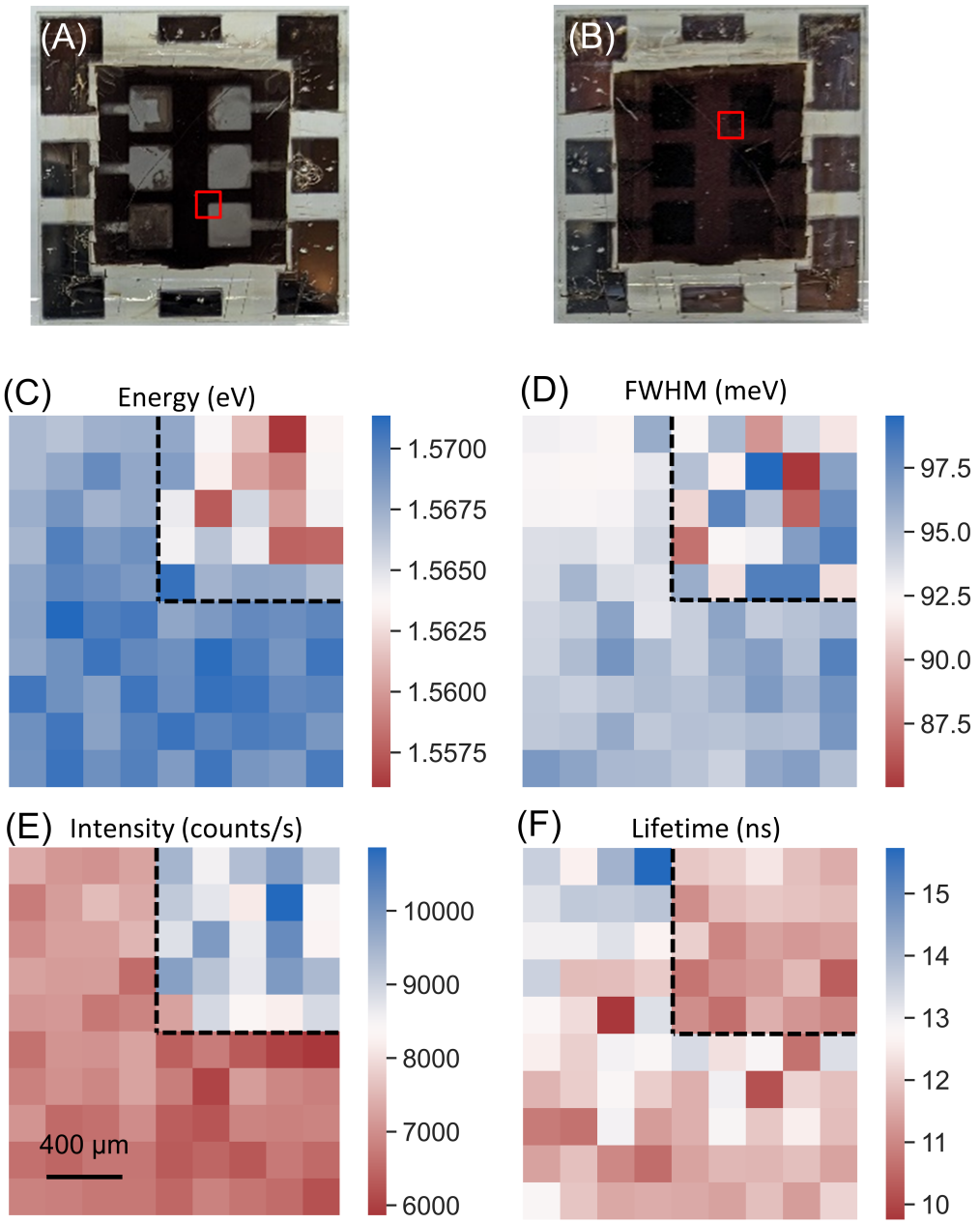


Figure 6.12: PL and TRPL maps of intact Ag region. *(A) Front image of FA-rich triple cation control sample 14. (B) Back image of sample 14 with area of map taken through substrate in red (sample has been flipped top-to-bottom from front image). Heatmaps of (C) energy, (D) FWHM, (E) PL intensity, and (F) charge recombination lifetime. Top right region (within dashed black line) maps MHP behind intact Ag contact while remaining area is between contacts.*

Pixel F was chosen because of the minimal degradation visible in the region. Fig. 6.12A and B provide images of the front and back of sample 14 with a red rectangle denoting the area which was mapped. The sample was scanned through its substrate in order to measure the MHP behind the pixel, as marked in Fig. 6.12B. Each of four PL metrics is presented as its own heatmap in Fig. 6.12C – F. The dashed black line represents the MHP behind the Ag of pixel F, while the remaining area of each plot is between pixels. Energetically, the MHP behind the pixel in Fig. 6.12C is red shifted by roughly 10 meV compared to the region outside the pixel. This behavior is opposite that of Fig. 6.11C, suggesting that sample 14 has degraded differently than the flight samples. The FWHM of Fig. 6.12D reaches its highest and lowest values within the pixel. This range is also 10 meV and shows the nonuniformity of perovskite material near the metal contact. As discussed in Fig. 6.11E, the PL intensity behind the pixel in Fig. 6.12E is much greater than the surrounding area due to the reflective back of the Ag contact. Finally, average recombination lifetime in the pixel region of Fig. 6.12F is mostly uniform and shorter than the surrounding area. This is generally a sign of increased trap states and other defects encouraging nonradiative recombination. Similar PL analysis is provided for an interesting region of FA-rich triple cation sample 5 in Fig. 6.13 for comparison. Here, the same size map as in sample 14 was recorded at the edge of pixel A, where the degraded and intact Ag regions meet. Fig. 6.13A highlights this region in a front image of sample 5, contrasting the yellow and grey Ag. In order to measure the MHP beneath the pixel, sample 5 was excited through its substrate as in Fig. 6.13B. The top right corner of Fig. 6.13C – F (roughly captured by the dashed black line) contains MHP behind the degraded Ag seen in yellow in the front and back images of the sample. The bottom right corner of these images contains MHP behind the Ag pixel which has not turned yellow, while the rest of the maps are outside the pixel area.

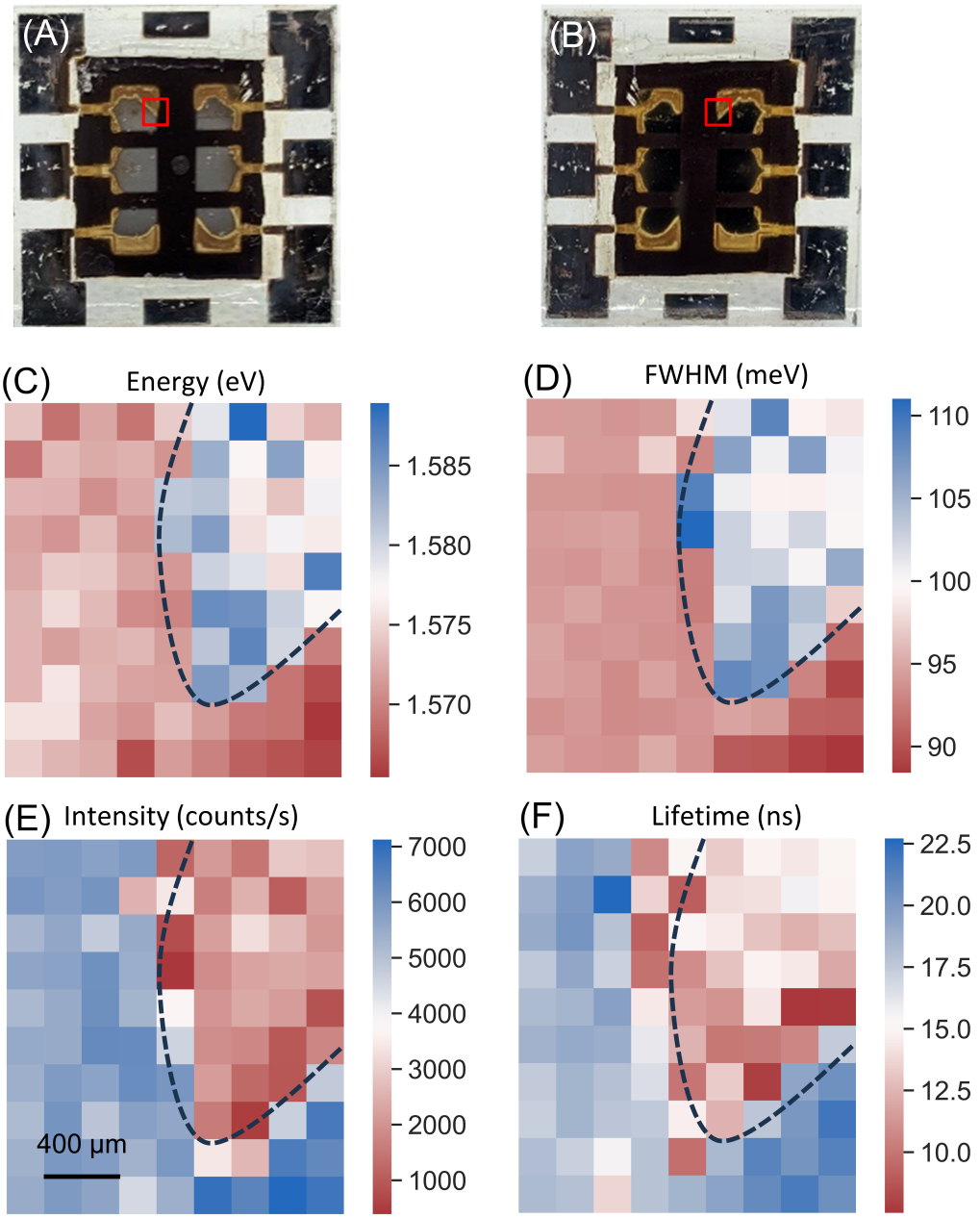


Figure 6.13: PL and TRPL maps of degraded Ag region. *(A) Front image of FA-rich triple cation sample 5. (B) Back image of sample 5 with area of map taken through substrate in red. Heatmaps of (C) energy, (D) FWHM, (E) PL intensity, and (F) charge recombination lifetime. Top right region (within dashed black line) maps partially-degraded MHP, bottom right is MHP behind intact Ag contact, and left side is MHP between pixels A and B.*

As in the MHP behind degraded pixels of Fig. 6.11C, the top right corner of sample 5 energetically blue shifted over 10 meV compared to the rest of the film in Fig. 6.13C. However, the region behind the intact Ag red shifted compared to the film in the left half of the map. This behavior was also seen in the energy shift of Fig. 6.12C. The FWHM of the degraded region in Fig. 6.13D was 15 meV larger than the MHP outside the pixel. For reasons not fully understood, the linewidth within the intact Ag region was the smallest in the map, agreeing with Fig. 6.12D. As expected, the PL intensity in Fig. 6.13E was lowest in the degraded region and highest behind the reflective Ag. Finally, the average recombination lifetime was below 15 ns in the degraded contact region and up to 22.5 ns in the reflective region. It is unclear why low lifetimes reached beyond the dashed line unlike the other PL metrics. This spatial analysis of the flight sample and previous control supports the microscopic data from section 6.3.1 both spectrally and temporally. MHP films behind damaged, yellow contacts are consistently found with greater energy, lower PL intensity, and shorter lifetimes than MHP between pixel regions.

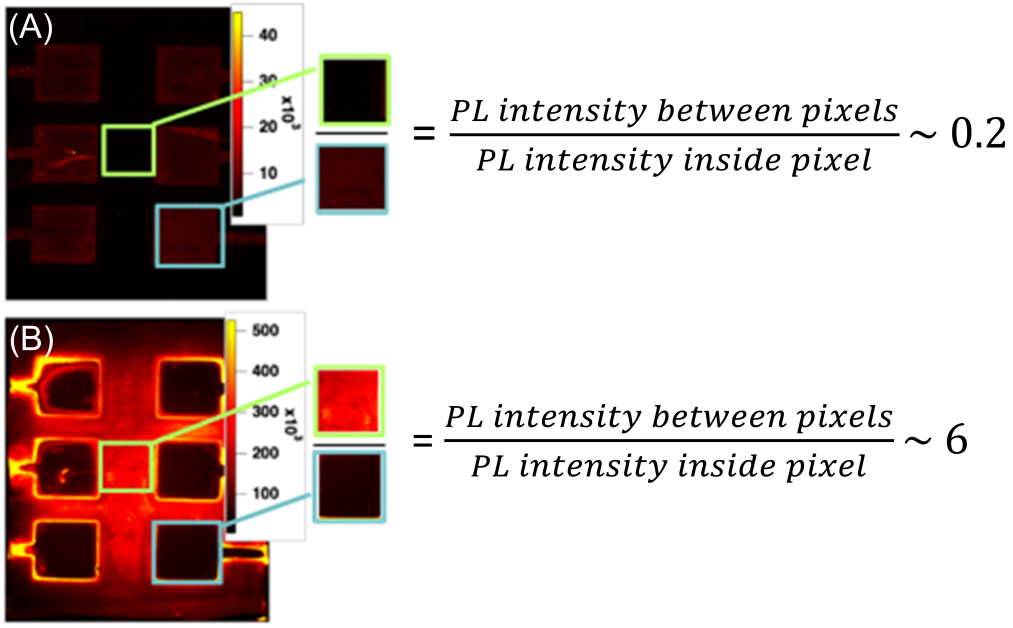


Figure 6.14: PL redistribution in MAPI sample 1. *Spectral camera capturing PL through the substrate of sample 1 (A) pre flight and (B) post flight. Degradation of MHP layer behind Ag contacts post flight results in fewer charges extracted overall and greater emission in MHP between pixels.*

An additional PL investigation, provided in Fig. 6.14, was conducted by Steve Johnston and Kaitlyn VanSant at NREL pre and post flight. Here, MHP emission intensity was captured with a spectral camera through the substrate of MAPI sample

1. In Fig. 6.14A, most radiative recombination occurs within pixel regions pre flight. Recombination is very low across the sample, as charges are being extracted by the top and bottom contacts. The slightly increased PL within the pixels is likely due to the reflective back of the Ag pads directing photons toward the detector. In comparison, PL within the pixel regions is much dimmer than between pixels post flight in Fig. 6.14B. As discussed throughout this section, degraded MHP behind damaged pixels is far less emissive than the surrounding film. The increase in PL between pixels by several orders of magnitude post flight is primarily due to the electrical failure of the top contacts. Without proper charge extraction, electrons and holes can radiatively recombine within the MHP film. This PL redistribution post flight is seen in most MISSE-15 samples, as they all experienced some degree of top contact failure.

6.4 Conclusion

Despite electrical disconnection due to Ag and Al degradation, all MISSE-15 hybrid MHP samples remained emissive between contacts after eight months in LEO. The complete photobleaching of $CsPbI_2Br$ control sample 12, as well as flight samples 7 and 8, indicates the entire batch was unstable. The failure of these samples does not reflect on fully inorganic MHPs in general, but simply a material synthesis or sample fabrication approach that needs addressing. Similar to the flight samples of MISSE-13 and 16, the devices herein showed no signs of damage from proton irradiation, UV exposure, or the increased AM0 light intensity. This chapter focused instead on microscopy and spectroscopy to investigate damaged Ag and Al contacts, as well as the MHP layer behind each. While the exact cause of metal migration is not understood and work is ongoing, both Ag and Al were found to penetrate the cell stack and damage the MHP layer. Ag pixels across all flight samples yellowed from the edge inward, degrading more extensively and uniformly than the Al contacts. The Al pixels of triple cation flight samples 3 and 4 feature smaller, more isolated yellow regions. This damage is less uniform, as some pixels appear almost unchanged while others are mostly yellow. All five control samples containing Ag feature pixel damage, though far less severe than the flight samples. The two control samples with Al contacts show no signs of decay or migration. Ultimately, microscopic and spectroscopic data revealed partially damaged MHP behind yellow contacts. Perovskites were energetically blue shifted and of shorter lifetimes in these areas. This damage was highly localized, as these PL metrics returned to normal within 100 µm of yellow contacts. These results have already informed researchers who are planning future experiments in space. MISSE-19, currently underway, is utilizing new MHP device architectures without Ag or Al top contacts to avoid ion migration. These cells, containing a protective ITO layer and Au pixels, will soon return to Earth and reveal their stability.

Chapter 7

Conclusion and Future Work

This dissertation has delved into the remarkable world of perovskites, investigating their viability as a power source for LEO missions. Through a comprehensive series of experiments, both ground-based and aboard the ISS, we have gained invaluable insights into the behavior and resilience of these materials in the harsh space environment. The pioneering MISSE-13 mission, which saw the first perovskite sample orbit the Earth, laid the foundation for understanding the material's response to the extraterrestrial environment. Before this mission, few researchers in the perovskite field would have expected MHPs to survive the stressors of LEO for 10 months. Despite enduring nearly 4,800 orbits, the flight sample exhibited no irreversible degradation, with its recombination lifetime and optical bandgap fully recovering after 15 hr AM1.5 illumination. Building upon the success of MISSE-13, the MISSE-16 mission delved deeper into the effects of UV radiation on MHPs. Employing a range of top glass materials, including UV band-pass filters and high-transmission glasses, the flight samples returned largely unaffected by the unfiltered AM0 solar spectrum. Remarkably, none of the samples exhibited signs of UV damage, further solidifying the robustness and potential of perovskites for space applications. To complement the ISS missions, a comprehensive terrestrial study was conducted to investigate the impact of particle radiation on unencapsulated perovskite films. While neutron irradiation had no measurable impact, proton fluences above $1x10^{13}$ cm^{-2} resulted in clear signs of damage, including photodarkening, energetic blue shifts, and reduced radiative recombination lifetimes. Such fluences are several orders of magnitude higher than would be accumulated in a multi-decade LEO mission. These findings highlight the remarkable radiation tolerance of MHPs while underscoring the importance of shielding and encapsulation strategies for fully realized PSCs in space. The culmination of this research was the MISSE-15 mission, which examined the performance of complete PSC architectures in the LEO environment. Although the metallic contacts exhibited partial degradation, the perovskite layers themselves remained emissive and comparable to their ground control counterparts after eight months of exposure. This

remarkable result further validates the self-healing capabilities of perovskites, paving the way for their future implementation in space-based power systems. Throughout this body of work, several key advantages of perovskites for space photovoltaics have been highlighted:

1. Radiation Tolerance and Self-Healing: Perovskites have demonstrated an exceptional ability to recover from radiation-induced defects, owing to their unique defect physics and dynamic structural rearrangements. This inherent self-healing capability ensures long-term performance and reliability in the harsh radiation environment of space.

2. Tunable Bandgaps: The ability to precisely tune the bandgap of perovskites by adjusting their chemical composition allows for optimal light absorption and increased efficiency under the AM0 solar spectrum encountered in space.

3. Low-Temperature Performance: Unlike many conventional solar cell technologies, perovskites maintain high efficiencies even at extremely low temperatures, making them well-suited for missions involving extreme thermal cycling and extended periods of cold.

4. Lightweight and High Specific Power: The thin-film nature of perovskite solar cells enables the realization of lightweight and high specific power devices, minimizing payload weight and directly impacting launch costs and mission feasibility.

5. Cost-Effective Manufacturing: The solution-processable fabrication of perovskites enables low-cost deposition techniques and roll-to-roll manufacturing, contributing to the potential for sustainable and economically viable space power solutions.

As the cost of accessing space continues to decrease and the demand for reliable power sources grows, perovskites stand poised to play a pivotal role in enabling future space missions and driving the commercialization of LEO. However, further research and development are necessary to address remaining challenges such as long-term stability, encapsulation strategies, and large-scale manufacturing processes. This dissertation has laid a solid foundation for the application of perovskites in space photovoltaics, but the journey has only just begun. Several questions remain from this work which warrant further investigation. While the devices in each study experienced varying levels of damage, only the terrestrial proton beam experiment was conducted to the point of sample failure. Significant knowledge can be gained by subjecting MHP cells to other LEO stressors until failure. A thorough failure analysis would help place the partial degradation seen in this thesis in context. As previously stated, it is difficult to replicate several variables of the LEO environment in the laboratory. Whether

through future MISSE missions or clever experimentation in the lab, more stress testing is certainly needed to understand, improve, and eventually utilize MHPs in space.

Appendix A

Experimental Background and Methods

A.1 Photoluminescence Spectroscopy

Photoluminescence is the process by which a semiconductor material absorbs light, then reemits light of lower energy. This process can be described with an idealized three step process. First, a photon of light with greater energy than the bandgap of the semiconductor must be absorbed. Upon absorption, an electron is promoted from the valence band of the material into the continuum states of the conduction band, leaving a positively charged hole behind. Next, the electron quickly relaxes to the conduction band edge, releasing any energy above the bandgap as phonons in the crystal lattice. Finally, the electron recombines with the hole in the valence band, producing a photon with the same energy as the bandgap of the semiconductor. For a given laser pulse, the excited electron number density $N(t)$ in the MHP conduction band will radiatively recombine with average lifetime T_1 as $N(t) = N_0 e^{-t/T_1}$. This recombination lifetime is vital in device performance, as excited charges with long lifetimes are more likely to be extracted by the solar cell electrodes before recombining. Along with time-resolved PL, emission is directed into a spectrometer for spectral resolution. This data is fit with a Gaussian function as $I_{PL}(x) = ae^{-4ln(2)(x-x_{center})^2/FWHM^2}$, where $I_{PL}(x)$ is the intensity of emitted light as a function of wavelength. By representing the Guassian in this form, it is simple to extract the most useful variables of the fit. The full width at half maximum (FWHM) and center wavelength (x_{center}) of the peak are evident, while the integrated intensity is simply $Intensity = a * FWHM * \sqrt{2\pi}$. This process is the backbone of the spectroscopic data presented throughout this thesis. In each chapter, MHP films were excited with light above their bandgap from either a laser or solar simulator. The emitted light from the perovskite was carefully directed into a spectrometer and/or photodiode to record spectral and temporal information, as described in Section A.3.

A.2 Perovskite Electronic Structure

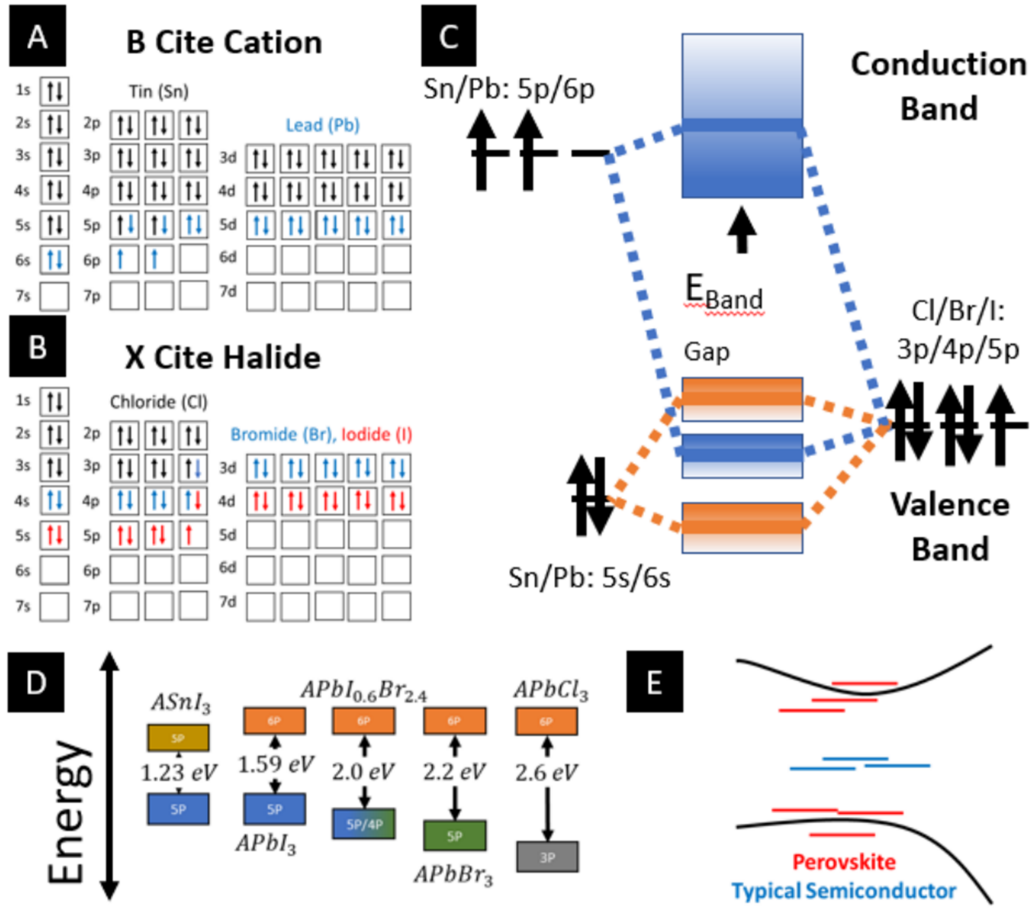


Figure A.1: Halide perovskite band contributions. *Typcial orbital structure of the (A) Sn and Pb metals, as well as the (B) Cl, Br, and I halides found in MHPs. (C) Formation of perovskite bandgap from the overlapping metal and halide atomic orbitals. (D) Calculated bandgap for perovskite crystals with varying chemistries. (E) Cartoon of energetic postions of trap states in the MHP bandgap compared to other semiconductors [3].*

The unique ABX_3 crystal structure which defines perovskites produces an interesting collection of atoms with partially filled atomic orbitals. The A site cation has been demonstrated to contribute little to the band structure, so focus will first be given to the B site metals Pb and Sn [107]. Sn atoms have fully occupied 5s orbitals with only two electrons in 5p. Similarly, Pb has a full 6s shell and only two electrons in 6p (Fig. A.1A). The X site halides Cl, Br, and I fill all but one electron in the 3p,

4p, and 5p orbitals, respectively (Fig. A.1B). The overlap of all atomic orbitals in the lattice form the electronic bands of the perovskite sample. From density functional theory, the valence band maximum arises from the hybridization of the 3p/4p/5p halide states with the fully occupied 5s/6s metal orbitals [108]. The conduction band minimum, however, is constructed from the partially filled 5p and 6p levels among the metal atoms. This arrangement is depicted in Fig. A.1C.

By changing the constituent atoms in a perovksite lattice, researchers can directly modify its bandgap. A representation of bandgap shift is presented in Fig. A.1D. Again focusing on the metal/halide effects, the smallest bandgap (1.23 eV) is found in the $ASnI_3$ perovskite [109]. This is due to the 5p I orbital having the highest valence band contribution, while the 5p Sn orbital lowers the conduction band edge. Opposite this configuration, the $APbCl_3$ crystal has the largest bandgap (2.6 eV) from the 3p Cl and 6p Pb orbitals. The majority of the samples studied in this work were MAPI, found near the predicted 1.59 eV of $APbI_3$ in Fig. A.1D. Along with chemical tunability of bandgap, the electronic structure of perovskites allows for high defect tolerance. MHPs exhibit mostly antibonding valence and conduction band character, as depicted in Fig. A.1C. Point defects (mostly vacancies) thus create shallow traps as suggested in Fig. A.1E [9]. This contrasts with most semiconductors, whose valence band maximum is generally bonding, which results in deep intrinsic defects [110]. These traps are represented as blue lines in Fig. A.1E.

A.3 Methods

Photoluminescence (PL) Spectroscopy: Samples were excited with a pulsed 532 nm laser light (NKT Photonics SuperK acousto-optic system) with a repetition rate of 39 MHz into an 100x magnification optical objective. For this objective, the laser spot size on the sample was approximately 2 µm in diameter with a laser power was approximately 60 µW. Light emitted from the samples was filtered by a 715 nm long pass filter before reaching the spectrometer (Princeton Instruments Acton 2300) and single photon avalanche diode (SPAD, PicoQuant PDM series, 4 ps time bin). The Gaussian PL profile was centered at 780 nm. The spectrometer head utilized a 500 nm blaze grating with 300 lines/mm to disperse the collected excitation into the CCD device. Spectral and temporal data was captured by the software which accompanied each machine, then further analyzed in Python and other mathematical programs.

Confocal Microscopy: A Zeiss LSM 880 Confocal Laser Scanning Microscope was used to capture the reflected and emitted light from MHP films. Samples were excited with a 405 nm laser at various power depending on microscope zoom and intensity of PL signal. By quickly raster scanning the laser, regions as large as 1 mm^2 were observed in video to find defects and other interesting features. Reflection images of the samples were collected by filtering light other than 400-410 nm. Emission images

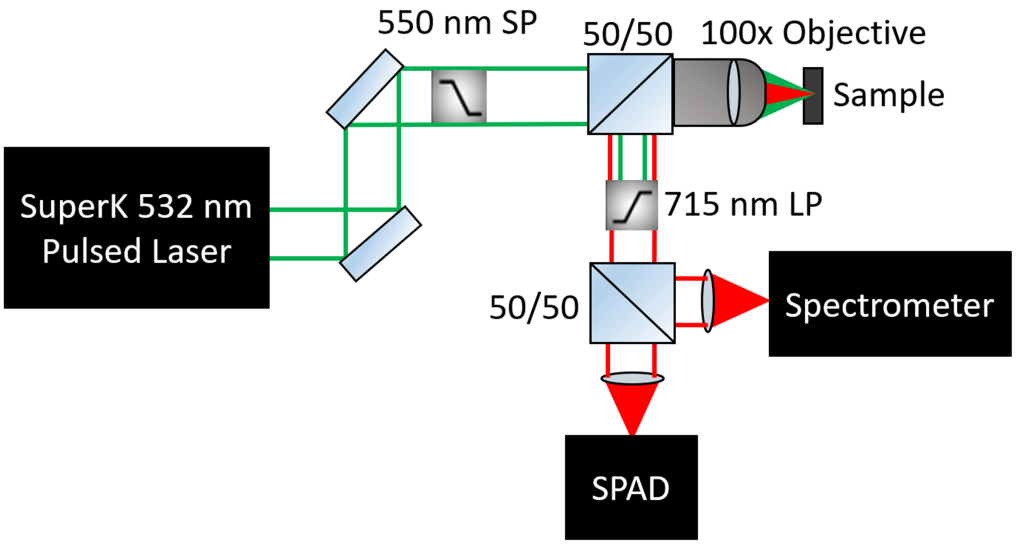


Figure A.2: PL/TRPL collection schematic. *A home-built laser system was used to collect all PL data presented in this thesis. From the SuperK laser, the beam is reflected from two adjustable mirrors to ensure proper alignment. The first 50/50 beamsplitter allows the laser to reach the sample while also redirecting the PL. After the laser is removed with a 715 long pass filter, the second beam splitter divides the PL equally between the single photon avalanche diode and spectrometer.*

were taken by filtering light other than 750-800 nm.

PL Mapping: PL was taken with a 100x Olympus objective as described above while each sample was translated with Newport 300 stages via a custom LabVIEW program. Most samples were mapped in a 5 x 5 grid across 1 mm^2 to provide a simple survey of optical data. These maps are primarily presented as box and whisker plots throughout this thesis to easily compare variable distributions between devices. Where useful, maps of higher resolution and/or larger area were constructed to provide spatial data of interesting features.

Temperature Dependence: To measure PL at low temperatures, samples were loaded into either a Montana Instruments 4200 or Advanced Research Systems DE-204NF cryostation. While at a vacuum of 90 µTorr, PL and time-resolved PL (TRPL) data were recorded every 10 K between 10 and 290 K.

AM1.5 Stability: PL was measured every 5 min for up to 15 h under continuous illumination of a AM1.5 solar simulator (Newport LSH-7320 ABA LED Solar Simulator). The simulated sunlight was filtered with 675 nm short pass filter before

reaching the sample. Additionally, a 750 nm short pass filter was implemented in front of the sample in each test to filter infrared light from the simulator that obscured the PL signal. A 675 long pass filter was used in the collection path in all tests to remove the effects of the solar simulator and record only light emitted from the sample. The PL signal was transmitted by fiber optic cable into a Princeton Instruments Acton 2300 spectrometer.

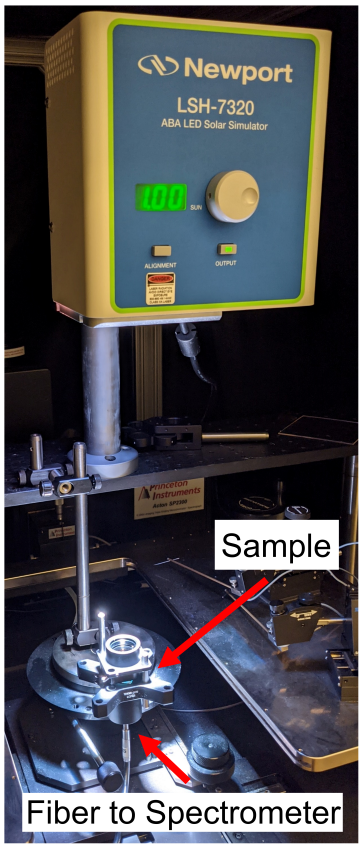


Figure A.3: Lightsoaking configuration. *Photograph of Newport LSH-7320 Solar Simulator and sample aligned beneath. The MHP device has been placed between the necessary filters at the proper distance from the simulator to best imitate the AM1.5 spectrum. A fiber optic cable below the sample captures PL and sends it to the Actron 2300 Spectrometer.*

Irradiation: Proton irradiations were performed in Ion Beam Laboratory at the University of North Texas. 20 keV proton beams were generated from TiH cathode by using Source of Negative Ion by Cesium Sputtering (SNICS-II, NEC). Protons beams were raster scanned over the region of interest using electrostatic raster scanner for

uniform irradiation in the low energy irradiation chamber. All irradiations were performed in the vacuum chamber under a vacuum of 1x10^{-7} torr. Neutron irradiations were performed at NASA Langley Research Center using Am/Be (1 Curie) neutron source to generate fast neutrons (4.5 MeV).

Stopping Range of Ions in Matter (SRIM) Calculation Information: The range and collision profile of the energetic protons in the samples were simulated by using SRIM ion-solid interaction software package using 100,000 ions with the following layer details; perovskite: 600 nm, 4.286 g/cm^3; ITO: 100 nm, 7.14 g/cm^3; borosilicate glass: 200 nm, 2.23 g/cm^3. The glass was simulated at this narrow width to speed calculations, but was nominally 1 mm thick.

Bibliography

[1] Best Research-Cell Efficiency Chart. NREL. https://www.nrel.gov/pv/cell-efficiency.html, 2024.

[2] William Delmas, Samuel Erickson, Jorge Arteaga, Mark Woodall, Michael Scheibner, Timothy S. Krause, Kyle Crowley, Kaitlyn T. VanSant, Joseph M. Luther, Jennifer N. Williams, Jeremiah McNatt, Timothy J. Peshek, Lyndsey McMillon-Brown, and Sayantani Ghosh. Evaluation of Hybrid Perovskite Prototypes After 10-Month Space Flight on the International Space Station. *Advanced Energy Materials*, 13(19):2203920, 2023. _eprint: https://onlinelibrary.wiley.com/doi/pdf/10.1002/aenm.202203920.

[3] William Delmas. *Organo-Metalic Halide Perovskite Photonics*. PhD thesis, University of California, Merced, 2022.

[4] Valentino Romano, Antonio Agresti, Rosaria Verduci, and Giovanna D'Angelo. Advances in Perovskites for Photovoltaic Applications in Space. *ACS Energy Letters*, 7(8):2490–2514, August 2022. Publisher: American Chemical Society.

[5] Jianming Yang, Qinye Bao, Liang Shen, and Liming Ding. Potential applications for perovskite solar cells in space. *Nano Energy*, 76:105019, October 2020.

[6] Yongguang Tu, Jiang Wu, Guoning Xu, Xiaoyu Yang, Rong Cai, Qihuang Gong, Rui Zhu, and Wei Huang. Perovskite Solar Cells for Space Applications: Progress and Challenges. *Advanced Materials*, 33(21):2006545, 2021. _eprint: https://onlinelibrary.wiley.com/doi/pdf/10.1002/adma.202006545.

[7] Wenjing Yu, Xiaoran Sun, Mu Xiao, Tian Hou, Xu Liu, Bolin Zheng, Hua Yu, Meng Zhang, Yuelong Huang, and Xiaojing Hao. Recent advances on interface engineering of perovskite solar cells. *Nano Research*, 15(1):85–103, January 2022.

[8] Taylor Moot, Jay B. Patel, Gabriel McAndrews, Eli J. Wolf, Daniel Morales, Isaac E. Gould, Bryan A. Rosales, Caleb C. Boyd, Lance M. Wheeler, Philip A.

Parilla, Steven W. Johnston, Laura T. Schelhas, Michael D. McGehee, and Joseph M. Luther. Temperature Coefficients of Perovskite Photovoltaics for Energy Yield Calculations. *ACS Energy Letters*, 6(5):2038–2047, May 2021. Publisher: American Chemical Society.

[9] Guan-Woo Kim and Annamaria Petrozza. Defect Tolerance and Intolerance in Metal-Halide Perovskites. *Advanced Energy Materials*, 10(37):2001959, 2020. _eprint: https://onlinelibrary.wiley.com/doi/pdf/10.1002/aenm.202001959.

[10] Afshan Jamshaid, Zhendong Guo, Jeremy Hieulle, Collin Stecker, Robin Ohmann, Luis K. Ono, Longbin Qiu, Guoqing Tong, Wanjian Yin, and Yabing Qi. Atomic-scale insight into the enhanced surface stability of methylammonium lead iodide perovskite by controlled deposition of lead chloride. *Energy & Environmental Science*, 14(8):4541–4554, 2021. Publisher: Royal Society of Chemistry.

[11] Mathilde Bouchard, Jan Hilhorst, Stéphanie Pouget, Firoz Alam, Maria Mendez, David Djurado, Dmitry Aldakov, Tobias Schülli, and Peter Reiss. Direct Evidence of Chlorine-Induced Preferential Crystalline Orientation in Methylammonium Lead Iodide Perovskites Grown on TiO2. *The Journal of Physical Chemistry C*, 121(14):7596–7602, April 2017. Publisher: American Chemical Society.

[12] Eugene A. Katz. Perovskite: Name puzzle and german-russian odyssey of discovery. *Helvetica Chimica Acta*, 103(6):e2000061, 2020.

[13] Akihiro Kojima, Kenjiro Teshima, Yasuo Shirai, and Tsutomu Miyasaka. Organometal Halide Perovskites as Visible-Light Sensitizers for Photovoltaic Cells. *Journal of the American Chemical Society*, 131(17):6050–6051, May 2009. Publisher: American Chemical Society.

[14] Michael M. Lee, Joël Teuscher, Tsutomu Miyasaka, Takurou N. Murakami, and Henry J. Snaith. Efficient Hybrid Solar Cells Based on Meso-Superstructured Organometal Halide Perovskites. *Science*, 338(6107):643–647, November 2012. Publisher: American Association for the Advancement of Science.

[15] Fei Ma, Yang Zhao, Zihan Qu, and Jingbi You. Developments of highly efficient perovskite solar cells. *Accounts of Materials Research*, 4(8):716–725, 2023.

[16] Linfeng Ye, Pengfei Guo, Jie Su, Kaiyuan Zhang, Chen Liu, Penghui Yang, Wenhao Zhao, Pengzhen Zhao, Zhe Liu, Jingjing Chang, Qian Ye, and Hongqiang Wang. Managing secondary phase lead iodide in hybrid perovskites via surface reconstruction for high-performance perovskite solar cells with robust environmental stability. *Angewandte Chemie International Edition*, 62(18):e202300678, 2023.

[17] Tinghuan Yang, Lili Gao, Jing Lu, Ma Chuang, Yachao Du, Wang Peijun, Zicheng Ding, Shiqiang Wang, Peng Xu, Dongle Liu, Haojin Li, Xiaoming Chang, Junjie Fang, Wenming Tian, Yingguo Yang, Shengzhong Liu Frank Liu, and Kui Zhao. One-stone-for-two-birds strategy to attain beyond 25solar cells. *Nature Communications*, 14, 02 2023.

[18] Sanwan Liu, Vasudevan Biju, Yabing Qi, Wei Chen, and Zonghao Liu. Recent progress in the development of high-efficiency inverted perovskite solar cells. *NPG Asia Materials*, 15, 05 2023.

[19] Noor Titan Hartono, Hans Köbler, Paolo Graniero, M. Khenkin, Rutger Schlatmann, Carolin Ulbrich, and Antonio Abate. Stability follows efficiency based on the analysis of a large perovskite solar cells ageing dataset. *Nature Communications*, 14, 08 2023.

[20] Stefaan De Wolf, Jakub Holovsky, Soo-Jin Moon, Philipp Löper, Bjoern Niesen, Martin Ledinsky, Franz-Josef Haug, Jun-Ho Yum, and Christophe Ballif. Organometallic halide perovskites: Sharp optical absorption edge and its relation to photovoltaic performance. *The Journal of Physical Chemistry Letters*, 5(6):1035–1039, 2014. PMID: 26270984.

[21] Gede Adhyaksa, Pim Veldhuizen, Yinghuan Kuang, Sarah Brittman, R.E.I. Schropp, and Erik Garnett. Carrier diffusion lengths in hybrid perovskites: Processing, composition, aging and surface passivation effects. *Chemistry of Materials*, 28, 07 2016.

[22] Yana Vaynzof. The Future of Perovskite Photovoltaics—Thermal Evaporation or Solution Processing? *Advanced Energy Materials*, 10(48):2003073, 2020. _eprint: https://onlinelibrary.wiley.com/doi/pdf/10.1002/aenm.202003073.

[23] Saewon Kang, Jaeki Jeong, Seungse Cho, Yung Jin Yoon, Seungyoung Park, Seongdong Lim, Jin Young Kim, and Hyunhyub Ko. Ultrathin, lightweight and flexible perovskite solar cells with an excellent power-per-weight performance. *Journal of Materials Chemistry A*, 7(3):1107–1114, January 2019. Publisher: The Royal Society of Chemistry.

[24] Ryne P. Raffaelle. Chapter one - An introduction to space photovoltaics: Technologies, issues, and missions. In Sheila G. Bailey, Aloysius F. Hepp, Dale C. Ferguson, Ryne P. Raffaelle, and Steven M. Durbin, editors, *Photovoltaics for Space*, pages 3–27. Elsevier, January 2023.

[25] Kim K. de Groh and Miria M. Finckenor. *A Researcher's Guide to Space Environmental Effects*. ISS Researcher's Guide Series. NASA ISS Program Science Office, 2020.

[26] Robert Thirsk, Andre Kuipers, Chiaki Mukai, and David Williams. The spaceflight environment: the International Space Station and beyond. *CMAJ : Canadian Medical Association Journal*, 180(12):1216–1220, June 2009.

[27] Yongguang Tu, GuoNing Xu, XiaoYu Yang, Yifei Zhang, ZhaoJie Li, Rui Su, Deying Luo, Wenqiang Yang, Ying Miao, Rong Cai, LuHua Jiang, Xiaowei Du, Yang Yanchu, QianShi Liu, Yang Gao, Shuai Zhao, Wei Huang, QiHuang Gong, and Rui Zhu. Mixed-cation perovskite solar cells in space. *Science China Physics, Mechanics & Astronomy*, 62, July 2019.

[28] Minh Tam Hoang, Yang Yang, Bryan Tuten, and Hongxia Wang. Are Metal Halide Perovskite Solar Cells Ready for Space Applications? *The Journal of Physical Chemistry Letters*, 13(13):2908–2920, April 2022. Publisher: American Chemical Society.

[29] Lawrence E. Murr and William H. Kinard. Effects of Low Earth Orbit. *American Scientist*, 81(2):152–165, 1993. Publisher: Sigma Xi, The Scientific Research Society.

[30] G. M. Paternò, V. Robbiano, L. Santarelli, A. Zampetti, C. Cazzaniga, V. Garcìa Sakai, and F. Cacialli. Perovskite solar cell resilience to fast neutrons. *Sustainable Energy & Fuels*, 3(10):2561–2566, September 2019. Publisher: The Royal Society of Chemistry.

[31] H. Fuqua Haviland, P. F. Bertone, M. J. Christl, J. A. Caffrey, and J. A. Apple. Artemis III Neutron Surface Science. Technical report, September 2020. NTRS Author Affiliations: Marshall Space Flight Center NTRS Document ID: 20205007103 NTRS Research Center: Marshall Space Flight Center (MSFC).

[32] Lawrence W. Townsend. Space weather on the Moon. *Physics Today*, 73(3):66–67, March 2020.

[33] Shuang Yang, Zeyuan Xu, Sha Xue, Praneeth Kandlakunta, Lei Cao, and Jinsong Huang. Organohalide Lead Perovskites: More Stable than Glass under Gamma-Ray Radiation. *Advanced Materials*, 31(4):1805547, 2019. _eprint: https://onlinelibrary.wiley.com/doi/pdf/10.1002/adma.201805547.

[34] Samuel F. Pellicori, Carol L. Martinez, Paul Hausgen, and David Wilt. Development and testing of coatings for orbital space radiation environments. *Applied Optics*, 53(4):A339–A350, February 2014. Publisher: Optica Publishing Group.

[35] Soumya Kundu and Timothy L. Kelly. In situ studies of the degradation mechanisms of perovskite solar cells. *EcoMat*, 2(2):e12025, 2020. _eprint: https://onlinelibrary.wiley.com/doi/pdf/10.1002/eom2.12025.

[36] Yan Jiang, Shih-Chi Yang, Quentin Jeangros, Stefano Pisoni, Thierry Moser, Stephan Buecheler, Ayodhya N. Tiwari, and Fan Fu. Mitigation of Vacuum and Illumination-Induced Degradation in Perovskite Solar Cells by Structure Engineering. *Joule*, 4(5):1087–1103, May 2020.

[37] Weijie Chen, Jingwen Zhang, Guiying Xu, Rongming Xue, Yaowen Li, Yinhua Zhou, Jianhui Hou, and Yongfang Li. A Semitransparent Inorganic Perovskite Film for Overcoming Ultraviolet Light Instability of Organic Solar Cells and Achieving 14.03% Efficiency. *Advanced Materials*, 30(21):1800855, 2018. _eprint: https://onlinelibrary.wiley.com/doi/pdf/10.1002/adma.201800855.

[38] Carsten Baur, Emilio Fernández Lisbona, and José Ramón González. Chapter three - Air mass zero (AM0) studies and solar cell calibration. In Sheila G. Bailey, Aloysius F. Hepp, Dale C. Ferguson, Ryne P. Raffaelle, and Steven M. Durbin, editors, *Photovoltaics for Space*, pages 51–78. Elsevier, January 2023.

[39] Geoffrey A. Landis. Chapter fourteen - Space photovoltaics for extreme high-temperature missions. In Sheila G. Bailey, Aloysius F. Hepp, Dale C. Ferguson, Ryne P. Raffaelle, and Steven M. Durbin, editors, *Photovoltaics for Space*, pages 393–410. Elsevier, January 2023.

[40] Jiang He, Tianhui Li, Xueping Liu, Hang Su, Zhiliang Ku, Jie Zhong, Fuzhi Huang, Yong Peng, and Yi-Bing Cheng. Influence of phase transition on stability of perovskite solar cells under thermal cycling conditions. *Solar Energy*, 188:312–317, August 2019.

[41] Ghada Abdelmageed, Cameron Mackeen, Kaitlin Hellier, Leila Jewell, Lydia Seymour, Mark Tingwald, Frank Bridges, Jin Z. Zhang, and Sue Carter. Effect of temperature on light induced degradation in methylammonium lead iodide perovskite thin films and solar cells. *Solar Energy Materials and Solar Cells*, 174:566–571, January 2018.

[42] Azat F. Akbulatov, Marina I. Ustinova, Gennady V. Shilov, Nadezhda N. Dremova, Ivan S. Zhidkov, Ernst Z. Kurmaev, Lyubov A. Frolova, Alexander F. Shestakov, Sergey M. Aldoshin, and Pavel A. Troshin. Temperature Dynamics of MAPbI3 and PbI2 Photolysis: Revealing the Interplay between Light and Heat, Two Enemies of Perovskite Photovoltaics. *The Journal of Physical Chemistry Letters*, 12(18):4362–4367, May 2021. Publisher: American Chemical Society.

[43] D. C. Ferguson, D. P. Engelhart, R. C. Hoffmann, V. J. Murray, and E. A. Plis. Chapter two - Space solar arrays and spacecraft charging. In Sheila G. Bailey, Aloysius F. Hepp, Dale C. Ferguson, Ryne P. Raffaelle, and Steven M. Durbin, editors, *Photovoltaics for Space*, pages 29–50. Elsevier, January 2023.

[44] Sheila Bailey and Ryne Raffaelle. Chapter IID-2 - Operation of Solar Cells in a Space Environment. In Augustin McEvoy, Tom Markvart, and Luis Castañer, editors, *Practical Handbook of Photovoltaics (Second Edition)*, pages 863–880. Academic Press, Boston, January 2012.

[45] Brandon K. Durant, Ian R. Sellers, and Bibhudutta Rout. Chapter Seven - Perovskite solar cells on the horizon for space power systems. In Sheila G. Bailey, Aloysius F. Hepp, Dale C. Ferguson, Ryne P. Raffaelle, and Steven M. Durbin, editors, *Photovoltaics for Space*, pages 175–195. Elsevier, January 2023.

[46] Ina T. Martin, Kyle Crowley, and Aloysius F. Hepp. Chapter Nine - Thin-film materials for space power applications. In Sheila G. Bailey, Aloysius F. Hepp, Dale C. Ferguson, Ryne P. Raffaelle, and Steven M. Durbin, editors, *Photovoltaics for Space*, pages 215–263. Elsevier, January 2023.

[47] Sheila G. Bailey and Dennis J. Flood. Space photovoltaics. *Progress in Photovoltaics: Research and Applications*, 6(1):1–14, 1998. _eprint: https://onlinelibrary.wiley.com/doi/pdf/10.1002/%28SICI%291099-159X%28199801/02%296%3A1%3C1%3A%3AAID-PIP204%3E3.0.CO%3B2-X.

[48] Anderson Bermudez-Garcia, Philippe Voarino, and Olivier Raccurt. Environments, needs and opportunities for future space photovoltaic power generation: A review. *Applied Energy*, 290:116757, May 2021.

[49] Ahmad R. Kirmani, Brandon K. Durant, Jonathan Grandidier, Nancy M. Haegel, Michael D. Kelzenberg, Yao M. Lao, Michael D. McGehee, Lyndsey McMillon-Brown, David P. Ostrowski, Timothy J. Peshek, Bibhudutta Rout, Ian R. Sellers, Mark Steger, Don Walker, David M. Wilt, Kaitlyn T. VanSant, and Joseph M. Luther. Countdown to perovskite space launch: Guidelines to performing relevant radiation-hardness experiments. *Joule*, 6(5):1015–1031, May 2022.

[50] Ahmad R. Kirmani, Todd A. Byers, Zhenyi Ni, Kaitlyn VanSant, Darshpreet K. Saini, Rebecca Scheidt, Xiaopeng Zheng, Tatchen Buh Kum, Ian R. Sellers, Lyndsey McMillon-Brown, Jinsong Huang, Bibhudutta Rout, and Joseph M. Luther. Unraveling radiation damage and healing mechanisms in halide perovskites using energy-tuned dual irradiation dosing. *Nature Communications*, 15(1):1–10, January 2024. Number: 1 Publisher: Nature Publishing Group.

[51] Yu Miyazawa, Masashi Ikegami, Tsutomu Miyasaka, Takeshi Ohshima, Mitsuru Imaizumi, and Kazuyuki Hirose. Evaluation of radiation tolerance of perovskite solar cell for use in space. In *2015 IEEE 42nd Photovoltaic Specialist Conference (PVSC)*, pages 1–4, June 2015.

[52] Yu Miyazawa, Masashi Ikegami, Hsin-Wei Chen, Takeshi Ohshima, Mitsuru Imaizumi, Kazuyuki Hirose, and Tsutomu Miyasaka. Tolerance of Perovskite Solar Cell to High-Energy Particle Irradiations in Space Environment. *iScience*, 2:148–155, April 2018.

[53] Brandon K. Durant, Hadi Afshari, Shashi Sourabh, Vishal Yeddu, Matthew T. Bamidele, Satyabrata Singh, Bibhudutta Rout, Giles E. Eperon, Do Young Kim, and Ian R. Sellers. Radiation stability of mixed tin–lead halide perovskites: Implications for space applications. *Solar Energy Materials and Solar Cells*, 230:111232, September 2021.

[54] Brandon K. Durant, Hadi Afshari, Satyabrata Singh, Bibhudutta Rout, Giles E. Eperon, and Ian R. Sellers. Tolerance of Perovskite Solar Cells to Targeted Proton Irradiation and Electronic Ionization Induced Healing. *ACS Energy Letters*, 6(7):2362–2368, July 2021. Publisher: American Chemical Society.

[55] Felix Lang, Marko Jošt, Jürgen Bundesmann, Andrea Denker, Steve Albrecht, Giovanni Landi, Heinz-Christoph Neitzert, Jörg Rappich, and Norbert H. Nickel. Efficient minority carrier detrapping mediating the radiation hardness of triple-cation perovskite solar cells under proton irradiation. *Energy & Environmental Science*, 12(5):1634–1647, May 2019. Publisher: The Royal Society of Chemistry.

[56] Felix Lang, Marko Jošt, Kyle Frohna, Eike Köhnen, Amran Al-Ashouri, Alan R. Bowman, Tobias Bertram, Anna Belen Morales-Vilches, Dibyashree Koushik, Elizabeth M. Tennyson, Krzysztof Galkowski, Giovanni Landi, Mariadriana Creatore, Bernd Stannowski, Christian A. Kaufmann, Jürgen Bundesmann, Jörg Rappich, Bernd Rech, Andrea Denker, Steve Albrecht, Heinz-Christoph Neitzert, Norbert H. Nickel, and Samuel D. Stranks. Proton Radiation Hardness of Perovskite Tandem Photovoltaics. *Joule*, 4(5):1054–1069, May 2020.

[57] Michael Saliba, Juan-Pablo Correa-Baena, Michael Grätzel, Anders Hagfeldt, and Antonio Abate. Perovskite solar cells: From the atomic level to film quality and device performance. *Angewandte Chemie International Edition*, 57(10):2554–2569, 2018.

[58] Jia-Wen Xiao, Lang Liu, Deliang Zhang, Nicholas De Marco, Jin-Wook Lee, Oliver Lin, Qi Chen, and Yang Yang. The Emergence of the Mixed Perovskites and Their Applications as Solar Cells. *Advanced Energy Materials*, 7(20):1700491, 2017. _eprint: https://onlinelibrary.wiley.com/doi/pdf/10.1002/aenm.201700491.

[59] Chenyi Yi, Jingshan Luo, Simone Meloni, Ariadni Boziki, Negar Ashari-Astani, Carole Grätzel, Shaik M. Zakeeruddin, Ursula Röthlisberger, and Michael

Grätzel. Entropic stabilization of mixed A-cation ABX3 metal halide perovskites for high performance perovskite solar cells. *Energy & Environmental Science*, 9(2):656–662, February 2016. Publisher: The Royal Society of Chemistry.

[60] Tyler Colenbrander, Jun Peng, Yiliang Wu, Michael Kelzenberg, Jing-Shun Huang, Clara MacFarland, Dennis Thorbourn, Robert Kowalczyk, Wousik Kim, John Brophy, Anh Dinh Bui, Dang-Thuan Nguyen, Hieu T. Nguyen, Harry A. Atwater, Thomas P. White, and Jonathan Grandidier. Low-intensity low-temperature analysis of perovskite solar cells for deep space applications††electronic supplementary information (esi) available. see doi: https://doi.org/10.1039/d2ya00218c. *Energy Advances*, 2(2):298–307, 2023.

[61] Ilaria Cardinaletti, Tim Vangerven, Steven Nagels, Rob Cornelissen, Dieter Schreurs, Jaroslav Hruby, Jelle Vodnik, Dries Devisscher, Jurgen Kesters, Jan D'Haen, Alexis Franquet, Valentina Spampinato, Thierry Conard, Wouter Maes, Wim Deferme, and Jean V. Manca. Organic and perovskite solar cells for space applications. *Solar Energy Materials and Solar Cells*, 182:121–127, August 2018.

[62] Hua Zhang, Xianfeng Qiao, Yan Shen, Thomas Moehl, Shaik M. Zakeeruddin, Michael Grätzel, and Mingkui Wang. Photovoltaic behaviour of lead methylammonium triiodide perovskite solar cells down to 80 K. *Journal of Materials Chemistry A*, 3(22):11762–11767, May 2015. Publisher: The Royal Society of Chemistry.

[63] Guixiang Li, Zhenhuang Su, Laura Canil, Declan Hughes, Mahmoud H. Aldamasy, Janardan Dagar, Sergei Trofimov, Luyao Wang, Weiwei Zuo, José J. Jerónimo-Rendon, Mahdi Malekshahi Byranvand, Chenyue Wang, Rui Zhu, Zuhong Zhang, Feng Yang, Giuseppe Nasti, Boris Naydenov, Wing C. Tsoi, Zhe Li, Xingyu Gao, Zhaokui Wang, Yu Jia, Eva Unger, Michael Saliba, Meng Li, and Antonio Abate. Highly efficient p-i-n perovskite solar cells that endure temperature variations. *Science*, 379(6630):399–403, January 2023. Publisher: American Association for the Advancement of Science.

[64] Gang Liu, Conghua Zhou, Fang Wan, Kangming Li, Yongbo Yuan, Yongli Gao, Yunzhang Lu, and Bingchu Yang. Dependence of power conversion properties of perovskite solar cells on operating temperature. *Applied Physics Letters*, 113(11):113501, September 2018.

[65] Lyndsey McMillon-Brown, Joseph M. Luther, and Timothy J. Peshek. What Would It Take to Manufacture Perovskite Solar Cells in Space? *ACS Energy Letters*, 7(3):1040–1042, March 2022. Publisher: American Chemical Society.

[66] Zhen Li, Talysa R. Klein, Dong Hoe Kim, Mengjin Yang, Joseph J. Berry, Maikel F. A. M. van Hest, and Kai Zhu. Scalable fabrication of perovskite solar cells. *Nature Reviews Materials*, 3(4):1–20, March 2018. Publisher: Nature Publishing Group.

[67] Dong Yang, Ruixia Yang, Shashank Priya, and Shengzhong (Frank) Liu. Recent Advances in Flexible Perovskite Solar Cells: Fabrication and Applications. *Angewandte Chemie International Edition*, 58(14):4466–4483, 2019. _eprint: https://onlinelibrary.wiley.com/doi/pdf/10.1002/anie.201809781.

[68] Priyanka Roy, Numeshwar Kumar Sinha, Sanjay Tiwari, and Ayush Khare. A review on perovskite solar cells: Evolution of architecture, fabrication techniques, commercialization issues and status. *Solar Energy*, 198:665–688, March 2020.

[69] Hasitha C. Weerasinghe, Nasiruddin Macadam, Jueng-Eun Kim, Luke J. Sutherland, Dechan Angmo, Leonard W. T. Ng, Andrew D. Scully, Fiona Glenn, Regine Chantler, Nathan L. Chang, Mohammad Dehghanimadvar, Lei Shi, Anita W. Y. Ho-Baillie, Renate Egan, Anthony S. R. Chesman, Mei Gao, Jacek J. Jasieniak, Tawfique Hasan, and Doojin Vak. The first demonstration of entirely roll-to-roll fabricated perovskite solar cell modules under ambient room conditions. *Nature Communications*, 15(1):1656, March 2024. Publisher: Nature Publishing Group.

[70] Seung Yeon Lee, Geon Yeong Park, Na-Yeon Kim, Minji Kang, Kiho Kim, Seong-Keun Cho, Woojin Choi, Jin Suk Myung, and Dong Seok Ham. Tailoring the SnO2 Ink for Roll-to-Roll Manufacturing of Flexible Perovskite Solar Cells. *Energy Technology*, 12(3):2301058, 2024. _eprint: https://onlinelibrary.wiley.com/doi/pdf/10.1002/ente.202301058.

[71] Lennart K. Reb, Michael Böhmer, Benjamin Predeschly, Sebastian Grott, Christian L. Weindl, Goran I. Ivandekic, Renjun Guo, Christoph Dreißigacker, Roman Gernhäuser, Andreas Meyer, and Peter Müller-Buschbaum. Perovskite and Organic Solar Cells on a Rocket Flight. *Joule*, 4(9):1880–1892, September 2020.

[72] DC93-500 Silicone Elastomer. https://www.ellsworth.com/products/by-market/defense/sealants/silicone/dow-93-500-space-grade-encapsulant-clear-115-g-kit/.

[73] G A Haynes. Effect of radiation on cerium-doped solar-cell cover glass. NASA Technical Note TN D-6024, Langley Research Center, Hampton, VA, 1970.

[74] Dominic B. Doyle and Reinhard H. Czichy. Influences of simulated space radiation on optical glasses. In *Space Optics 1994: Space Instrumentation and Spacecraft Optics*, volume 2210, pages 434–448. SPIE, September 1994.

[75] Tammy D. Henson and Geoffrey K. Torrington. Space radiation testing of radiation-resistant glasses and crystals. In *Inorganic Optical Materials III*, volume 4452, pages 54–65. SPIE, November 2001.

[76] Wolfgang Tress, Konrad Domanski, Brian Carlsen, Anand Agarwalla, Essa A. Alharbi, Michael Graetzel, and Anders Hagfeldt. Performance of perovskite solar cells under simulated temperature-illumination real-world operating conditions. *Nature Energy*, 4(7):568–574, July 2019. Publisher: Nature Publishing Group.

[77] Benjamin R. Ecker, Congcong Wang, Haotong Wei, Yongbo Yuan, Jinsong Huang, and Yongli Gao. Intrinsic Behavior of CH3NH3PbBr3 Single Crystals under Light Illumination. *Advanced Materials Interfaces*, 5(23):1801206, 2018. _eprint: https://onlinelibrary.wiley.com/doi/pdf/10.1002/admi.201801206.

[78] Hoyeon Choi, Jack Chun-Ren Ke, Stefan Skalsky, Christopher A. Castle, Kexue Li, Katie L. Moore, Wendy R. Flavell, and Patrick Parkinson. Visualizing the role of photoinduced ion migration on photoluminescence in halide perovskite grains. *Journal of Materials Chemistry C*, 8(22):7509–7518, June 2020. Publisher: The Royal Society of Chemistry.

[79] Caleb C. Boyd, Rongrong Cheacharoen, Tomas Leijtens, and Michael D. McGehee. Understanding Degradation Mechanisms and Improving Stability of Perovskite Photovoltaics. *Chemical Reviews*, 119(5):3418–3451, March 2019. Publisher: American Chemical Society.

[80] Cheng Zhu, Xiuxiu Niu, Yuhao Fu, Nengxu Li, Chen Hu, Yihua Chen, Xin He, Guangren Na, Pengfei Liu, Huachao Zai, Yang Ge, Yue Lu, Xiaoxing Ke, Yang Bai, Shihe Yang, Pengwan Chen, Yujing Li, Manling Sui, Lijun Zhang, Huanping Zhou, and Qi Chen. Strain engineering in perovskite solar cells and its impacts on carrier dynamics. *Nature Communications*, 10(1):815, February 2019. Publisher: Nature Publishing Group.

[81] Emmanuel V. Péan, Catherine S. De Castro, and Matthew L. Davies. Shining a light on the photoluminescence behaviour of methylammonium lead iodide perovskite: investigating the competing photobrightening and photodarkening processes. *Materials Letters*, 243:191–194, May 2019.

[82] Xiao Fu, Daniel A. Jacobs, Fiona J. Beck, The Duong, Heping Shen, Kylie R. Catchpole, and Thomas P. White. Photoluminescence study of time- and

spatial-dependent light induced trap de-activation in CH3NH3PbI3 perovskite films. *Physical Chemistry Chemical Physics*, 18(32):22557–22564, August 2016. Publisher: The Royal Society of Chemistry.

[83] Hsinhan Tsai, Reza Asadpour, Jean-Christophe Blancon, Constantinos C. Stoumpos, Olivier Durand, Joseph W. Strzalka, Bo Chen, Rafael Verduzco, Pulickel M. Ajayan, Sergei Tretiak, Jacky Even, Muhammad Ashraf Alam, Mercouri G. Kanatzidis, Wanyi Nie, and Aditya D. Mohite. Light-induced lattice expansion leads to high-efficiency perovskite solar cells. *Science*, 360(6384):67–70, April 2018. Publisher: American Association for the Advancement of Science.

[84] S. A. Shojaee, T. A. Harriman, G. S. Han, J.-K. Lee, and D. A. Lucca. Substrate effects on photoluminescence and low temperature phase transition of methylammonium lead iodide hybrid perovskite thin films. *Applied Physics Letters*, 111(2):023902, July 2017.

[85] Sunihl Ma, Seong Hun Kim, Beomjin Jeong, Hyeok-Chan Kwon, Seong-Cheol Yun, Gyumin Jang, Hyunha Yang, Cheolmin Park, Donghwa Lee, and Jooho Moon. Strain-Mediated Phase Stabilization: A New Strategy for Ultrastable α-CsPbI3 Perovskite by Nanoconfined Growth. *Small*, 15(21):1900219, 2019. _eprint: https://onlinelibrary.wiley.com/doi/pdf/10.1002/smll.201900219.

[86] William G. Delmas, Evan T. Vickers, Albert C. DiBenedetto, Calista Lum, Isaak N. Hernandez, Jin Z. Zhang, and Sayantani Ghosh. Modulating Charge Carrier Dynamics and Transfer via Surface Modifications in Organometallic Halide Perovskite Quantum Dots. *The Journal of Physical Chemistry Letters*, 11(18):7886–7892, September 2020. Publisher: American Chemical Society.

[87] P. S. Whitfield, N. Herron, W. E. Guise, K. Page, Y. Q. Cheng, I. Milas, and M. K. Crawford. Structures, Phase Transitions and Tricritical Behavior of the Hybrid Perovskite Methyl Ammonium Lead Iodide. *Scientific Reports*, 6(1):35685, October 2016.

[88] SRIM & TRIM Simulation Software. http://www.srim.org/.

[89] E. R Benton and E. V Benton. Space radiation dosimetry in low-Earth orbit and beyond. *Nuclear Instruments and Methods in Physics Research Section B: Beam Interactions with Materials and Atoms*, 184(1):255–294, September 2001.

[90] Olga Malinkiewicz, Mitsuru Imaizumi, Subarna B. Sapkota, Takeshi Ohshima, and Senol Öz. Radiation effects on the performance of flexible perovskite solar cells for space applications. *Emergent Materials*, 3(1):9–14, February 2020.

[91] Shusaku Kanaya, Gyu Min Kim, Masashi Ikegami, Tsutomu Miyasaka, Kohtaku Suzuki, Yu Miyazawa, Hiroyuki Toyota, Kanta Osonoe, Tomoyuki Yamamoto, and Kazuyuki Hirose. Proton Irradiation Tolerance of High-Efficiency Perovskite Absorbers for Space Applications. *The Journal of Physical Chemistry Letters*, 10(22):6990–6995, November 2019. Publisher: American Chemical Society.

[92] Jing-Shun Huang, Michael D. Kelzenberg, Pilar Espinet-González, Colin Mann, Don Walker, Ali Naqavi, Nina Vaidya, Emily Warmann, and Harry A. Atwater. Effects of Electron and Proton Radiation on Perovskite Solar Cells for Space Solar Power Application. In *2017 IEEE 44th Photovoltaic Specialist Conference (PVSC)*, pages 1248–1252, June 2017.

[93] Walter O. Herrera Martínez, Natalia B. Correa Guerrero, Victoria A. Gómez Andrade, Martin Alurralde, and M. Dolores Perez. Evaluation of the resistance of halide perovskite solar cells to high energy proton irradiation for space applications. *Solar Energy Materials and Solar Cells*, 238:111644, May 2022.

[94] Felix Lang, Norbert H. Nickel, Jürgen Bundesmann, Sophie Seidel, Andrea Denker, Steve Albrecht, Victor V. Brus, Jörg Rappich, Bernd Rech, Giovanni Landi, and Heinrich C. Neitzert. Radiation Hardness and Self-Healing of Perovskite Solar Cells. *Advanced Materials*, 28(39):8726–8731, 2016. _eprint: https://onlinelibrary.wiley.com/doi/pdf/10.1002/adma.201603326.

[95] Daniel Pérez-del Rey, Chris Dreessen, Ana M. Igual-Muñoz, Lennart van den Hengel, María C. Gélvez-Rueda, Tom J. Savenije, Ferdinand C. Grozema, Claus Zimmermann, and Henk J. Bolink. Perovskite Solar Cells: Stable under Space Conditions. *Solar RRL*, 4(12):2000447, 2020. _eprint: https://onlinelibrary.wiley.com/doi/pdf/10.1002/solr.202000447.

[96] Standard: Qualification and Quality Requirements for Space Solar Cells (AIAA S-111A-2014). In *Standard: Qualification and Quality Requirements for Space Solar Cells (AIAA S-111A-2014)*, AIAA Standards. American Institute of Aeronautics and Astronautics, Inc., January 2014.

[97] Bibhudutta Rout, Mangal S. Dhoubhadel, Prakash R. Poudel, Venkata C. Kummari, Bimal Pandey, Naresh T. Deoli, Wickramaarachchige J. Lakshantha, Stephen J. Mulware, Jacob Baxley, Jack E. Manuel, Jose L. Pacheco, Szabolcs Szilasi, Duncan L. Weathers, Tilo Reinert, Gary A. Glass, Jerry L. Duggan, and Floyd D. McDaniel. An overview of the facilities, activities, and developments at the University of North Texas Ion Beam Modification and Analysis Laboratory (IBMAL). *AIP Conference Proceedings*, 1544(1):11–18, July 2013.

[98] SPENVIS - Space Environment, Effects, and Education System. https://www.spenvis.oma.be/.

[99] Esma Ugur, Erkki Alarousu, Jafar I. Khan, Aleš Vlk, Erkan Aydin, Michele De Bastiani, Ahmed H. Balawi, Sandra P. Gonzalez Lopez, Martin Ledinský, Stefaan De Wolf, and Frédéric Laquai. How Humidity and Light Exposure Change the Photophysics of Metal Halide Perovskite Solar Cells. *Solar RRL*, 4(11):2000382, 2020. _eprint: https://onlinelibrary.wiley.com/doi/pdf/10.1002/solr.202000382.

[100] Cai-Xin Zhang, Tao Shen, Dan Guo, Li-Ming Tang, Kaike Yang, and Hui-Xiong Deng. Reviewing and understanding the stability mechanism of halide perovskite solar cells. *InfoMat*, 2(6):1034–1056, 2020. _eprint: https://onlinelibrary.wiley.com/doi/pdf/10.1002/inf2.12104.

[101] Blake P. Finkenauer, Akriti, Ke Ma, and Letian Dou. Degradation and Self-Healing in Perovskite Solar Cells. *ACS Applied Materials & Interfaces*, 14(21):24073–24088, June 2022. Publisher: American Chemical Society.

[102] Chenyun Wang, Du Qu, Bin Zhou, Chuanzhen Shang, Xinyue Zhang, Yongguang Tu, and Wei Huang. Self-Healing Behavior of the Metal Halide Perovskites and Photovoltaics. *Small*, 20(6):2307645, 2024. _eprint: https://onlinelibrary.wiley.com/doi/pdf/10.1002/smll.202307645.

[103] Timothy S. Krause, Kaitlyn T. VanSant, Andrew Lininger, Kyle Crowley, Timothy J. Peshek, and Lyndsey McMillon-Brown. Thermal Performance of Perovskite-Based Photovoltaics for Operation in Low Earth Orbit. *Solar RRL*, 7(21):2300468, 2023. _eprint: https://onlinelibrary.wiley.com/doi/pdf/10.1002/solr.202300468.

[104] Carla Costa, Matthieu Manceau, Sophie Duzellier, Thierry Nuns, and Romain Cariou. Perovskite solar cells under protons irradiation: From in-situ IV-monitoring to root cause degradation elucidation. *Solar Energy Materials and Solar Cells*, 257:112388, August 2023.

[105] Gregory P. Ginet, Bronislaw K. Dichter, Donald H. Brautigam, and Dan Madden. Proton Flux Anisotropy in Low Earth Orbit. *IEEE Transactions on Nuclear Science*, 54(6):1975–1980, December 2007. Conference Name: IEEE Transactions on Nuclear Science.

[106] Gautam D. Badhwar. The Radiation Environment in Low-Earth Orbit. *Radiation Research*, 148(5s):S3–S10, November 1997.

[107] Vikash Kumar Ravi, Ganesh B. Markad, and Angshuman Nag. Band Edge Energies and Excitonic Transition Probabilities of Colloidal CsPbX3 (X = Cl, Br, I) Perovskite Nanocrystals. *ACS Energy Letters*, 1(4):665–671, 2016. _eprint: https://doi.org/10.1021/acsenergylett.6b00337.

[108] Riley E. Brandt, Vladan Stevanović, David S. Ginley, and Tonio Buonassisi. Identifying defect-tolerant semiconductors with high minority-carrier lifetimes: beyond hybrid lead halide perovskites. *MRS Communications*, 5(2):265–275, 2015.

[109] Manuel Weiss, Jonas Horn, Christoph Richter, and Derck Schlettwein. Preparation and characterization of methylammonium tin iodide layers as photovoltaic absorbers. *physica status solidi (a)*, 213(4):975–981, 2016.

[110] Andriy Zakutayev, Christopher M. Caskey, Angela N. Fioretti, David S. Ginley, Julien Vidal, Vladan Stevanovic, Eric Tea, and Stephan Lany. Defect tolerant semiconductors for solar energy conversion. *The Journal of Physical Chemistry Letters*, 5(7):1117–1125, 2014. PMID: 26274458.